Modeling of Nearshore Hydrodynamics for Sediment Transport Calculations

by

David Gonzalez-Rodriguez

B.S., Civil Engineering (2002)
University of La Coruña

Submitted to the Department of Civil and Environmental Engineering
in partial fulfillment of the requirements for the degree of

Master of Science in Civil and Environmental Engineering

at the

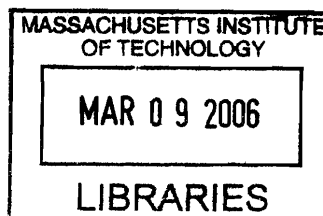MASSACHUSETTS INSTITUTE OF TECHNOLOGY

February 2006

© Massachusetts Institute of Technology 2006. All rights reserved.

Author . . . .
Department of Civil and Environmental Engineering
October 20th, 2005

Certified by . . . .
Ole S. Madsen
Professor, Department of Civil and Environmental Engineering
Thesis Supervisor

Accepted by . . . .
Andrew J. Whittle
Chairman, Department Committee on Graduate Students

Modeling of Nearshore Hydrodynamics for Sediment Transport Calculations

by

David Gonzalez-Rodriguez

Submitted to the Department of Civil and Environmental Engineering
on October 21st, 2005, in partial fulfillment of the
requirements for the degree of
Master of Science in Civil and Environmental Engineering

Abstract

This thesis analyzes and improves Tajima's (2004) nearshore hydrodynamic model. Tajima's simple model accurately predicts long-shore sediment transport along long, straight beaches, while cross-shore transport predictions differ from observations. A better prediction of cross-shore transport requires improvement of the hydrodynamic model.

We first contrast Tajima's model with other hydrodynamic models. To improve the characterization of incident waves, we examine a number of joint probability distributions of wave heights and periods. These distributions are then used to develop a probabilistic wave-by-wave hydrodynamic description based on Tajima's monochromatic wave model. We derive the model governing equations for the unsteady case and detail their numerical implementation. This unsteady model is applied to study the effect of a wave beat normally incident on a plane sloping beach. We use this case to illustrate the relevance of the unsteady generalization to sediment transport calculations.

Thesis Supervisor: Ole S. Madsen
Title: Professor, Department of Civil and Environmental Engineering

Acknowledgments

I would first like to express my deepest gratitude to my advisor, Professor Ole S. Madsen, for his patience, guidance, and for the numerous enlightening discussions that took place throughout this work. Prof. Madsen's kindness and hospitality have made me feel in Boston like at home.

I gratefully acknowledge the financial support over two years of my Master's study by *Fundación Pedro Barrié de la Maza* in La Coruña, Spain. Their generous scholarship program has made it possible for me to study at MIT. I am also thankful to Mrs. Sandra L. Cervera, from the *Institute of International Education*, for administering my scholarship with great efficiency and fondness.

One of my best experiences as a graduate student has been to attend Professor Chiang C. Mei's insightful lectures in Mathematical Modeling, Fluid Dynamics, and Wave Propagation. I have truly enjoyed them.

This thesis arises from previous work by Dr. Yoshimitsu Tajima, who kindly provided me with numerical codes and experimental data sets. I would like to thank Yukie Tanino for proofreading a draft of the thesis. I also thank my friends at MIT for the enjoyable times we have spent together.

I dedicate this thesis to my parents, María José and Ventura.

Contents

7

List of Figures

12

List of Tables

Chapter 1

Introduction

1.1 Motivation

Evolution of beach morphology and, more specifically, erosion processes are major concerns in coastal engineering. These changes in beach morphology are caused by the local imbalance of sediment transport. Tajima (2004) developed a hydrodynamic model whose ultimate purpose was to forecast sediment transport in the surf zone. This hydrodynamic model is based on linear wave theory and therefore involves smaller computational effort than other recent models based on the Boussinesq equations (e.g., Madsen et al., 1997a,b; Kirby et al., 1998; Chen et al., 2000). Moreover, Tajima's model is able to compute non-linear wave characteristics by establishing an equivalence between linear and non-linear waves. This makes Tajima's approach useful to predict sediment transport in a computationally inexpensive way.

Applying his hydrodynamic model, Tajima (2004) succeeded in forecasting longshore sediment transport on a long, straight beach, but his prediction of cross-shore transport differed significantly from experimental observations. Net cross-shore sediment transport is the *small* difference between two *large* quantities, on- and off-shore transports. Therefore, to obtain a reasonable prediction of the net cross-shore transport, both on- and off-shore transport rates need to be very accurately calculated. To this end, all relevant processes affecting sediment transport must be accounted for.

Several aspects of Tajima's hydrodynamic model can be improved. The model

describes the propagation of monochromatic or narrow-banded spectral waves into the surf zone. However, real waves in the nearshore region follow more complicated distributions than the simple one assumed by Tajima (2004). Moreover, Tajima defines the incident waves in terms of their long-term average characteristics, thus neglecting all unsteady effects originated by the slow modulation in wave parameters from one wave to the next.

The first purpose of this thesis is to compare Tajima's hydrodynamic model with other previously existing simple linear models, to show the suitability of Tajima's hydrodynamic model for performing sediment transport calculations. Second, we are interested in confronting it with more detailed descriptions of random waves, to decide whether Tajima's simple model provides an accurate enough description of real waves. Third, we will generalize Tajima's hydrodynamic model formulation to account for unsteadiness, which will provide the necessary basis to refine sediment transport calculations.

1.2   Thesis outline

In Chapter 2 we present Tajima's hydrodynamic model, whose analysis and improvement are the goals of this thesis. This hydrodynamic model consists of a wave model, a surface roller model, and a nearshore current model. First, we summarize the formulation of Tajima's wave model, and compare it with the linear wave models by Battjes and Janssen (1978) and Thornton and Guza (1983). We test the three wave models in plane and barred beach cases and compare their accuracy with experimental measurements. Then, we introduce Tajima's surface roller model and compare it with the model by Stive and De Vriend (1994). Finally, we present Tajima's nearshore current model.

In Chapter 3 we examine a number of statistical models that describe incident waves through the use of joint probability distributions of wave heights and periods. We introduce a probabilistic wave-by-wave approach, based on Tajima's monochromatic model, to propagate incident waves characterized by a probability distribution.

Using Longuet-Higgins's 1975 and 1983 distributions, which are shown to be consistent with the JONSWAP spectrum, this detailed wave-by-wave approach is applied to test cases and compared with Tajima's simpler random wave model.

In Chapter 4 we derive the governing equations for the unsteady case. We also present the details for its numerical implementation. Then, we apply the unsteady model to test cases. We compare the time-averaged results of the unsteady model with those of Tajima's monochromatic steady model. We study the effect of a wave beat acting on a plane sloping beach, and use this case to illustrate the relevance of the unsteady generalization to sediment transport calculations.

In Chapter 5 we summarize our conclusions and present directions for future work.

Chapter 2

Steady one-dimensional hydrodynamic model

In this chapter, we summarize the main characteristics of the hydrodynamic model presented by Tajima (2004), whose analysis and further development is the purpose of this thesis. We compare Tajima's model with previous models that were developed to compute similar hydrodynamic characteristics. First, we introduce Tajima's wave model, and compare it with the models by Battjes and Janssen (1978) and by Thornton and Guza (1983). Then, we present Tajima's surface roller model, and compare it with the model by Stive and De Vriend (1994). Finally, we summarize Tajima's nearshore current model.

2.1   Wave model

Here, we present Tajima's (2004) wave propagation model, as well as the models developed by Battjes and Janssen (1978) and by Thornton and Guza (1983). We want to confirm the convenience of keeping Tajima's wave model in our formulation, instead of replacing it by one of these alternatives. We first summarize the theoretical basis of each of these three models. Then, we compare the accuracy of their respective predictions in a number of test cases.

2.1.1 Tajima's wave model

A hydrodynamic model developed to compute nearshore sediment transport needs to take into account non-linear wave characteristics. Non-linear effects, such as skewness and asymmetry of the near-bottom wave orbital velocity, may have significant effects on sediment transport. Most of the recently developed wave propagation models use the Boussinesq equations, first derived by Peregrine (1967) and later improved by Nwogu (1993), to compute non-linear wave characteristics. However, since Boussinesq equations are based on the assumption of weak non-linearity, Nwogu's modified Boussinesq equations fail in yielding accurate predictions in the vicinity of the breakpoint, where non-linear effects are strong. As pointed out by Wei et al. (1995) and Madsen et al. (1996), use of fully non-linear Boussinesq equations is necessary to make reliable predictions in this region. This approach, although accurate, turns out to be expensive from a computational standpoint.

Tajima's (2004) approach starts from establishing a correspondence between linear and non-linear wave characteristics. This makes it possible to use linear wave theory to propagate the waves and then obtain non-linear wave characteristics from the linear results. This model, based on linear theory, is computationally very efficient, and therefore suitable when extensive iterative calculations are necessary, as is the case for predicting sediment transport and coastal morphodynamics.

Non-linear wave model

Tajima (2004) defines the equivalent linear wave as the wave that has the same energy flux as the actual non-linear wave. It is interesting to note that, since non-linear effects nearly vanish in deep water, the non-linear wave and the equivalent linear wave have the same deep-water characteristics, such as wavelength L_0 and wave height H_0.

To determine the relationship between non-linear and equivalent linear waves, Tajima conducts a series of numerical experiments. These consist of propagating a given wave, of deep water wave height H_0, on a plane beach, first using linear theory and then using Nwogu's (1993) modified Boussinesq equations. In this latter case,

incident wave profiles are obtained from 5th order Stokes wave theory (Isobe, 1979) or stream function theory with 19 terms (Dean, 1965). At each depth, both linear and non-linear waves are *equivalent* in the aforementioned sense, since they have the same energy flux. By carrying out these numerical experiments for different plane slopes, Tajima obtains relationships between non-linear wave characteristics and equivalent linear ones, as a function of non-dimensional depth (h/L_0), non-dimensional deep water wave height (H_0/L_0) and bottom slope. The non-linear wave characteristics of interest are: Wave height, near-bottom wave orbital velocity, and its asymmetry and skewness. All these relationships are detailed in Tajima (2004, §2.1.3).

Once these relationships are established, the model uses linear wave theory to propagate waves until the breakpoint. After breaking, a broken wave dissipation term is introduced in the energy flux balance equation. The procedure for determining the breakpoint and the formulation for broken waves are summarized in the following paragraphs.

Breaking wave model

Since linear theory is used to propagate the waves, the breaking wave criterion is developed in terms of equivalent linear wave heights. Following Watanabe et al. (1984), Tajima formulates the breaking criterion in terms of u_c/C, the ratio between the water particle velocity at the wave crest and the phase velocity. The breaking wave height is determined as a function of the non-dimensional depth, h_b/L_0, and the slope, β_0, in the following way:

$$\left(\frac{2u_c}{C}\right)_b = \frac{k_b H_b}{\tanh(k_b h_b)} = f(h_b/L_0, \tan\beta_0) \tag{2.1}$$

where $k_b = 2\pi/L_b$ is the wave number and the subscript b makes reference to breaking conditions.

The function f is required to satisfy Michell's (1893) breaking criterion in deep water,

$$\frac{H_{b*}}{L_{b*}} = 0.142 \tag{2.2}$$

where the $*$ refers to non-linear wave characteristics. In terms of linear wave characteristics, Michell's criterion reads

$$\frac{H_b}{L_b} = 0.17 \tag{2.3}$$

The function f is determined by fitting different sets of experimental data, which are detailed in Tajima (2004). As a result of the fitting, the breaking criterion, in terms of linear wave characteristics, is defined as

$$
\begin{aligned}
\frac{k_b H_b}{\tanh k_b h_b} &= 1.07 - 0.59 \exp\left(-8.6\frac{h_b}{L_0}\right) \\
&\quad + 2.59 \tan\beta_0 \exp\left(-15.1\left(\frac{h_b}{L_0}\right)^{1.5}\right)
\end{aligned}
\tag{2.4}
$$

Broken waves

Tajima's formulation for broken wave energy dissipation follows Dally et al's (1985),

$$\frac{\partial\left(EC_g\right)}{\partial x} = -K_b\frac{C_g}{h}\left(E - E_r\right) \tag{2.5}$$

where $E = \rho g H^2/8$ is the linear wave energy, C_g is the linear wave group velocity, $E_r = \rho g H_r^2/8$ is the wave energy based on the recovery wave height, $H_r = \gamma_r h$ (which is the eventual wave height if the wave were to continue propagating in the depth h), and K_b is a dissipation factor. Unlike Dally et al., who take K_b as constant, Tajima makes it depend on the slope. It is an empirical fact that broken waves on a plane beach, well inside the surf zone, have a wave height proportional to the depth, $H = \gamma_s h$. From this observation, and applying linear theory, Tajima concludes that

$$K_b = \frac{5}{2}\frac{\gamma_s^2 \tan\beta}{\gamma_s^2 - \gamma_r^2} \tag{2.6}$$

where $\tan\beta = \partial h/\partial x = \partial\left(h_0 + \bar{\eta}\right)/\partial x$ is the slope of the mean water depth. From experimental data fitting, the values of γ_r and γ_s are determined as

$$
\begin{aligned}
\gamma_r &= 0.3 \\
\gamma_s &= 0.3 + 4\tan\beta
\end{aligned}
\tag{2.7}
$$

Random waves

While the previous theory was developed assuming monochromatic waves, Tajima presents a simple formulation to extend his model to a random incident wave case. He assumes a narrow-banded spectrum, characterized by its peak frequency, and a Rayleigh distributed wave height. After breaking starts, wave heights remain Rayleigh distributed. The breaking criterion, (2.4), separates the broken waves from the unbroken ones. Only broken waves yield energy dissipation, following Tajima's energy dissipation law, (2.5). Under these assumptions, and after averaging (2.5) for the different wave heights, Tajima's energy balance equation for random waves reads

$$\frac{\partial (EC_g)}{\partial x} = -K_b \frac{C_g}{h} \exp\left(-\xi_b^2\right) \left[E\left(1 + \xi_b^2\right) - E_r\right] \tag{2.8}$$

where $E = \rho g H_{rms}^2/8$, $E_r = \rho g \left(\gamma_r h\right)^2/8$, with γ_r determined from (2.7), and $\xi_b = H_b/H_{rms}$, with H_b determined from the breaking criterion, (2.4).

2.1.2 Battjes and Janssen's wave model

The two other wave models we introduce in this chapter are linear and do not calculate non-linear wave characteristics. However, we are interested in comparing their predictions with Tajima's linear results. Like Tajima's (2004) random wave model, Battjes and Janssen's (1978) wave model also assumes a narrow-banded spectrum, and applies conservation of energy flux according to linear theory, allowing for an energy loss associated with wave breaking. The evolution of wave height is therefore determined by the following equation:

$$\frac{\partial(EC_g \cos\theta)}{\partial x} = -D \tag{2.9}$$

where $E = \rho g H_{rms}^2/8$ is the linear wave energy, C_g is the group velocity, θ is the angle between the wave fronts and the bathymetry, and D is the energy dissipation rate, which will be defined below.

Like Tajima, Battjes and Janssen assume a Rayleigh distributed wave height be-

fore breaking. After wave breaking starts, they assume a truncated Rayleigh distribution, where no waves larger than the breaking wave height are allowed. The model determines the local breaking wave height, H_m, by using a breaking criterion based on Miche (1951). In shallow water, Miche's criterion establishes that the breaking wave height, H_m, is proportional to the water depth, h, according to the expression

$$H_m = \gamma h \qquad (2.10)$$

where Miche suggests the value $\gamma = 0.88$ for the proportionality constant. In Battjes and Janssen's model, γ is left as an adjustable parameter, to account for the effects of beach slope. The breaking criterion they adopt is

$$H_m = 0.88k^{-1} \tanh\left(\frac{\gamma kh}{0.88}\right) \qquad (2.11)$$

They recommend using the value $\gamma = 0.8$ (Battjes and Janssen, 1978).

Once the breaking wave height is determined, Battjes and Janssen truncate the Rayleigh distribution for unbroken waves, by assuming all broken waves to have the local breaking wave height, H_m. The unbroken waves remain Rayleigh distributed. The corresponding cumulative distribution function for all waves is

$$F(H) = \begin{cases} 1 - \exp\left(-\frac{H^2}{2\hat{H}^2}\right) & \text{if } 0 \leq H < H_m \\ 1 & \text{if } H \geq H_m \end{cases} \qquad (2.12)$$

where $\hat{H}$ is the modal wave height. The root mean square wave height is computed as

$$H_{rms} = \sqrt{\int_0^\infty H^2 \frac{dF(H)}{dH} dH} \qquad (2.13)$$

The fraction of waves that are broken at a given location is

$$Q_b = \text{Prob}(H = H_m) = \exp\left(-\frac{H_m^2}{2\hat{H}^2}\right) \qquad (2.14)$$

26

Using (2.12), Q_b can be calculated from (2.13) as

$$H_{rms}^2 = \int_0^{H_m} \frac{H^3}{\hat{H}^2} \exp\left(-\frac{H^2}{2\hat{H}^2}\right) dH + H_m^2 Q_b \qquad (2.15)$$

which leads to

$$\frac{1 - Q_b}{\ln Q_b} = -\left(\frac{H_{rms}}{H_m}\right)^2 \qquad (2.16)$$

The energy dissipation rate due to wave breaking is calculated by simulating it to be that of a bore of corresponding height. The bore energy dissipation per unit area is

$$\epsilon_b = \frac{\bar{f}}{4}\rho g \frac{H^3}{h} \qquad (2.17)$$

where $\bar{f}$ is the mean frequency. This expression is simplified by assuming that $H/h = O(1)$. From this analogy, the energy dissipation rate is

$$D = \frac{\alpha}{4} Q_b \bar{f} \rho g H_m^2 \qquad (2.18)$$

where H_m is the breaking wave height and α is a constant, which is introduced as a factor of proportionality between the bore dissipation rate and the actual wave breaking dissipation rate. The value of α should be of the order of 1, according to the authors. The factor Q_b is introduced since only the broken waves contribute to energy dissipation.

2.1.3   Thornton and Guza's wave model

Thornton and Guza's (1983) wave model is based on similar assumptions to the ones in the two previously discussed models: (i) narrow-banded spectrum; (ii) conservation of energy flux according to linear theory; (iii) Rayleigh distributed wave height before breaking. The basic energy balance equation is similar to those of the previous models, and reads

$$\frac{\partial(E C_g \cos\theta)}{\partial x} = -\langle \epsilon_b \rangle - \langle \epsilon_f \rangle \qquad (2.19)$$

where $\langle \epsilon_b \rangle$ and $\langle \epsilon_f \rangle$ are energy dissipation rates related to wave breaking and bottom

friction, respectively. As pointed out by the authors, the frictional dissipation rate, $\langle \epsilon_f \rangle$, is negligible when compared with the wave breaking dissipation rate, $\langle \epsilon_b \rangle$.

In comparison with Battjes and Janssen's model, Thornton and Guza's description of the broken wave height distribution represents observations more accurately. First, similarly to Tajima's model, Thornton and Guza treat the total distribution for all waves, $p(H)$, as Rayleigh, even after the waves start to break. Their experimental results support this assumption. Second, instead of calculating a breaking wave height for each depth, they assume that, at every depth, waves of all heights are breaking. Third, they assume that the fraction of broken waves for each wave height is

$$W(H) = \left(\frac{H_{rms}}{\gamma h} \right)^n \left[1 - exp\left(-\left(\frac{H}{\gamma h} \right)^2 \right) \right] \leq 1 \qquad (2.20)$$

where, from observations, they set $n = 2$ and suggest $\gamma = 0.42$. However, γ remains as an adjustable parameter of the model, similar to γ in Battjes and Janssen's model. Note that, for a given depth h, the larger the wave height, H, the bigger the fraction of broken waves, $W(H)$. The distribution of breaking wave heights is therefore

$$p_b(H) = W(H)p(H) \qquad (2.21)$$

with $p(H)$, the total distribution for all waves, being a Rayleigh distribution.

In comparison, Tajima's model assumes a unique breaking wave height for each depth. However, Tajima's description of wave breaking can be refined by prescribing the incident wave in terms of a probabilistic distribution of heights and periods, $p(H, T)$. Each wave component, of H and T, is propagated using Tajima's monochromatic model. The final result is the average of all components weighted by the prescribed probability density function (This procedure is detailed in Chapter 3). In this case, the breaking wave height becomes no longer constant for each depth and, for a broad range of wave heights, there will be a fraction of broken waves. The resulting characterization of wave breaking is similar to Thornton and Guza's. However, the probabilistic description based on Tajima's monochromatic model uses

well-established probability distributions. Therefore, it does not need to assume an expression for the fraction of broken waves, $W(H)$, and no fitting parameter is involved.

Thornton and Guza's approach to compute the dissipation rate is similar to Battjes and Janssen's. They also simulate the wave breaking energy dissipation to be that of a bore, (2.17). According to their statistical description, in which they allow for broken waves of different heights, they calculate an average rate of energy dissipation, $\langle \epsilon_b \rangle$. This average rate is calculated by multiplying the energy dissipation rate for each wave height, H, by its probability of wave breaking, $p_b(H)$, and integrating for all values of H:

$$\langle \epsilon_b \rangle = \frac{B^3}{4} \rho g \frac{\bar{f}}{h} \int_0^\infty H^3 p_b(H) dH \qquad (2.22)$$

with $p_b(H)$ defined by (2.21). The result of this integral is

$$\langle \epsilon_b \rangle = \frac{3\sqrt{\pi}}{16} \rho g B^3 \bar{f} \frac{H_{rms}^5}{\gamma^2 h^3} \left[1 - \frac{1}{\left(1 + (H_{rms}/\gamma h)^2 \right)^{5/2}} \right] \qquad (2.23)$$

where B^3 is a constant of order 1, similar to α in Battjes and Janssen (1978). The authors state that B^3 should be calibrated for the particular area of study, since the model is notably sensitive to this parameter.

2.1.4 Model comparison

Here, we compare the three spectral wave models presented above. We note that Battjes and Janssen's and Thornton and Guza's models do not allow representing monochromatic incident waves defined by a single wave height and period. These models are developed for narrow spectral incident waves, with wave heights defined by a Rayleigh distribution. Tajima's model allows not only for spectral incident waves, but also for purely monochromatic waves, of given H and T. This makes Tajima's model valid to simulate statistically defined wave conditions, where we need to propagate wave components, of H and T, and average the results according to a probability distribution. This approach will be used in Chapter 3.

Unlike Tajima, Battjes and Janssen's and Thornton and Guza's models include parameters that are supposed to be calibrated for each particular location. In Battjes and Janssen (1978), these parameters are γ and α, whose suggested values are 0.8 and 1, respectively. In Thornton and Guza (1983), they are γ, whose suggested value is 0.42, and B, which they expect to be of the order of 1. However, to fit the experimental results in their paper, Thornton and Guza vary the value of B from 0.8 to 1.72 depending on the case they analyze. They finally suggest the value $B = 0.8$ for laboratory conditions and $B = 1.5$ for field conditions to fit their results. Note that this parameter appears as B^3 in the expression of Thornton and Guza's dissipation rate, $\langle \epsilon_b \rangle$. Therefore, the difference between the suggested values yields a factor of $(1.5/0.8)^3 \sim 7$ in the value of $\langle \epsilon_b \rangle$.

Since our goal is to develop a fully predictive hydrodynamic model, we must define model parameters a priori. We will therefore use the parameter values the authors suggest when comparing Battjes and Janssen's and Thornton and Guza's models with Tajima's. We will also analyze the sensitivity of these models to changes in the parameter values. Note that Tajima's model is already fully predictive, and does not require any parameter to be calibrated.

Figure 2-1 shows a comparison between different model results for an incident wave propagating over a plane bottom, according to the experimental set-up reported by Okayasu and Katayama (1992). In case 2 of their experiments, Okayasu and Katayama propagated a random wave, characterized by a Bretschneider-Mitsuyasu spectrum (Mitsuyasu, 1970), with a significant incident wave height $H_i = 8.28$ cm and a peak period $T_{peak} = 1.26$ s. In the figure, results by Tajima, Battjes and Janssen, and Thornton and Guza are compared with average measured wave heights. The experimental values shown in the figure are significant wave heights obtained from spectral analysis based on linear theory. Therefore, these results must be directly compared with linear wave height results. Note that the inputs and outputs of the three discussed models are *rms* values, while the results presented in the figure are *significant* values; the conversion has been done by assuming $H_s = 1.4 H_{rms}$. The values of the parameters recommended by the authors are used in the models by Battjes

Figure 2-1: Comparison of measured and predicted significant wave heights, Okayasu and Katayama (1992), case 2. Measurements (circles), Tajima's predicted linear wave heights (solid line), Battjes and Janssen's predictions (dashed line), and Thornton and Guza's predictions (dashed-dotted line). As a general convention for bottom profile graphs, x increases in the direction of wave propagation and is 0 at the still water shoreline; $z = 0$ corresponds to the still water level.

and Janssen ($\alpha = 1$, $\gamma = 0.8$) and by Thornton and Guza ($B = 0.8$, $\gamma = 0.42$). Recall that because all parameters in Tajima's model are fixed, further calibrations are not necessary. Tajima's linear wave heights give a good agreement with measurements. Battjes and Janssen's and Thornton and Guza's results in the surf zone are similar to Tajima's linear values, so their linear wave models seem to be of comparable accuracy to Tajima's in this case. In the intermediate depth zone, Tajima's and Battjes and Janssen's linear wave heights slightly underpredict the experimental results. Overall, average relative errors of the three models are comparable, and of the order of 10%.

Figure 2-2 refers again to the plane bottom case, and shows the effect of varying the energy dissipation parameter (B in Thornton and Guza's model and α in Battjes

Figure 2-2: Comparison of measured and predicted significant wave heights; Okayasu and Katayama (1992), case 2. Measurements (circles), Tajima's predicted linear wave heights (solid line). Upper plot: Thornton and Guza's predictions for $B = 0.5$ (dotted line), $B = 0.8$ (dashed-dotted line), and $B = 1.5$ (dashed line). Center plot: Battjes and Janssen's predictions for $\alpha = 0.5$ (dotted line), $\alpha = 1$ (dashed-dotted line), and $\alpha = 1.5$ (dashed line).

32

and Janssen's). In their paper, Thornton and Guza (1983) use values for B between 0.8 and 1.72 to get best fits to their experimental results. $B = 0.8$ is the recommended value for laboratory conditions. Indeed, the figure shows that any further increase of the parameter beyond the value $B = 0.8$ results in a greater underprediction of the wave height. The value $B = 1.5$, recommended for field conditions, yields an underprediction of as much as 35% relative to measurements. On the other hand, a value of $B = 0.5$, smaller than the recommended one, yields overpredictions of the wave height in the surf zone, where the accuracy of the results is most crucial. Battjes and Janssen's model exhibits a smaller sensitivity on the parameter α. This was expected, since the parameter α is replaced by B^3 in Thornton and Guza's formulation, notably increasing the influence of the parameter value on the model results. From further numerical tests, it is seen that the sensitivity of Battjes and Janssen's and Thornton and Guza's model to the other parameter, γ, is smaller.

Figure 2-3 shows a comparison for a barred beach set-up, according to case 3 in Okayasu and Katayama's (1992) experiments. The bottom has positive and negative slopes of 1:20. The incident wave is random, defined by a Bretschneider-Mitsayasu spectrum with an incident significant wave height of $H_i = 5.67$ cm and $T_{peak} = 0.945$ s. Tajima's model and Battjes and Janssen's model with suggested parameter values ($\alpha = 1$, $\gamma = 0.8$) give very good agreement with measurements. Thornton and Guza's model, using suggested parameter values for laboratory conditions ($B = 0.8$, $\gamma = 0.42$), gives about a 10% underprediction while, if the parameter field values are used ($B = 1.5$, $\gamma = 0.42$), the underprediction is about 40% relative to measurements.

Finally, Figure 2-4 shows a comparison for a barred beach, following the experiments of Wang et al. (2002). The experimental results shown here correspond to the plunging breaker case cited in the aforementioned paper. The incident significant wave height is $H_i = 0.23$ m and the peak wave period is $T_{peak} = 3.0$ s. The angle of incidence is 10°. Tajima's model prediction agrees very well with the experimental values, while Battjes and Janssen's and Thornton and Guza's models overpredict them. Thornton and Guza's results have an average error of about 10%, while Battjes and Janssen's model leads to maximum overpredictions of 30% with respect to the
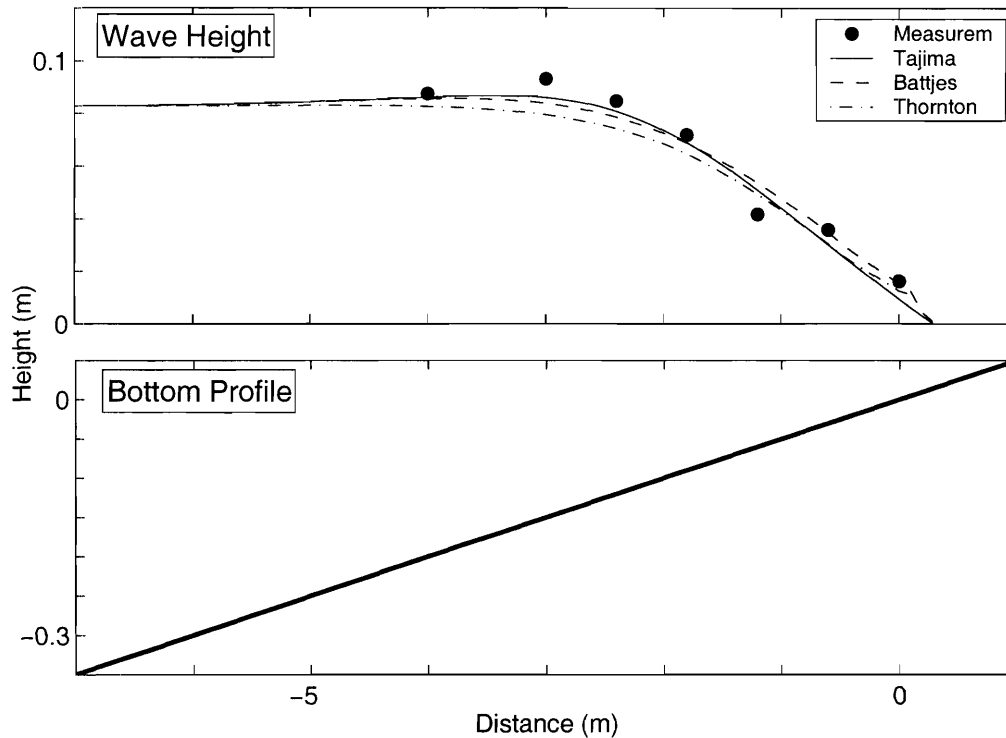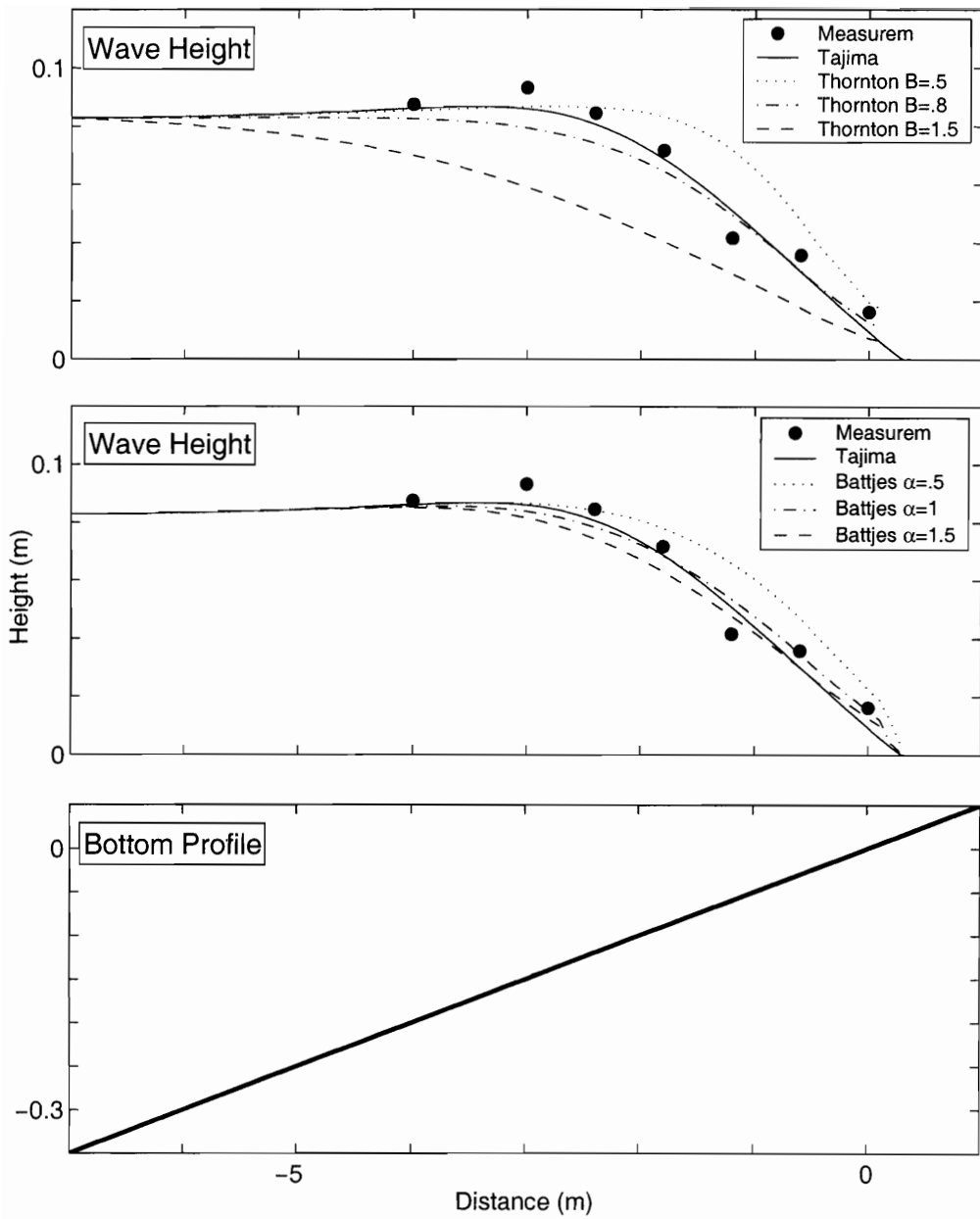
33
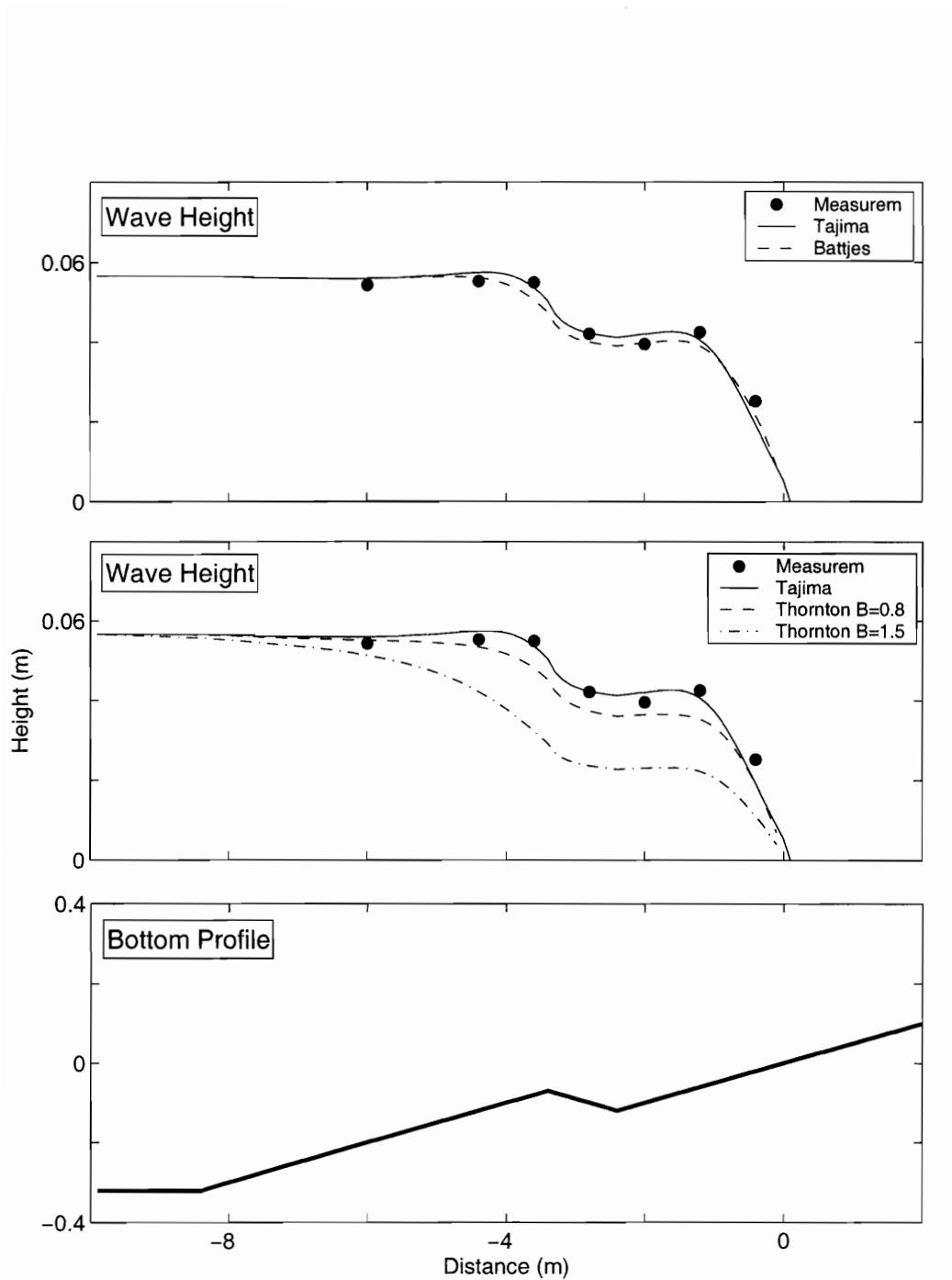
Figure 2-3: Comparison of measured and predicted significant wave heights; Okayasu and Katayama (1992), case 3. Measurements (circles), Tajima's predicted linear wave heights (solid line). Upper plot: Battjes and Janssen's predictions (dashed line). Center plot: Thornton and Guza's predictions for $B = 0.8$ (dashed line) and $B = 1.5$ (dashed-dotted line).
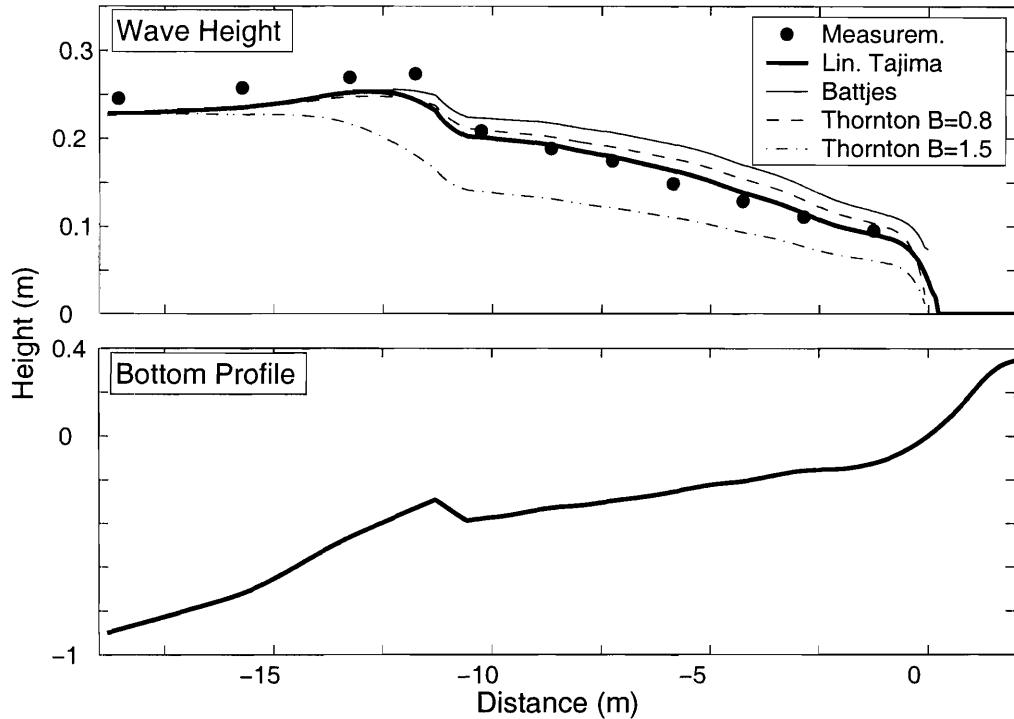
Figure 2-4: Comparison of measured and predicted significant wave heights; Wang et al. (2002), plunging breaker case. Measurements (circles), Tajima's predicted linear wave heights (thick solid line), Battjes and Janssen's predictions (thin solid line), Thornton and Guza's predictions for B=0.8 (dashed line) and B=1.5 (dotted line).

observed values in the surf zone. Note that Thornton and Guza's model, with the energy dissipation parameter value suggested for field conditions. $B = 1.5$, strongly underpredicts the observed results.

In conclusion, Tajima's model yields the most accurate predictions of the experiments in the three analyzed cases. Average relative errors of the three models are summarized in Table 2.1, supporting this conclusion. In addition, Battjes and Janssen's and Thornton and Guza's models have the drawback of introducing adjustable parameters, which significantly affect model results. The authors claim that parameter adjustment can be used as a tool for improving the accuracy of the model results. However, these parameters need to be calibrated for the location of study, and this contradicts the concept of a fully-predicting hydrodynamic model, such as Tajima's.

Table 2.1: Average relative errors of the three models with respect to measurements for the three experimental cases analyzed in this section. Battjes and Janssen's and Thornton and Guza's results correspond to the recommended parameter values for laboratory conditions.

Experiment	Tajima	Battjes	Thornton
Okayasu and Takayama (case 2)	9%	9%	13%
Okayasu and Takayama (case 3)	3%	4%	9%
Wang et al. (plunging case)	6%	17%	11%

2.2 Surface roller model

The concept of a surface roller was first introduced by Svendsen (1984) to explain the increase of the return current observed inside the surf zone with respect to existing theoretical predictions. The surface roller acts as a reservoir of wave energy dissipated by wave breaking. Only part of this energy is immediately transferred to turbulent energy, while the rest is temporarily stored in the surface roller. The surface roller introduces a new forcing term that accounts for the observed increase in return flow velocity.

Svendsen's surface roller model, however, tends to overpredict the return current. Improved models have therefore been developed. Here, we present Tajima's (2004) model, which is based on Dally and Brown's (1995), as well as the model introduced by Nairn et al. (1990) and later improved by Deigaard (1993) and Stive and De Vriend (1994). We compare these two approaches and conclude that they yield similar results.

2.2.1 Tajima's model

Tajima (2004) follows Dally and Brown (1995), and assumes the surface roller energy, E_{sr}, to be proportional to the roller cross-sectional area, S_{sr}, and to the wave phase velocity, C, according to

$$E_{sr} = \frac{\rho S_{sr} C^2 / 2}{L} \qquad (2.24)$$

where L is the wavelength. The volume flux due to the surface roller, which causes an increase in the return current, is

$$\vec{q}_{sr} = \frac{S_{sr}}{T}\vec{n} = \frac{2E_{sr}}{\rho C}\vec{n} \qquad (2.25)$$

The surface roller also introduces contributions to the momentum balance equations. The momentum flux terms due to the surface roller play a similar role to those of the wave radiation stress tensor components (see Section 4.1 for details) and modify the value of the mean water elevation, $\bar{\eta}$.

As mentioned before, the energy of the surface roller comes from wave breaking and is eventually dissipated into turbulent energy. Following Dally and Brown (1995), Tajima assumes the energy balance equation for the surface roller to be of the form

$$\alpha\nabla(EC_g\vec{n}) + \nabla(E_{sr}C\vec{n}) = -\frac{K_{sr}}{h}E_{sr}C \qquad (2.26)$$

where α is the fraction of the broken wave energy that goes into the surface roller and K_{sr} is a proportionality constant. While Dally and Brown assume that all the broken wave energy goes into the surface roller, and therefore take $\alpha = 1$, Tajima assumes that only the potential broken wave energy goes into the surface roller. This is based on the consideration that most of the potential wave energy is concentrated near the surface, where the roller develops, while the kinetic energy is distributed over the entire depth and is more unlikely to be supplied to the surface roller. Due to the equipartition between potential and kinetic energy, Tajima assumes $\alpha = 1/2$. To determine the value of K_{sr}, Tajima observes the analogy between wave and surface roller dissipation energy models, and takes $K_{sr} = K_b$, with K_b defined in (2.6). Introducing (2.5) into (2.26) and applying the previous considerations, the complete energy balance equation for the roller reads

$$\nabla(E_{sr}C\vec{n}) = \frac{K_b}{h}\left(C_g\frac{E - E_r}{2} - CE_{sr}\right) \qquad (2.27)$$

Tajima also presents an extension of the roller model for the random wave case,

37

parallel to the extension of his wave model to random conditions. The energy balance equation for the random wave case is similar to (2.27), but replacing the wave energy dissipation term (the first term in the right hand side of (2.27)) by its equivalent in the random wave case (one half times the right hand side in (2.8)). The energy balance equation then reads

$$\nabla(E_{sr}C\vec{n}) = \frac{K_b}{h} \left(\frac{C_g}{2} \exp\left(-\xi_b^2\right) \left[E\left(1 + \xi_b^2\right) - E_r \right] - CE_{sr} \right) \tag{2.28}$$

2.2.2 Stive and De Vriend's model

Nairn et al. (1990) introduce a surface roller model based on similar principles as Tajima's. Equations (2.24) and (2.25), as well as the roller momentum flux contribution, still hold. Nairn et al.'s energy balance equation for the roller reads

$$\nabla \left(EC_g\vec{n} \right) + \nabla \left(E_{sr}C\vec{n} \right) = -2D \tag{2.29}$$

where, unlike Tajima, Nairn et al. assume that all the broken wave energy goes into the roller. To compute the right-hand side of (2.29), they follow Deigaard and Fredsoe (1989) and consider that the roller energy dissipation is due to the work done by the shear stress acting between the roller and the fluid below, τ_r. Therefore, the energy dissipation rate, which has been called $2D$ here for the purpose of making a later analogy to Tajima, is

$$2D = \bar{\tau}_r C \tag{2.30}$$

From balance of forces on the roller, the shear stress is

$$\bar{\tau}_r = \frac{\rho g S_{sr} \sin \alpha}{L} \tag{2.31}$$

where $\sin \alpha$ would correspond to the wave-front slope, which is usually assumed to be 0.1 or less (Ruessink et al., 2001).

Stive and De Vriend (1994) deduce the energy balance equation from momentum conservation and reach a discrepancy with equation (2.29), since they obtain a factor

of 2 multiplying the roller energy term. From the results of Deigaard (1993), they show that the discrepancy comes from the fact that Nairn et al.'s formulation is missing a term in the energy balance equation. Since the volume of water in the roller is changing, there is an exchange of water between the roller and the organized wave motion, leading to momentum transfer and a corresponding energy dissipation term, omitted by Nairn et al. After introducing this extra term, the energy balance equation for the roller, (2.29), takes the form

$$\nabla \left(EC_g \vec{n} \right) + \nabla \left(2E_{sr}C\vec{n} \right) = -2D = -\bar{\tau}_r C \tag{2.32}$$

which is similar to Tajima's, (2.26).

2.2.3 Model comparison

The formulation of the surface roller models by Tajima (2004) and Stive and De Vriend (1994) is very similar. For comparison, we model the wave energy dissipation term in the way suggested by Tajima, the validity of which was shown in Section 2.1:

$$\nabla \left(EC_g \vec{n} \right) = -\frac{K_b C_g}{h} \left(E - E_r \right) \tag{2.33}$$

Then, the roller energy balance equation both for Tajima's and Stive and De Vriend's models can be written in the form

$$\nabla \left(E_{sr}C\vec{n} \right) = \frac{K_b C_g}{h} \frac{E - E_r}{2} - D \tag{2.34}$$

where the models only differ in the expression for D. In Tajima (2004),

$$D = \frac{K_b}{h} C E_{sr} = K_b E_{sr} \sqrt{\frac{g}{h}} \tag{2.35}$$

while, in Stive and De Vriend (1994),

$$D = g \sin \alpha \frac{E_{sr}}{C} = \sin \alpha E_{sr} \sqrt{\frac{g}{h}} \tag{2.36}$$

39

where we have assumed shallow water, so that $C = \sqrt{gh}$. Both dissipation rates differ only by a factor of proportionality, $K_b / \sin \alpha$, which depends on the beach slope. For a beach slope of 1:30, and assuming $\sin \alpha = 0.1$, the ratio between Tajima's and Stive and De Vriend's dissipation rates is $K_b / \sin \alpha = 1.6$. Therefore, we expect similar results from the two surface roller models.

Figure 2-5 shows mean water level and undertow predictions for case 6N in the experiments conducted by Hamilton and Ebersole (2001). In this experimental case, a monochromatic wave with period T=2.5 s was propagated on a 1:30 concrete beach, from a depth of 0.667 m, where the wave height is 0.182 m and its angle of incidence is 10°. The experimental results are compared with three runs of Tajima's hydrodynamic model: (i) without accounting for a surface roller; (ii) with its own (Tajima, 2004) surface roller model; (iii) with Stive and De Vriend's (1994) surface roller model, assuming $\sin \alpha = 0.1$. Results from both surface roller models are quite similar and, in both cases, the inclusion of the roller improves the fit of the experimental results.

Figure 2-6 shows mean water level and undertow predictions for case 8E in Hamilton and Ebersole (2001). The experimental conditions are similar to case 6N cited above, but the wave is now irregular, following a TMA spectrum (Bouws et al., 1985). The spectral characteristics were chosen so that the significant wave height is the same as the wave height in the monochromatic case, case 6N. The peak period is again $T_p = 2.5s$. As shown in the figure, both models yield accurate predictions of the mean water elevation, with an average error of about 2 mm, while the mean water elevation is of the order of 1 cm. However, when predicting the undertow, Tajima provides better results, with an average relative error of 29%, while Stive and De Vriend consistently overpredict it, yielding an average relative error of 56%. Since the ratio between Tajima's and Stive and De Vriend's dissipation rates is 1.6 in this case, Tajima's surface roller dissipates energy more quickly, and therefore yields a milder increase of the undertow. This is usually the case, since the dissipation rates ratio, $K_b / \sin \alpha$, is greater than one but for very mild slopes. Note that, in this case, the average predictions without considering the roller are globally the most accurate in magnitude (average relative error of 20%), although they underpredict the undertow
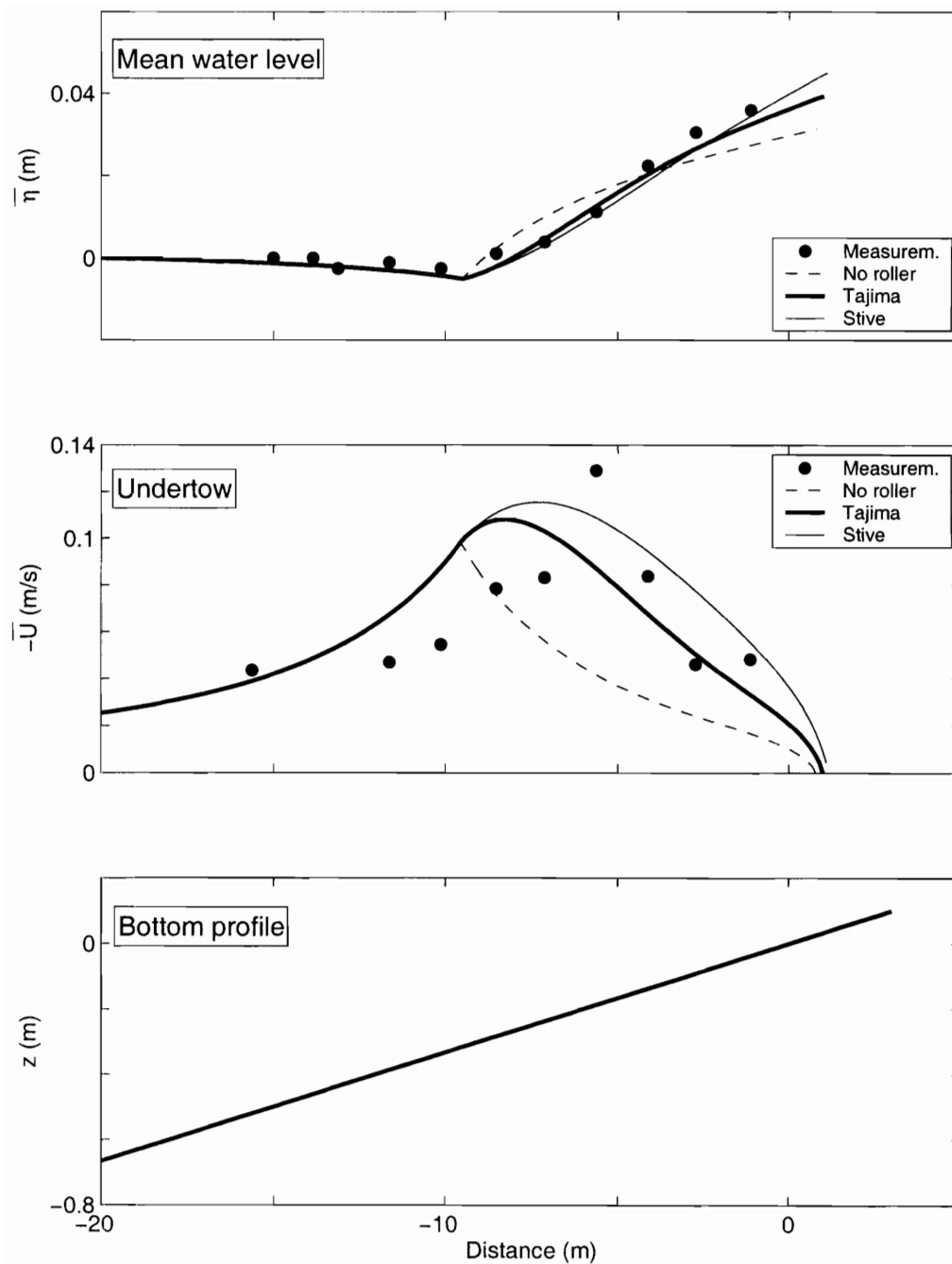
Figure 2-5: Comparison of measured (Hamilton and Ebersole, 2001, case 6N, monochromatic wave) and predicted mean water level and undertow. Measurements (circles), predictions without surface roller (dotted lines), predictions with Tajima's surface roller (thick solid line), and predictions with Stive and De Vriend's surface roller (thin solid line).
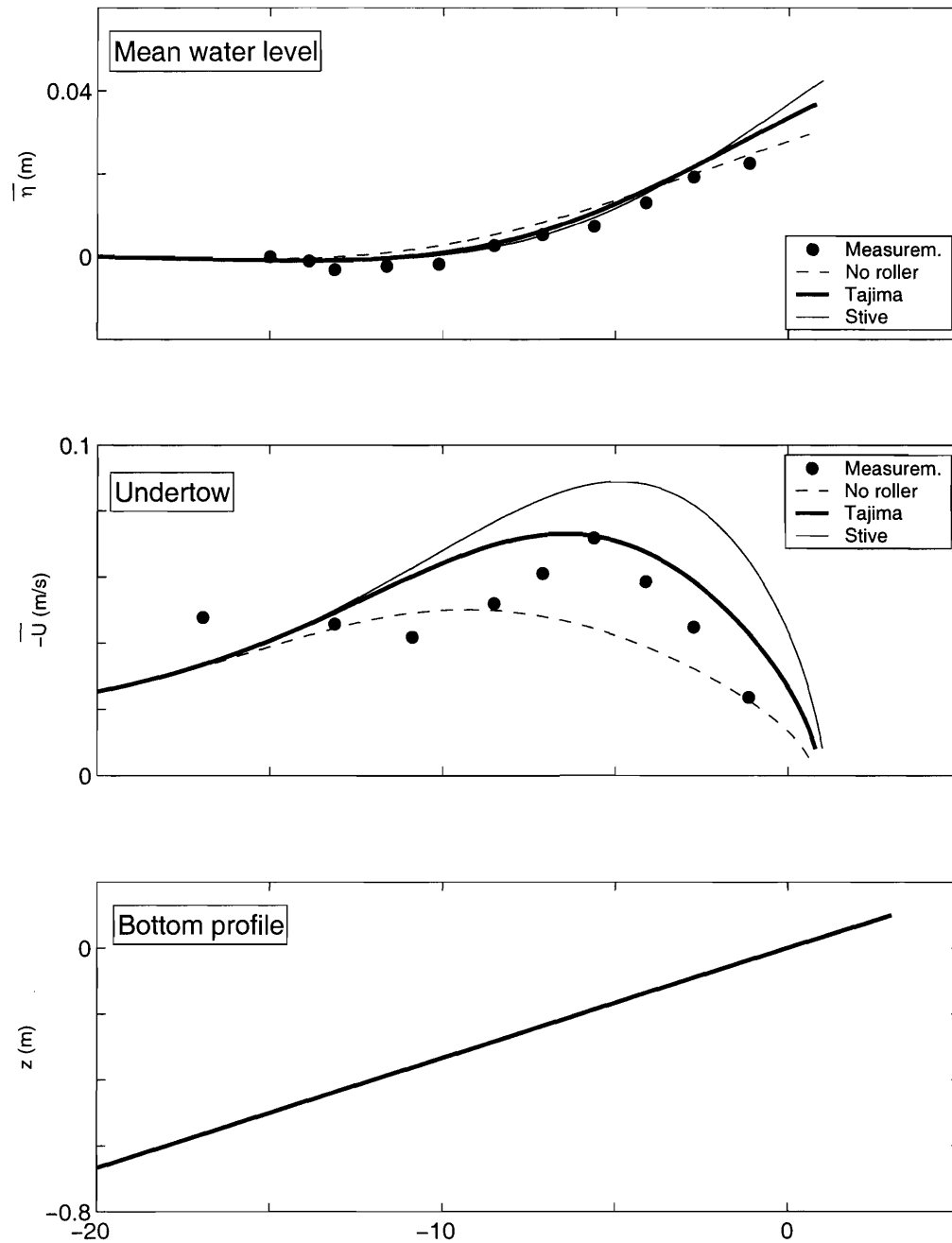
Figure 2-6: Comparison of measured (Hamilton and Ebersole, 2001, case 8E, spectral wave) and predicted mean water level and undertow. Measurements (circles), predictions without surface roller (dotted lines), predictions with Tajima's surface roller (thick solid line), and predictions with Stive and De Vriend's surface roller (thin solid line).

in the crucial nearshore region, where Tajima's predictions yield the best fit.

The average errors of the models' predictions are summarized in Tables 2.2 (Errors in mean water elevation) and 2.3 (Errors in the undertow). These tests show that Tajima's surface roller model's accuracy is comparable or greater than Stive and De Vriend's, supporting the choice of the former in our formulation.

Table 2.2: Average absolute errors (in mm) in the mean water level ($\bar{\eta}$) predictions of the surface roller models with respect to measurements.

Experiment	No roller	Tajima	Stive
Hamilton and Ebersole (case 6N)	4.9 mm	2.4 mm	2.3 mm
Hamilton and Ebersole (case 8E)	2.6 mm	2.3 mm	2.1 mm

Table 2.3: Average relative errors in the undertow ($\bar{U}$) predictions of the surface roller models with respect to measurements.

Experiment	No roller	Tajima	Stive
Hamilton and Ebersole (case 6N)	44%	30%	34%
Hamilton and Ebersole (case 8E)	20%	29%	56%

2.3 Nearshore current model

In this section, we summarize the formulation of the nearshore current model presented by Tajima (2004), which will also be used in this thesis, as part of the generalized hydrodynamic model for unsteady conditions.

Tajima's nearshore current model is a quasi-three dimensional model. Vertically, it divides the whole depth into two layers. One layer extends from the beach bottom to the wave trough, while the other comprises the region above the trough level. In each of these layers, he applies the two-dimensional horizontal, vertically integrated, and time-averaged momentum equations. The model accounts for current-current and wave-current interactions. Boundary conditions are applied using a modified version of the bottom boundary layer model introduced by Madsen (1994).

Here, we show the more general quasi-three dimensional formulation. In Chapter 4, we will restrict the model to normally incident waves and neglect alongshore (y) variation.

Governing equation

In the model by Tajima (2004), the nearshore mean current velocity below the trough level is given by

$$\rho \nu_t \frac{\partial \vec{U}}{\partial z} = \vec{\tau}_c \simeq \vec{\tau}_{cb} + \frac{\vec{\tau}_{cs} - \vec{\tau}_{cb}}{h_{tr}} z \tag{2.37}$$

where the current shear stress is assumed to vary linearly in depth. Here, ν_t is the turbulent eddy viscosity, $\vec{\tau}_c$ is the mean current shear stress vector, $\vec{\tau}_{cb}$ and $\vec{\tau}_{cs}$ are respectively the bottom and trough shear stress vectors, $h_{tr} = h_0 + \bar{\eta} - \frac{H}{2}$ is the trough water depth, and z is the elevation above the bottom. Above the trough level, the mean current velocity is assumed constant and equal to the current velocity at the trough level.

Turbulent eddy viscosity

Close to the bottom, shear stress can be considered constant, and the turbulent eddy viscosity is assumed to vary linearly with depth. At larger distances from the bottom, shear stress increases due to the effect of broken waves, and the rate of increase of the turbulent eddy viscosity must be faster than the previous linear law. Based on this consideration, the turbulent eddy viscosity is defined in the following way:

$$\nu_t = \begin{cases} \kappa u_{*c} z & \text{if } \delta \leq z \leq z_m \\ \kappa u_{*s} z \sqrt{\frac{z}{h_{tr}}} & \text{if } z_m < z \leq h_{tr} \end{cases} \tag{2.38}$$

where $\kappa = 0.4$ is Von Kármán's constant; $u_{*c} = \sqrt{|\vec{\tau}_{cb}|/\rho}$ is the shear stress velocity at the bottom; $u_{*s} = \sqrt{|\vec{\tau}_{cs}|/\rho + u_{*B}^2}$ is the shear stress velocity at the surface, with $u_{*B}^2 = M \left(\frac{D}{2\rho}\right)^{1/3}$ being the characteristic turbulent velocity due to the breaking wave energy dissipation, where M is taken as $M = \kappa = 0.4$; $z_m = h_{tr} u_{*c}^2/u_{*s}^2$ is the depth where the two eddy viscosity profiles match; and δ is the wave bottom boundary layer thickness, determined from Madsen's (1994) model.

44

Bottom boundary condition

Madsen's (1994) modified wave-current bottom boundary layer model is used in Tajima (2004) to provide the bottom boundary condition for the current model. The mean current velocity at the outer edge of the boundary layer, $z = \delta$, is

$$\vec{U}_\delta = \frac{\vec{\tau}_{cb}}{\kappa \rho u_{*m}} \ln \left(\frac{\delta}{z_0} \right) \tag{2.39}$$

where $z_0 = k_N/30$. k_N is the equivalent Nikuradse (1933) roughness of the bottom. The maximum combined wave-current bottom shear velocity, u_{*m}, is defined by

$$u_{*m}^2 = \frac{C_\mu \tau_{wm}}{\rho} \tag{2.40}$$

with

$$C_\mu = \sqrt{1 + 2|\cos \phi_{cw}| \frac{|\vec{\tau}_{cb}|}{\tau_{wm}} + \left(\frac{|\vec{\tau}_{cb}|}{\tau_{wm}} \right)^2} \tag{2.41}$$

$$\tau_{wm} = \frac{1}{2} \rho f_{cw} u_{bm}^2 \tag{2.42}$$

Here, ϕ_{cw} is the angle between waves and currents. The boundary layer thickness, δ, is given by

$$\delta = A \frac{\kappa u_{*m}}{\omega} \tag{2.43}$$

where

$$A = \exp \left[2.96 \left(\frac{C_\mu A_{bm}}{k_N} \right)^{-0.071} - 1.45 \right] \tag{2.44}$$

and $A_{bm} = u_{bm}/\omega$ is the amplitude of the near-bottom wave orbital velocity, u_{bm}, whose value is provided by Tajima's non-linear wave model. According to Madsen (1994), f_{cw} can be approximated as a function of the dimensionless parameter $X = C_\mu A_{bm}/k_N$ in the following way

$$f_{cw} = max \begin{cases} C_\mu \exp(7.02 X^{-0.078} - 8.82) & \text{if } 0.2 < X < 10^2 \\ C_\mu \exp(5.61 X^{-0.109} - 7.30) & \text{if } 10^2 < X < 10^4 \\ C_\mu \exp(5.50 X^{-0.120} - 7.02) & \text{if } 10^4 < X < 10^6 \end{cases} \tag{2.45}$$

Solution for mean current profile

The mean current profile is obtained by solving (2.37), with ν_t given by (2.38) and the bottom boundary condition given by (2.39). The vertical profile of the mean current can be expressed as

$$\vec{U} = \begin{cases} \vec{A}_1 \ln \frac{z}{z_0} & \text{if } z_0 \leq z \leq \delta \\ \vec{U}_\delta + \vec{A}_2 \ln \frac{z}{\delta} + \vec{A}_3 \frac{z-\delta}{h_{tr}} & \text{if } \delta < z \leq z_m \\ \vec{U}_{z_m} + \vec{A}_4 \left(\sqrt{z} - \sqrt{z_m} \right) & \text{if } z_m < z \leq h_{tr} \\ \vec{U}_s & \text{if } h_{tr} < z \leq h + \eta \end{cases} \tag{2.46}$$

with

$$\begin{pmatrix} \vec{A}_1 \\ \vec{A}_2 \\ \vec{A}_3 \\ \vec{A}_4 \end{pmatrix} = \begin{pmatrix} \frac{\vec{\tau}_{cb}}{\rho \kappa u_{*m}} \\ \frac{\vec{\tau}_{cb}}{\rho \kappa u_{*c}} \\ \frac{\vec{\tau}_{cs} - \vec{\tau}_{cb}}{\rho \kappa u_{*c}} \\ \frac{2}{\rho \kappa u_{*s}} \left(\frac{\vec{\tau}_{cs} - \vec{\tau}_{cb}}{\sqrt{h_{tr}}} + \vec{\tau}_{cb} \sqrt{\frac{h_{tr}}{z z_m}} \right) \end{pmatrix} \tag{2.47}$$

where $\vec{U}_\delta$, $\vec{U}_{z_m}$ and $\vec{U}_s$ are the current velocity vectors at $z = \delta$, $z = z_m$ and $z = h_{tr}$, so that the mean current profile is continuous.

Integrated mass and momentum conservation equations

The unknown variables in the previous formulation are the bottom shear stress, $\vec{\tau}_{cb} = (\tau_{cbx}, \tau_{cby})$, the trough shear stress, $\vec{\tau}_{cs} = (\tau_{csx}, \tau_{csy})$, and the mean water elevation, $\bar{\eta}$, which is needed to calculate the shear stresses. These five unknowns are determined from the following set of equations: Depth-integrated continuity equation, depth-integrated momentum equations above the trough level (in x- and y-directions), and depth-integrated momentum equations over the entire depth (in x- and y-directions). In Tajima (2004, §4.4.5 and Appendix A), these equations are derived for the steady case. The more general unsteady equations, which govern the unsteady model developed in this thesis, are presented in Chapter 4.

46

Chapter 3

Validation of the hydrodynamic model for random wave conditions

In his hydrodynamic model for uniform, long straight beaches, Tajima (2004) considers two possible kinds of incident waves: Periodic or random. Periodic waves are just monochromatic waves defined by a single wave height and period. Tajima's random wave model assumes a narrow-banded spectrum which is represented by a constant wave period, corresponding to the spectral peak, and Rayleigh distributed wave heights.

The purpose of this chapter is to check the validity of Tajima's random model by comparing it with a more realistic representation of random waves. For this comparison, we will use the description afforded by the joint probability distributions for wave heights and periods proposed by Longuet-Higgins (1975, 1983).

In the following sections, we first present some relevant joint probability distributions for wave heights and periods. Then, we compare the probabilistic descriptions by Longuet-Higgins (1975, 1983) with the JONSWAP spectral model. These probabilistic descriptions are used to determine the validity of Tajima's random wave model, through numerical experiments for plane and barred beach topographies. The results of this validation are summarized in the conclusion.

3.1 Random wave models

A number of probability models have been suggested to describe the joint distribution of wave heights and periods. Among the most relevant ones are the models proposed by Longuet-Higgins (1975, 1983), Cavanié et al. (1976) and Lindgren (1972) and Lindgren and Rychlik (1982). An insightful comparison between these models can be found in Srokosz and Challenor (1987).

3.1.1 Cavanié et al.

Cavanié et al. (1976) assume a sinusoidal profile for each wave in the random series. Under this assumption, which is reasonable for narrow banded spectra, they obtain a joint distribution for wave heights and periods defined by wave positive maxima. According to Srokosz and Challenor (1987), Cavanié et al.'s distribution provides a good agreement with experimental observations for narrow banded spectra and succesfully accounts for the asymmetry in the wave period distribution that observations show. Its main disadvantage, as pointed out by Longuet-Higgins (1983), is that it characterizes the spectral width by using a width parameter, ϵ, defined as

$$\epsilon = \sqrt{1 - \frac{m_2^2}{m_0 m_4}} \tag{3.1}$$

This parameter involves the fourth moment of the spectral density, m_4. For practical purposes, the use of this fourth moment is inadequate, since its value is quite sensitive to the behavior of the spectrum at high frequencies, where experimental noise may introduce critical disturbances.

3.1.2 Lindgren et al.

Lindgren (1972) and Lindgren and Rychlik's (1982) approach assumes Gaussian waves and defines a stochastic *model process* to evaluate the probability distribution. The *model process* describes the surface elevation next to a crest, and is therefore used to estimate the joint distribution of wave heights and periods near the crest, conditioned

on the value of the wave height at the crest. The unconditional joint distribution is then obtained by integrating this conditional distribution over all possible wave heights. Therefore, in contrast with Cavanié et al.'s and Longuet-Higgins's models, Lindgren's probability distribution does not have a closed-form analytical expression, but it is defined through a *model process* approach, and requires a huge amount of computation for its evaluation. This makes it inconvenient for most practical applications, where a simpler procedure for evaluating the probability distribution would be preferable.

3.1.3 Longuet-Higgins (1975)

In 1975, Longuet-Higgins introduced a joint probability distribution for wave heights and periods (Longuet-Higgins, 1975) that he would revise in a later paper (Longuet-Higgins, 1983). The 1975 model was derived from the statistical analysis of the wave envelope, under the hypothesis of a Gaussian sea surface and a narrow-banded spectrum. The joint probability density function reads

$$f_{\xi\tau} = \frac{\xi^2}{\nu} \frac{2}{\sqrt{\pi}} \exp\left\{-\xi^2\left[1 + \left(\frac{\tau-1}{\nu}\right)^2\right]\right\} \, , \, \xi \geq 0 \, , \, -\infty < \tau < \infty \qquad (3.2)$$

where ξ and τ are the non-dimensional wave height and period, defined as

$$\begin{aligned} \xi &= \frac{H}{H_{rms}} \\ \tau &= \frac{T}{T_{ave}} \end{aligned} \qquad (3.3)$$

H and T are the wave height and period, H_{rms} is the root mean square wave height, and T_{ave} is the average wave period, which can be expressed as

$$\begin{aligned} H_{rms} &= 2\sqrt{2m_0} \\ T_{ave} &= 2\pi\frac{m_0}{m_1} \end{aligned} \qquad (3.4)$$

where m_n denotes the nth moment of the spectral density, $S(\omega)$,

$$m_n = \int_0^\infty \omega^n S(\omega)d\omega \qquad (3.5)$$

49

$\omega = 2\pi/T$ is the wave radian frequency. ν is a spectral width parameter defined (Longuet-Higgins, 1983) as

$$\nu = \sqrt{\frac{m_0 m_2}{m_1^2} - 1}$$ (3.6)

The original notation of the 1975 paper has been modified here, for consistency with the notation used in the rest of this chapter.

The marginal density function of the non-dimensional wave height, f_ξ, is Rayleigh, which is consistent with observations. The marginal density of the non-dimensional wave period, f_τ, is a symmetric bell-shaped function, although not Gaussian. The conditional density of τ for a given ξ is Gaussian.

In this formulation, Longuet-Higgins allows for negative values of τ, which are unrealistic. To avoid this, we will adopt a truncated version of Longuet-Higgins's 1975 distribution, defined as follows:

$$f_{\xi\tau} = L\frac{2\xi^2}{\nu\sqrt{\pi}} \exp\left\{-\xi^2\left[1 + \left(\frac{\tau-1}{\nu}\right)^2\right]\right\}$$ (3.7)

where

$$\xi \geq 0$$
$$\tau \geq 0$$

and

$$L = \frac{2}{1 + \frac{1}{\sqrt{1+\nu^2}}}$$ (3.8)

3.1.4 Longuet-Higgins (1983)

While Longuet-Higgins's 1975 distribution gives a good fit to narrow spectrum data, it does not account for the asymmetry in the distribution of the wave period, T, that is observed for broader spectra. In a later contribution, Longuet-Higgins (1983) refined his theoretical formulation and succeeded in accounting for this asymmetry.

His 1983 density function reads

$$f(\xi, \tau) = \frac{L}{16\nu\sqrt{2\pi}} \frac{\xi^2}{\tau^2} \exp\left\{-\frac{\xi^2}{8}\left[1 + \frac{1}{\nu^2}\left(1 - \frac{1}{\tau}\right)^2\right]\right\} \qquad (3.9)$$

$$\xi \geq 0$$
$$\tau \geq 0$$

where ξ, τ, ν and L were defined in equations (3.3), (3.6), and (3.8).

This distribution is still based on the assumption of narrow-banded spectrum. Longuet-Higgins states that the distribution accurately represents observations provided that $\nu \leq 0.6$; other authors (Srokosz and Challenor, 1987) have suggested that for a good fit with empirical results we must require $\nu \leq 0.4$.

The marginal density of the wave height, f_ξ, is

$$f_\xi = 2\xi e^{-\xi^2} L(\nu) F(\xi/\nu) \; , \; \xi \geq 0 \qquad (3.10)$$

where

$$F(\xi/\nu) = \frac{1}{\sqrt{\pi}} \int_{-\infty}^{\xi/\nu} e^{-\beta^2} d\beta \qquad (3.11)$$

Therefore, f_ξ is almost Rayleigh, but for the correction factor $L(\nu)F(\xi/\nu)$. For large ξ, this correction factor approaches $L(\nu)$ in an exponential fashion, which is in turn close to unity. However, the correction is significant for values of ξ close to 0.

The marginal distribution of τ is

$$f_\tau = \frac{L}{2\nu\tau^2}\left[1 + \frac{1}{\nu^2}\left(1 - \frac{1}{\tau}\right)^2\right]^{-3/2} \; , \; \tau \geq 0 \qquad (3.12)$$

This function captures the asymmetry of the wave period distribution, in a way that is consistent with observations. Note that, for large values of τ, the distribution behaves like $1/\tau^2$. Therefore, the mean period is infinite. This fact is related to convergence issues discussed in the next section.

As Srokosz and Challenor (1987) point out, for obtaining a good fit with experi-

mental data, Longuet-Higgins's (1983) distribution must be compared with statistical values of zero-upcrossing height and period, respectively defined as the maximum vertical distance between two consecutive zero-upcrossings and the time elapsed between consecutive zero-upcrossings. This results from the manner in which the distribution was derived.

3.2 Comparison of probabilistic and spectral descriptions

In this section we are interested in comparing Longuet-Higgins's probability distributions (1975 and 1983) with the spectral description of sea waves provided by the JONSWAP spectrum (Hasselmann et al., 1973). The JONSWAP spectrum was formulated for a developing fetch-limited wind sea, and therefore it allows for narrower and more peaked spectral shapes than a fully-developed sea spectrum. The JONSWAP spectral density is given by

$$S(f) = \alpha g^2 (2\pi)^{-4} f^{-5} \exp\left\{-\frac{5}{4}\left(\frac{f}{f_p}\right)^{-4} + \ln\gamma\exp\left\{-\frac{(f-f_p)^2}{2\sigma^2 f_p^2}\right\}\right\} \tag{3.13}$$

where f_p is the peak frequency, and α, σ, and γ are shape parameters. The usual values of σ are

$$\sigma = \begin{cases} 0.07 & \text{if } f \leq f_p \\ 0.09 & \text{if } f > f_p \end{cases} \tag{3.14}$$

γ is of the order of 3.3, and the value of α depends on the stage of development of the wind sea.

We will compare the energy flux obtained from the JONSWAP spectrum and from Longuet-Higgins's probability distributions at various depths, neglecting dissipation due to bottom friction or wave breaking. The wave energy flux, E_f, of a monochromatic wave of height H is given by

$$E_f = EC_g = \frac{1}{8}\rho g H^2 C_g \tag{3.15}$$

where E is the wave energy density, averaged over a wave period; C_g is the group velocity; and ρ is the water density.

The energy flux of a spectral wave characterized by a JONSWAP spectrum of spectral density $S(f)$, at a given water depth h, is calculated integrating the energy flux contributions over the whole frequency range:

$$E_f(h) = \rho g \int_0^\infty S(f) C_g(f, h) df \tag{3.16}$$

The procedure for calculating the energy flux of a wave characterized by one of Longuet-Higgins's probability distributions is similar. In this case, the energy flux contributions for individual waves are averaged with respect to the probability density function, $f_{\xi\tau}$:

$$E_f(h) = \int_0^\infty \int_0^\infty \widetilde{E}_f(h, \xi, \tau) f_{\xi\tau}(\xi, \tau) d\xi d\tau \tag{3.17}$$

where $\widetilde{E}_f$ is the energy flux of the monochromatic wave with non-dimensional height and period of ξ and τ, respectively. In practice, the integral above is computed by taking a finite number of individual wave components, of H and T, and averaging their contributions. We will refer to this procedure as the *probabilistic wave-by-wave approach*. It consists on calculating the magnitude of interest for a large representative set of monochromatic wave components, of H and T, and then weighting the results using a probability distribution to obtain an average value.

In the previous expression, (3.17), we did not account for the fact that different individual wave components have different periods. In the probabilistic description, we regard the incident random wave as a series of individual monochromatic waves, acting sequentially. Each individual component acts for a time equal to its wave period, which is different for each component. According to this, individual wave components should also be weighted by their period durations, i.e.,

$$E_f(h) = \int_0^\infty \int_0^\infty \widetilde{E}_f(h, \xi, \tau) f_{\xi\tau}(\xi, \tau) T(\tau) d\xi d\tau \tag{3.18}$$

where $T(\tau) = T_{ave}\tau$. However, it is not clear that this conceptual model of a se-

quence of monochromatic waves represents accurately the real sea. Therefore, we will calculate two different averages, according to (3.17) and (3.18), and analyze both results.

Next, we present results of the energy flux comparison for a particular case, defined by normal incident waves with $H_{rms} = 1$ m and $T_{ave} = 5$ s. The corresponding values of the spectral density moments are $m_0 = 0.125$ m^2 and $m_1 = 0.15708$ m^2/s. We further assume a spectral width parameter value of $\nu = 0.4$. To satisfy these moment values, we take $\alpha = 5.363 \cdot 10^{-3}$, $\gamma = 2.55$ and $f_p = 0.164$ s^{-1} as the values of the JONSWAP spectrum parameters. The results, at different depths, are summarized in Table 3.1.

Table 3.1: Energy fluxes of the probability distributions for different water depths, relative to JONSWAP spectrum energy fluxes. The probability distributions are Longuet-Higgins (1975) and Longuet-Higgins (1983), without period weighting (see equation 3.17) or with period weighting (see equation 3.18). Wave breaking and bottom friction are neglected.

	$E_f/E_{f,}$JONSWAP			
Depth (m)	LH75 (No T)	LH75 (T weights)	LH83(No T)	LH83 (T weights)
100	0.9472	1.1038	1.0034	1.3062
50	0.9478	1.1066	1.0086	1.3178
20	0.9260	1.0899	0.9786	1.2693
10	0.9281	1.0869	0.9604	1.2119
5	0.9667	1.1099	0.9895	1.2045
2	1.0673	1.1976	1.0796	1.2744
1	1.0764	1.1960	1.0838	1.2651

To calculate the probabilistic approach results in Table 3.1, we considered 8927 individual components, of H and T, representing a 96.4% of the total probability for the 1975 distribution and a 97.7% for the 1983 distribution. The maximum individual component wave period was 23.4 s.

From the results in Table 3.1, we observe a good agreement between the probabilistic models and the JONSWAP spectrum when the formulation without period weighting, (3.17), is used. When different period durations are accounted for, (3.18), energy flux is overestimated with respect to the JONSWAP spectrum. This overpre-

diction is, however, of the same order of magnitude for different depths. Therefore, from this numerical test, we conclude that the probabilistic approach and the JON-SWAP spectrum description yield consistent results.

However, not all the energy flux values recorded in Table 3.1 are meaningful. Some of the probabilistic approach results are sensitive to the period cut-off we adopt (23.4 seconds in this case), and would unboundedly increase if we allowed for larger and larger wave periods. The problem lies in the way the energy flux is calculated, from (3.17) or (3.18). In these expressions, the wave energy density, E, is proportional to ξ^2, while the group velocity, C_g, is proportional to τ in deep water and constant in shallow water. Therefore, the energy flux integrals are of the form

$$I = \int_0^\infty \int_0^\infty \xi^r \tau^t f_{\xi\tau}(\xi, \tau) d\xi d\tau \qquad (3.19)$$

but for a constant factor. Here, $f_{\xi\tau}$ is the density function (either the 1975 or the 1983 distribution), $r = 2$, and t is a constant whose value ranges from 0 to 2, depending on whether the computation corresponds to shallow or deep water, and whether an extra T term accounting for different period durations is introduced or not. As shown in Appendix A, I is integrable for $t < 4$ for the 1975 distribution, but only for $t < 1$ for the 1983 distribution. This causes the 1983 distribution to yield non-convergent predictions of the energy flux in most cases. The 1975 distribution shows a better convergence behavior, but different authors (Longuet-Higgins, 1983; Srokosz and Challenor, 1987) claim that it represents observations less accurately than the 1983 distribution.

In the momentum equations of the hydrodynamic model, to be introduced in Chapter 4, we are not explicitly interested in the energy flux, but in the radiation stress terms, such as S_{xx} and S_{xy} (defined in (4.2) and (4.3)), which are proportional to ξ^2 and independent of τ, both in deep and shallow water. This makes the integral convergent, even with the 1983 density function, provided that period weighting is not implemented. In Section 3.3, we will show that period weighting does not significantly affect radiation stress predictions. Since the 1983 distribution affords a better

representation of observations, we will adopt the 1983 distribution without period weighting to characterize the incident waves, as justified in the following sections.

The considerations about integrability presented in this section are summarized in Table 3.2.

Table 3.2: Summary of the integrability of energy flux and radiation stress in the probabilistic approach

	Integrability of...	
Distribution, formulation	E_f	Rad. stresses
LH75, without T weighting	Yes	Yes
LH75, with T weighting	Yes	Yes
LH83, without T weighting	Only in shallow water	Yes
LH83, with T weighting	No	No

3.3   Validation of Tajima's random wave model

In the previous section, we showed the consistency of the probabilistic wave-by-wave approach with the JONSWAP spectral model. In this section, we compare different probabilistic descriptions and use them to show the validity of Tajima's (2004) random wave model.

We use Longuet-Higgins's (1975, 1983) probability distributions to model incident random waves more realistically than Tajima's (2004) very narrow distribution, defined by H_{rms} and T_{peak}. Longuet-Higgins's distributions allow us to examine the effects of the spectral width, assumed 0 by Tajima. The *probabilistic wave by wave approach* is used: Individual wave components, of H and T, are propagated using Tajima's linear monochromatic model. Then, mean wave characteristics are calculated, at various positions in- and outside the surf zone, by averaging the results for all individual components, according to the probability density function. The results we are specifically interested in are: Wave heights, radiation stress gradients (dS_{xx}/dx, see (4.2)) and surface roller stress gradients (dR_{xx}/dx, see (4.5)). These two latter stress gradients play a role in the momentum conservation equations, and therefore influence the values of wave set-up and undertow. When calculating stress

gradients, the average of individual wave results may be computed with or without accounting for the effect of different period durations. In the case of wave heights, different periods play no role in the average. As explained in the previous section, due to integrability considerations, averaging with period weighting is only possible for the Longuet-Higgins's (1975) distribution, but not for the later 1983 distribution.

Figures 3-1 to 3-5 show a comparison between Tajima's spectral model and the probabilistic wave-by-wave approach on a plane beach of slope 1:50. The incident wave is characterized by $H_{rms} = 1$ m and $T_{ave} = 5$ s in deep water ($h = 200$ m). The corresponding peak period is $T_{peak} = 6.10$ s, according to the JONSWAP spectrum. The spectral width parameter ranges from $\nu = 0.1$ to $\nu = 0.6$ in the probabilistic approach. Tajima's spectral model assumes an infinitely narrow spectrum, corresponding to $\nu = 0$, and is characterized by a single period. We consider two choices for the characteristic period: The average period, T_{ave}, and the peak period, T_{peak}. Tajima (2004) suggests the latter. However, as shown in the figures, the former yields better agreement with the probabilistic description.

Figure 3-1 compares the wave heights predicted by Tajima's spectral model and by the wave-by-wave approach using Longuet-Higgins's (1983) distribution. The choice of T_{ave} in Tajima's spectral model yields wave heights coincident with the narrow spectrum probabilistic description ($\nu = 0.1$), while the choice of T_{peak} introduces discrepancies. In the off-shore region, $x < -150$ m, the average relative error of Tajima's results based on T_{ave}, with respect to Longuet-Higgins's (1983) with $\nu = 0.1$, is 0.1%, while the average error of the results based on T_{peak} is 2%. In the nearshore region, $x > -150$ m, the discrepancies between Tajima's model and the probabilistic wave-by-wave approach become large, as shown in the middle plot of Figure 3-1. The wave height predicted by Tajima is as large as 3 times the value obtained by applying Longuet-Higgins's description. In the plot, only the ratio with respect to $\nu = 0.1$ is shown; the ratio with respect to $\nu = 0.6$ yields similar values in the nearshore region, where the wave-by-wave approach results are insensitive to the value of ν. Due to this overprediction of the wave height, Tajima's model yields a larger undertow in the nearshore region, as shown in Figure 3-5.
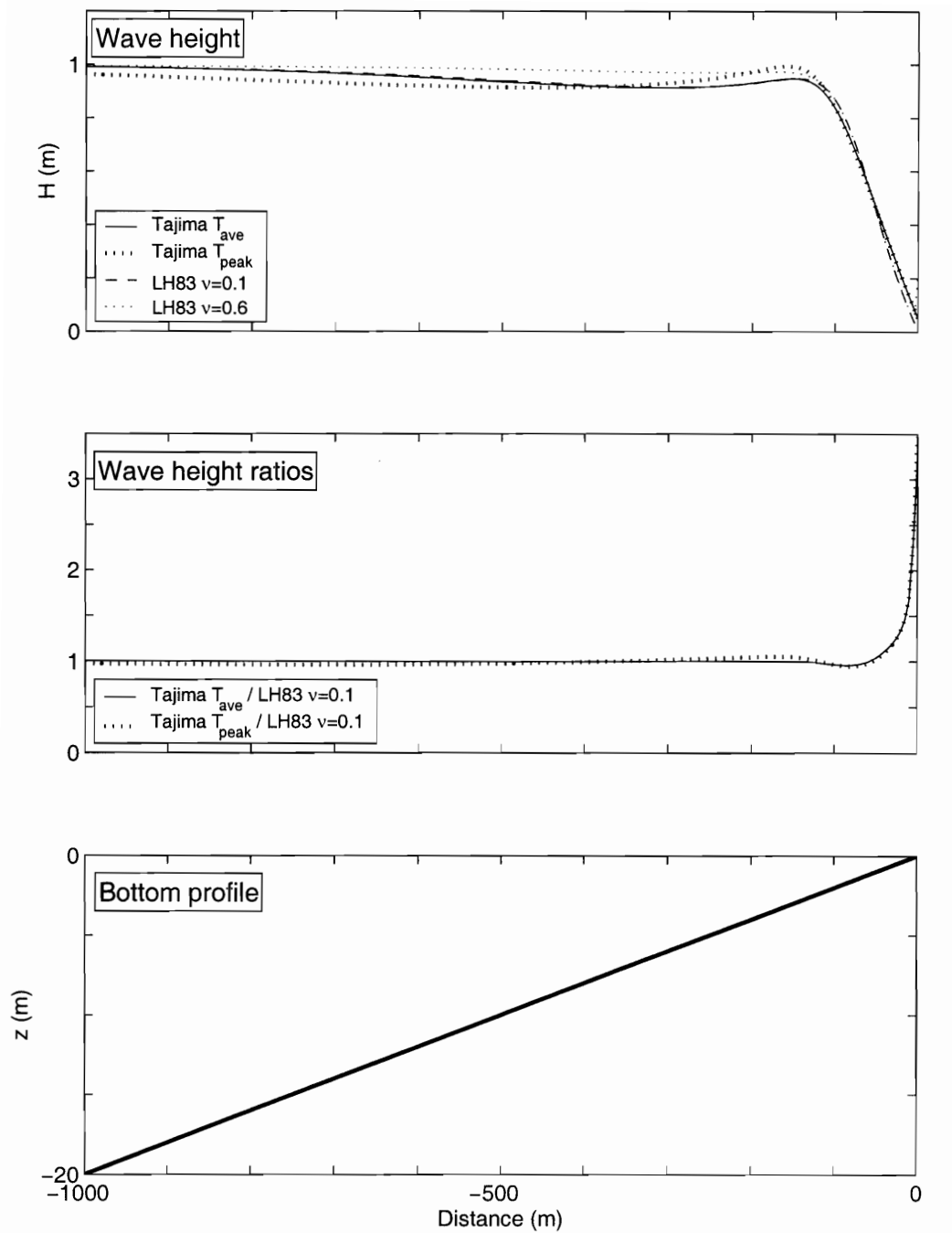
Figure 3-1: Comparison of wave height predictions in the plane beach case. Upper plot: Tajima's spectral model for H_{rms} and T_{ave} (solid line), Tajima's spectral model for H_{rms} and T_{peak} (thick dotted line), and Longuet-Higgins's (1983) distribution, for $\nu = 0.1$ (dashed line) and $\nu = 0.6$ (thin dotted line). Middle plot: Ratio between wave heights from Tajima's spectral model and from Longuet-Higgins's (1983) distribution for $\nu = 0.1$.
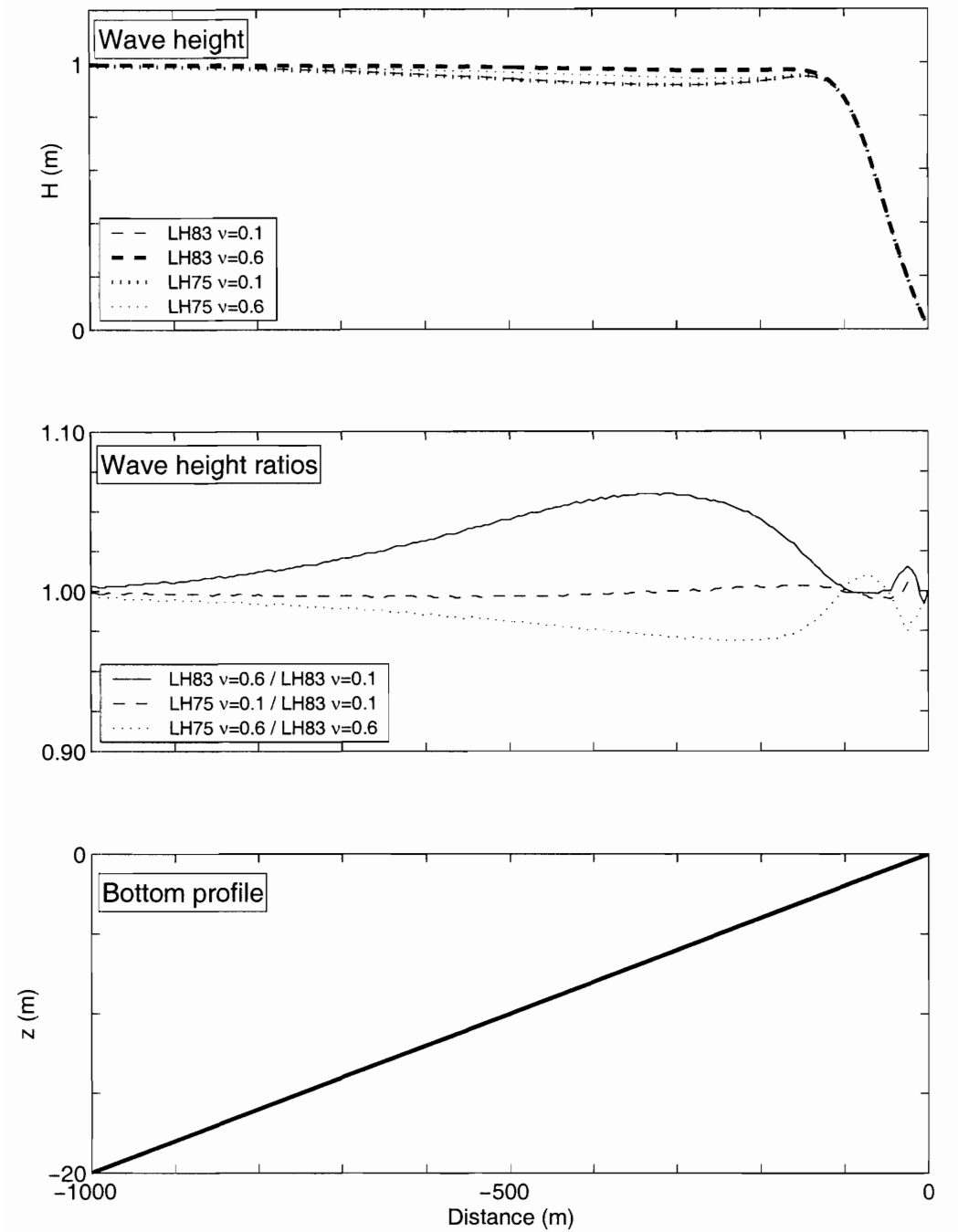
Figure 3-2: Comparison of wave height predictions in the plane beach case. Upper plot: Longuet-Higgins's 1983 distribution, for $\nu = 0.1$ (thin dashed line) and $\nu = 0.6$ (thick dashed line) and Longuet-Higgin's 1975 distribution, for $\nu = 0.1$ (thick dotted line) and $\nu = 0.6$ (thin dotted line). Middle plot: Ratios between the previous magnitudes.

Figure 3-2 shows a comparison between the predicted wave heights obtained by the probabilistic wave-by-wave approach using Longuet-Higgins's 1975 and 1983 distributions. For ease of comparison, ratios between magnitudes have been represented in the middle plot. For $\nu = 0.1$, both distributions yield almost the same results, with an average difference of 0.08%. For $\nu = 0.6$, the average difference is 0.8%, still small, and it remains small in the nearshore region. Furthermore, the average difference between the results for $\nu = 0.1$ and $\nu = 0.6$ for the same distribution (1983) is 1.5%, bigger than the difference between different distributions for a given value of ν. Therefore we conclude that the wave height predictions afforded by the two Longuet-Higgins's distributions are similar. Note that this statement is particularly accurate in the nearshore region, where the results are notably insensitive to the distribution choice and to the value of ν.

In Figure 3-3, we compare the radiation and surface roller stress gradients predicted by Tajima's spectral model, based on T_{ave} and on T_{peak}, with the wave-by-wave approach predictions using Longuet-Higgins's (1983). Both realizations of Tajima's spectral model yield results displaced seaward with respect to the probabilistic description, but this disagreement is more pronounced for the T_{peak} choice. Since the peak period is larger than the average period, it leads to a larger wavelength. Consequently, the peak period wave feels the bottom earlier than the average period wave, and the difference with respect to the probabilistic results is more pronounced. Note that, surprisingly, Tajima's predictions are closer to the probabilistic approach results for wider spectra ($\nu = 0.6$). Tajima's model corresponds to $\nu = 0$, and therefore we expected its results to be closer to the probabilistic results for narrower spectra ($\nu = 0.1$).

Stress gradient predictions using the 1975 and 1983 distributions are compared in Figure 3-4. According to the integrability considerations discussed in Section 3.2 and summarized in Table 3.2, radiation and surface roller stresses can only be calculated without period weighting for the 1983 distribution, while the 1975 distribution allows period weighting. All the probabilistic descriptions (1983 distribution without period weighting; 1975 distribution without and with period weighting) yield coincidental

60
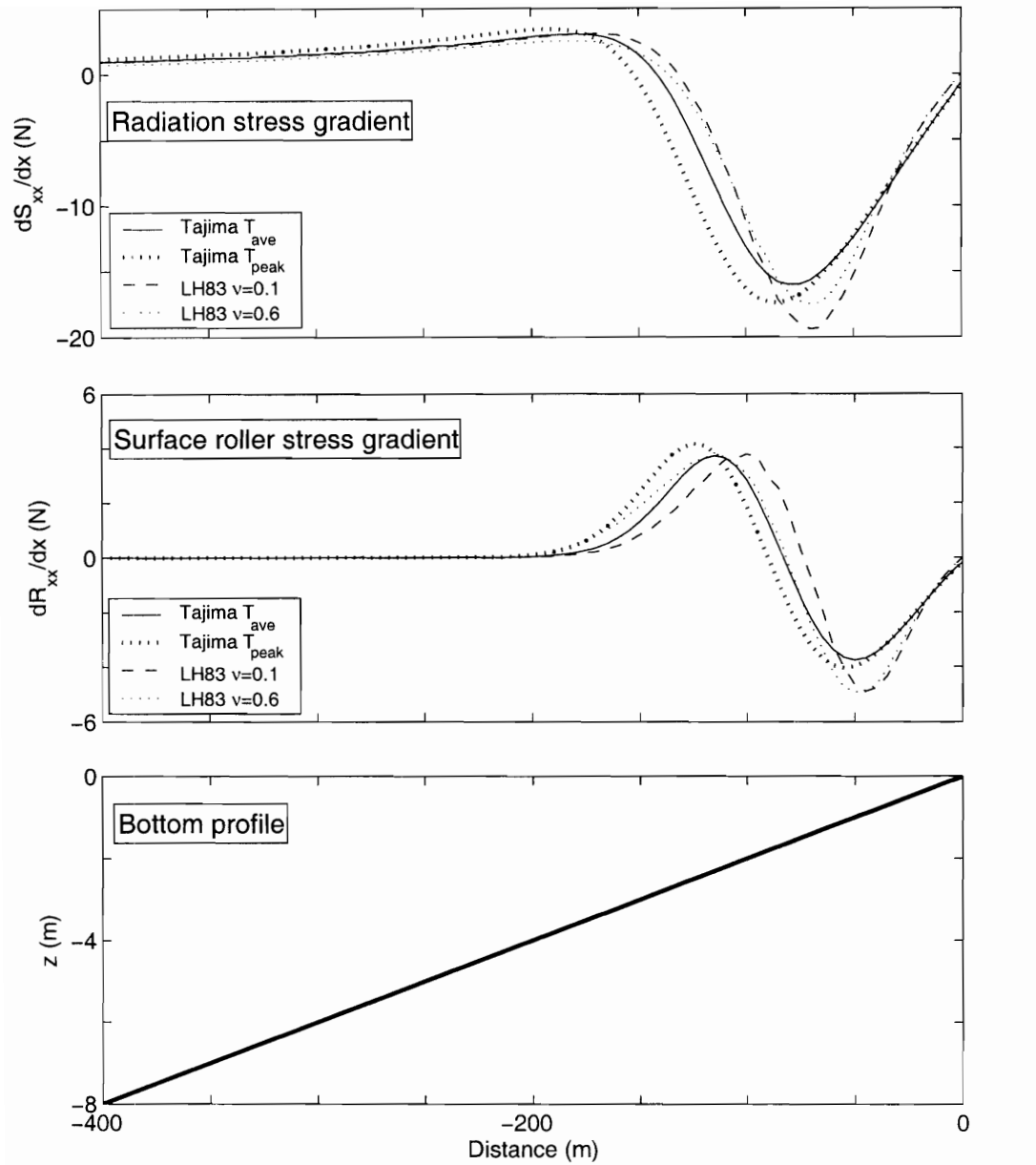
Figure 3-3: Comparison of radiation stress gradients and surface roller stress gradients in the plane beach case. Tajima's spectral model for H_{rms} and T_{ave} (solid line), Tajima's spectral model for H_{rms} and T_{peak} (thick dotted line), and Longuet-Higgins's (1983) distribution, for $\nu = 0.1$ (dashed line) and $\nu = 0.6$ (thin dotted line). Different wave period durations are not accounted for when averaging.

61
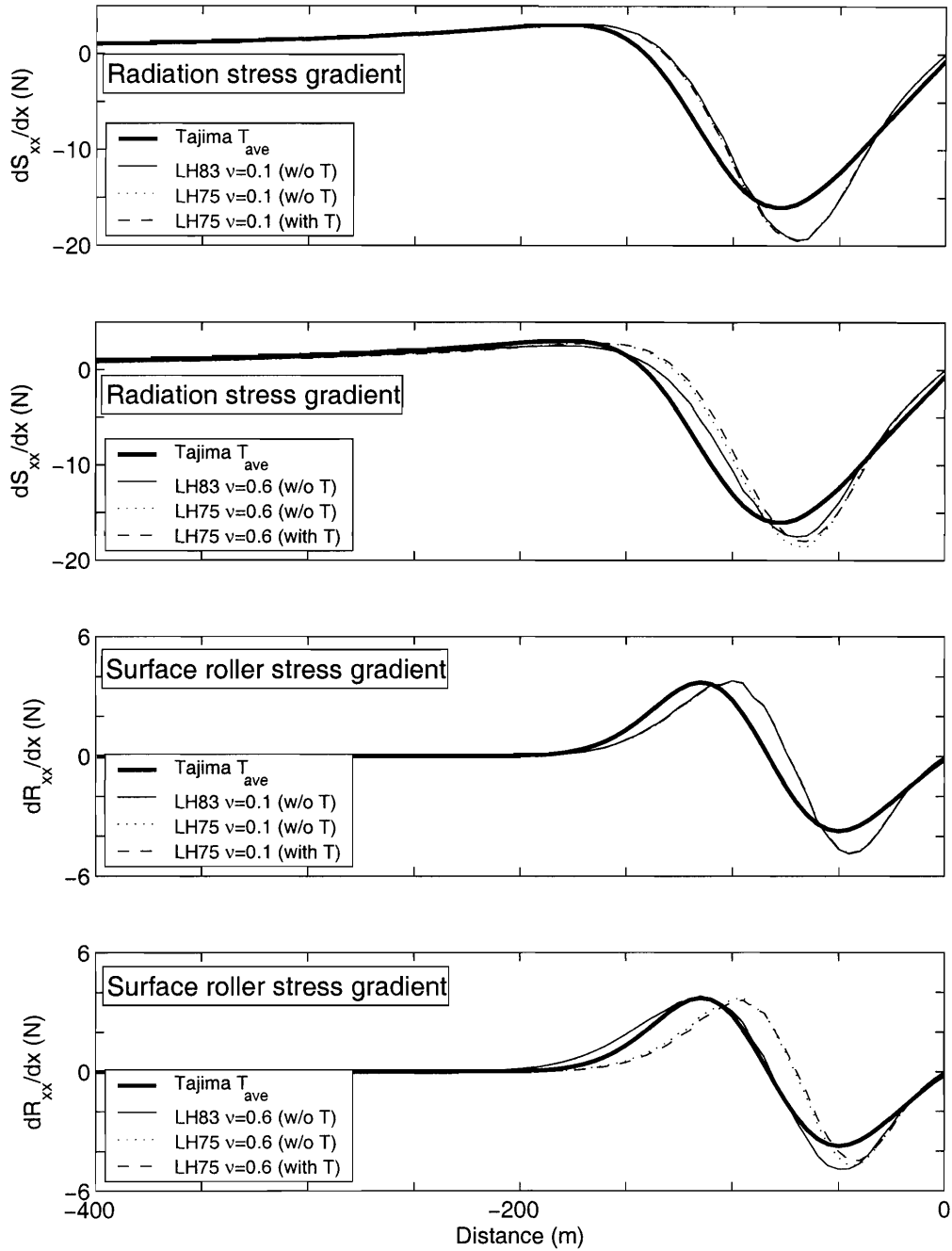
Figure 3-4: Comparison of radiation stress gradients and surface roller stress gradients in the plane beach case. The models compared are: Tajima's spectral model for H_{rms} and T_{ave}, Longuet-Higgins's (1983) distribution, for $\nu = 0.1$ and $\nu = 0.6$, and Longuet-Higgins's (1975) distribution, for $\nu = 0.1$ and $\nu = 0.6$. Results accounting for and not accounting for wave period durations are shown for Longuet-Higgins's (1975) distribution.

results for narrow spectra ($\nu = 0.1$). For wider spectra ($\nu = 0.6$), the results from the 1983 distribution are closer to Tajima's predictions than the results from the 1975 distribution. Note that period averaging does not have significant influence on the 1975 distribution results for any value of $\nu = 0.1$.

For the same plane beach case, Figure 3-5 compares wave set-up and undertow results afforded by Tajima's spectral model and by Longuet-Higgins's 1983 probabilistic description. Longuet-Higgins's 1975 distribution results, not shown in the figure, are similar to the 1983 distribution results. The wave set-up, $\bar{\eta}$, is given by

$$\rho g(h + \bar{\eta})\frac{\partial \bar{\eta}}{\partial x} = -\frac{\partial}{\partial x}(S_{xx} + R_{xx}) - \tau_{cbx} \tag{3.20}$$

where the bottom current shear stress, τ_{cbx}, has been neglected because of its generally negligible effect compared to the stress gradients, as shown by Tajima (2004). The undertow, U_0, is obtained from mass conservation as

$$U_0 = -\frac{q_{wx} + q_{srx}}{h + \bar{\eta}} \tag{3.21}$$

where q_{wx} and q_{srx} are the volume fluxes due to waves and surface roller, respectively, as defined in (4.1) and (4.4). Figure 3-5 shows very good agreement between different predictions of the wave set-up, while we observe some discrepancies between undertow predictions. Tajima's spectral model predicts a variation of the undertow of similar shape as the probabilistic models. However, Tajima underpredicts the maximum magnitude of the undertow after the breakpoint, and it overpredicts the undertow values near the shore. This latter overprediction is related to the larger wave height computed by Tajima's model in the nearshore region, as shown in Figure 3-1, and may have a significant influence in sediment transport calculations. Again, the agreement with the probabilistic descriptions is better when Tajima's model is based on the average period, T_{ave}, than on the peak period, T_{peak}; particularly around the breakpoint.

Figures 3-6 and 3-7 show the same comparison on a barred beach topography, which corresponds to the experiments by Wang et al. (2002). Only the probabilistic

63
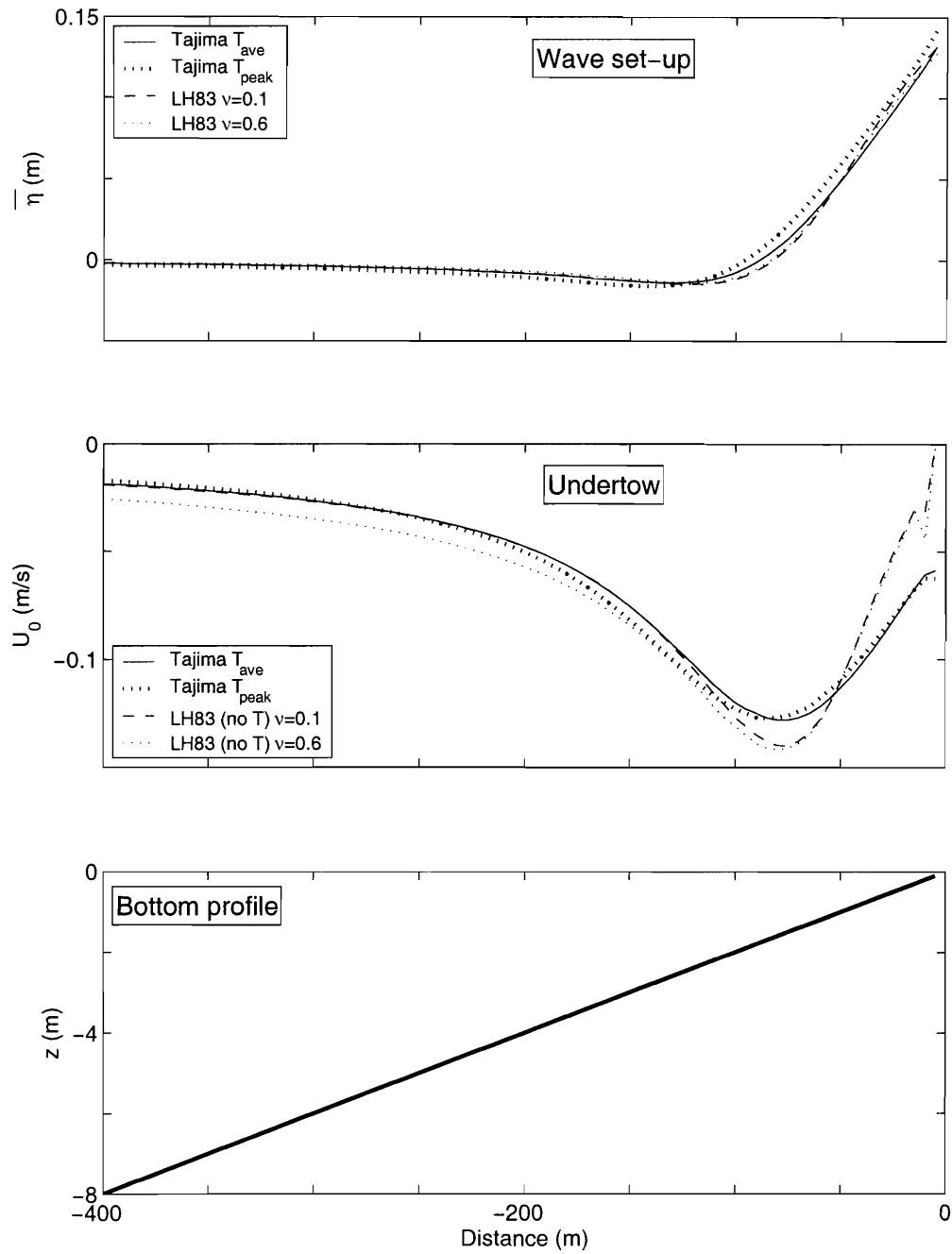
Figure 3-5: Comparison of wave set-up and return current velocities in the plane beach case. Tajima's spectral model for H_{rms} and T_{ave} (solid line), Tajima's spectral model for H_{rms} and T_{peak} (thick dotted line), and Longuet-Higgins's (1983) distribution, for $\nu = 0.1$ (dashed line) and $\nu = 0.6$ (thin dotted line). Upper plot: Wave set-up. Middle plot: Return current velocity.
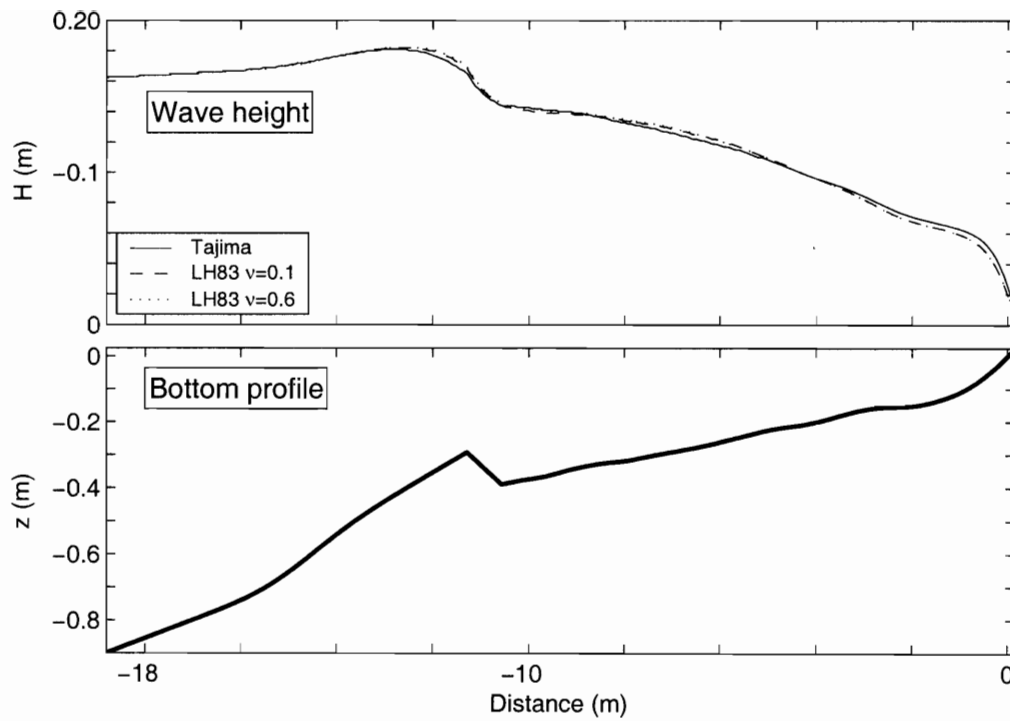
Figure 3-6: Comparison of wave height predictions in the barred beach case. Tajima's spectral model (solid line) and Longuet-Higgins's (1983) distribution, for $\nu = 0.1$ (dashed line) and $\nu = 0.6$ (dotted line).
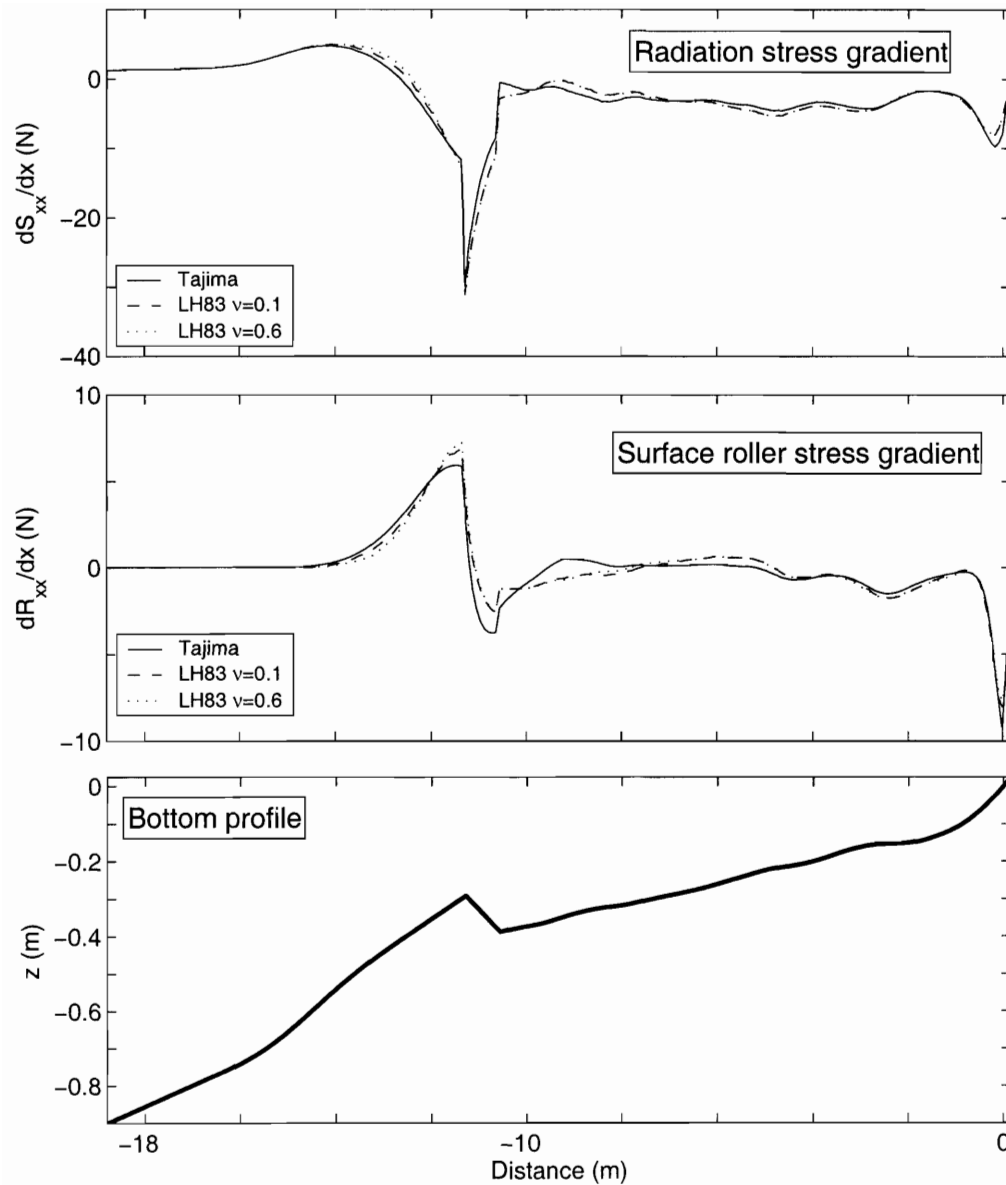
Figure 3-7: Comparison of radiation stress gradients and surface roller stress gradients in the barred beach case. Tajima's spectral model (solid line) and Longuet-Higgins's (1983) distribution, for $\nu = 0.1$ (dashed line) and $\nu = 0.6$ (dotted line). Different wave period durations are not accounted for when averaging.

results corresponding to Longuet-Higgins's (1983) distribution are presented here; the 1975 results are essentially similar. For this topography, the bar acts as a strong conditioning for model results, and good agreement is found between Tajima's spectral model and the probabilistic wave-by-wave approach, better than in the plane beach case.

3.4 Conclusion

We have developed a probabilistic wave-by-wave approach that yields a more detailed prediction of nearshore hydrodynamics than Tajima's (2004) simple spectral model. To characterize the incident waves, we have tested Longuet-Higgins's 1975 and 1983 probability distributions, which have been shown to give a good description of real sea waves, in agreement with JONSWAP spectrum. Since only the 1983 distribution accounts for the asymmetry of wave periods, which is observed in broad spectra, it is preferred to the 1975 distribution. However, in our probabilistic wave-by-wave formulation, it appears conceptually appropriate to introduce a T factor when averaging individual wave component results, which is only possible by using the 1975 distribution, due to integrability considerations discussed in Section 3.2. Nevertheless, the numerical experiments for plane and barred beaches show that this extra T factor has negligible influence on the results yielded by the 1975 distribution. Therefore, it is accurate enough to disregard the effect of the wave period averaging and to use Longuet-Higgins's 1983 distribution without including the T factor.

The probabilistic wave-by-wave approach was compared to Tajima's (2004) spectral model. Some discrepancies between Tajima's spectral model and the more detailed probabilistic description have been found. The agreement is improved when Tajima's very narrow spectral model is characterized by H_{rms} and $T_{ave} = 2\pi m_0/m_1$, instead of H_{rms} and T_{peak} as originally suggested by Tajima. However, for either choice of the representative period, predictions of wave heights and undertow near the shore are significantly different from those afforded by the wave-by-wave approach.

Chapter 4

Unsteady one-dimensional hydrodynamic model

Tajima's (2004) hydrodynamic model, whose main features were summarized in Chapter 2, assumes steady conditions. Real sea conditions, however, are usually unsteady and vary over a longer scale than the wave period. Changes in this longer scale may significantly affect sediment transport, and therefore they must be taken into account.

In this chapter, we extend Tajima's hydrodynamic model to unsteady conditions. First, we present a generalization of the governing equations to the unsteady case. Then, we detail the numerical implementation of these generalized equations. Finally, we apply the unsteady hydrodynamic model to test cases and show the relevance of the unsteady generalization to sediment transport calculations.

4.1 Derivation of the governing equations

Volume fluxes and momentum forcings

In this section, we present the governing equations for the unsteady case. The wave, surface roller and current models stay the same as Tajima's. Their formulations were summarized in Chapter 2, Sections 2.1.1, 2.2.1 and 2.3, respectively.

Volume fluxes and momentum forcings due to waves and surface rollers play an im-

portant role in the governing equations. According to Tajima (2004), the components of the wave volume flux above the trough level are

$$(q_{wx}, q_{wy}) = \overline{\int_{h-H/2}^{h+\eta} (\tilde{u}, \tilde{v}) dz} = \frac{E}{\rho C} (\cos\theta, \sin\theta) \tag{4.1}$$

where $(\tilde{u}, \tilde{v})$ are the wave orbital velocity components in x- and y-directions, respectively, the overline represents time-average over a wave period, E is the wave energy density, and θ is the angle of wave incidence.

Wave radiation stresses, S_{xx} and S_{xy}, are given by (e.g., Mei, 1989, p. 466)

$$S_{xx} = \overline{\int_0^{h+\eta} (p + \rho\tilde{u}^2) dz} - \frac{\rho g}{2} h^2 = E\left[\frac{C_g}{C}\left(1 + \cos^2\theta\right) - \frac{1}{2}\right] \tag{4.2}$$

$$S_{xy} = \overline{\int_0^{h+\eta} \rho\tilde{u}\tilde{v} dz} = \frac{E}{2}\frac{C_g}{C}\sin(2\theta) \tag{4.3}$$

According to (2.25), the volume fluxes in x- and y-directions due to the surface roller are

$$(q_{srx}, q_{sry}) = \frac{S_{sr}}{T}(\cos\theta, \sin\theta) = \frac{2E_{sr}}{\rho C}(\cos\theta, \sin\theta) \tag{4.4}$$

where S_{sr} and E_{sr} are the surface area and energy of the roller, respectively, as defined in Section 2.2.1.

Averaged momentum fluxes due to the surface roller, R_{xx} and R_{xy}, are expressed as (Tajima, 2004)

$$R_{xx} = \frac{\rho S_{sr} C^2 \cos^2\theta}{L} = 2E_{sr}\cos^2\theta \tag{4.5}$$

$$R_{xy} = \frac{\rho S_{sr} C^2 \cos\theta\sin\theta}{L} = E_{sr}\sin(2\theta) \tag{4.6}$$

Relationships between stresses and current velocities

The main variables that define the model are set-up, $\bar{\eta}$, total flux due to currents, (q_{cx}, q_{cy}), surface velocities, (U_s, V_s), bottom shear stresses, (τ_{cbx}, τ_{cby}), and trough shear stresses, (τ_{csx}, τ_{csy}). The first five are the independent variables in our formulation. The bottom and trough shear stresses are related to the independent variables

through our nearshore current model. According to (2.46),

$$U_s = C_{sb}\tau_{cbx} + C_{ss}\tau_{csx} \tag{4.7}$$

where

$$\begin{aligned}
C_{sb} &= \frac{1}{\rho\kappa u_{*m}}\ln\frac{\delta}{z_0} + \frac{1}{\rho\kappa u_{*c}}ln\frac{z_m}{\delta} \\
&\quad -\frac{(z_m-\delta)}{\rho\kappa u_{*c}h_{tr}} + \frac{2}{\rho\kappa u_{*s}}\frac{\left(\sqrt{h_{tr}}-\sqrt{z_m}\right)^2}{\sqrt{z_m h_{tr}}} \tag{4.8} \\
C_{ss} &= \frac{z_m-\delta}{\rho\kappa u_{*c}h_{tr}} + \frac{2}{\rho\kappa u_{*s}}\frac{\sqrt{h_{tr}}-\sqrt{z_m}}{\sqrt{h_{tr}}} \tag{4.9}
\end{aligned}$$

Integrating the velocity profile, (2.46), from $z = z_0$ to $z = h + \bar{\eta}$, we get

$$q_{cx} = C_{bb}\tau_{cbx} + C_{bs}\tau_{csx} \tag{4.10}$$

where

$$\begin{aligned}
C_{bb} &= \frac{1}{\rho\kappa u_{*m}}\left(-\delta + z_0 + h_{tr}\ln\frac{\delta}{z_0}\right) + \frac{1}{\rho\kappa u_{*c}}\left(-z_m + \delta + h_{tr}\ln\frac{z_m}{\delta}\right) \\
&\quad -\frac{z_m-\delta}{\rho\kappa u_{*c}}\left(1 - \frac{z_m+\delta}{2h_{tr}}\right) \\
&\quad +\frac{2}{\rho\kappa u_{*c}}\left(\frac{h_{tr}^{3/2}}{\sqrt{z_m}} - \frac{8}{3}h_{tr} + 2\sqrt{z_m h_{tr}} - \frac{z_m^{3/2}}{3\sqrt{h_{tr}}}\right) + C_{sb}\hat{a} \tag{4.11} \\
C_{bs} &= \frac{1}{\rho\kappa u_{*c}}(z_m-\delta)\left(1 - \frac{1}{2}\frac{z_m+\delta}{h_{tr}}\right) \\
&\quad +\frac{2}{\rho\kappa u_{*s}}\frac{1}{h_{tr}}\left(\frac{2}{3}h_{tr}^{3/2} - h_{tr}\sqrt{z_m} + \frac{z_m^{3/2}}{3}\right) + C_{ss}\hat{a} \tag{4.12}
\end{aligned}$$

The system of equations (4.7) and (4.10) yields

$$\tau_{cbx} = \frac{C_{ss}q_{cx} - C_{bs}U_s}{C_{bb}C_{ss} - C_{sb}C_{bs}} \tag{4.13}$$

$$\tau_{csx} = \frac{C_{sb}q_{cx} - C_{bb}U_s}{C_{bs}C_{sb} - C_{ss}C_{bb}} \tag{4.14}$$

Analogously,

$$\tau_{cby} = \frac{C_{ss}q_{cy} - C_{bs}V_s}{C_{bb}C_{ss} - C_{sb}C_{bs}} \tag{4.15}$$

$$\tau_{csy} = \frac{C_{sb}q_{cy} - C_{bb}V_s}{C_{bs}C_{sb} - C_{ss}C_{bb}} \tag{4.16}$$

71

Governing equations

Equations (4.13) through (4.16) allow us to compute the shear stresses from the independent variables. The five independent variables, $\bar{\eta}$, q_{cx}, q_{cy}, U_s, and V_s, are obtained from the governing equations: Depth-integrated mass conservation equation, depth-integrated momentum conservation equations above the trough level (in x- and y- directions), and depth-integrated momentum conservation equations over the whole depth (in x- and y-directions). The derivation of these equations for the unsteady case and the notation are detailed in Appendix B. Here, we summarize the resulting equations under the long, straight beach assumption, i.e., $\partial/\partial y = 0$. Integration of the mass conservation equation along the whole depth, (B.59), yields

$$\underline{\underline{\frac{\partial \bar{\eta}}{\partial t_0}}} + \frac{\partial}{\partial x}\left(q_{cx} + q_{wx} + q_{srx}\right) = 0 \tag{4.17}$$

where t_0 is the slow time variation, and q_{wx} and q_{srx} are the fluxes due to waves and roller, respectively (see Appendix B for details). In our time-advancing numerical scheme, we will use this equation to compute $\bar{\eta}$, since this is the only independent variable involved in a time-derivative in this equation (double-underlined term).

The momentum equations integrated above the trough level yield expressions for the trough shear stresses. In the cross-shore (x) direction,

$$\tau_{csx} = F_{shpx} + F_{swx} + F_{srx} + F_{scx} \tag{4.18}$$

where F_{shpx}, F_{swx}, F_{srx}, and F_{scx} are forces due to hydrostatic pressure, waves, roller, and current and current-associated interactions, respectively. Neglecting atmospheric pressure and wind shear stress contributions, (B.33) yields

$$F_{shpx} = -\rho g \hat{a} \frac{\partial \bar{\eta}}{\partial x} \tag{4.19}$$

$$F_{swx} = -\frac{\partial}{\partial x}\left(\frac{E}{2}\right) - \rho q_{wx}\frac{\partial \hat{u}_s}{\partial x} + \frac{\rho}{2}\left(\hat{a}\frac{\partial \hat{w}_s^2}{\partial x} + \hat{w}_s^2\frac{\partial \bar{\eta}}{\partial x}\right) - \frac{1}{2}\rho\hat{a}\frac{\partial \hat{u}_s}{\partial t_0} \tag{4.20}$$

$$F_{srx} = -\frac{\partial R_{xx}}{\partial x} - \rho\frac{\partial q_{srx}}{\partial t_0} \tag{4.21}$$

72

$$F_{scx} = -\rho \left((U_s \hat{a} + q_{wx} + q_{srx}) \frac{\partial U_s}{\partial x} + \frac{\hat{a} U_s}{2} \frac{\partial \hat{u}_s}{\partial x} \right) - \rho \frac{\partial \bar{\eta}}{\partial t_0} U_s - \rho \hat{a} \underline{\underline{\frac{\partial U_s}{\partial t_0}}} \quad (4.22)$$

Note that U_s (double-underlined term) and $\bar{\eta}$ are the independent variables involved in time-derivatives in equation (4.18). $\partial \bar{\eta}/\partial t_0$ can be expressed in terms of spatial derivatives by means of (4.17). Therefore, in our numerical scheme, we will use equation (4.18) to compute U_s.

Similarly, in the alongshore direction (y), we have

$$\tau_{csy} = F_{swy} + F_{sry} + F_{scy} + F_{svy} \quad (4.23)$$

where

$$F_{swy} = -\rho q_{wx} \frac{\partial \hat{v}_s}{\partial x} - \frac{1}{2} \rho \hat{a} \frac{\partial \hat{v}_s}{\partial t_0} \quad (4.24)$$

$$F_{sry} = -\frac{\partial R_{xy}}{\partial x} - \rho \frac{\partial q_{sry}}{\partial t_0} \quad (4.25)$$

$$F_{scy} = -\rho \left((U_s \hat{a} + q_{wx} + q_{srx}) \frac{\partial V_s}{\partial x} + \frac{\hat{a} U_s}{2} \frac{\partial \hat{v}_s}{\partial x} \right) - \rho \frac{\partial \bar{\eta}}{\partial t_0} V_s - \rho \hat{a} \underline{\underline{\frac{\partial V_s}{\partial t_0}}} \quad (4.26)$$

$$F_{svy} = \hat{a} \frac{\partial \tau_{xy}}{\partial x} = \rho \hat{a} \left(\nu_{ts} \frac{\partial V_s}{\partial x} \right) \quad (4.27)$$

and F_{svy} is a turbulent viscous force, and ν_{ts} is the turbulent eddy viscosity at the trough level, defined in (2.38). Equation (4.23) will be used to compute V_s.

The integrated momentum equations over the entire depth yield expressions for the bottom shear stresses, as obtained in (B.49). In x-direction,

$$\tau_{cbx} = F_{bhpx} + F_{bwx} + F_{srx} + F_{bcx} \quad (4.28)$$

where, neglecting atmospheric pressure and wind shear stress contributions,

$$F_{bhpx} = -\rho g(h + \bar{\eta}) \frac{\partial \bar{\eta}}{\partial x} \quad (4.29)$$

$$F_{bwx} = -\frac{\partial S_{xx}}{\partial x} - \rho \frac{\partial q_{wx}}{\partial t_0} \quad (4.30)$$

$$F_{bcx} = -\rho \frac{\partial}{\partial x} \left((2q_{wx} + q_{srx}) U_s + \left(\hat{a} U_s^2 + q_{bx} U_0 \right) \right) - \rho \underline{\underline{\frac{\partial q_{cx}}{\partial t_0}}} \quad (4.31)$$

73

where $q_{bx} = q_{cx} - U_s \hat{a}$ is the volume flux under the trough level due to currents, and U_0 denotes the x-component of the vertically-averaged wave-induced current velocity under trough level. Equation (4.28) will be used to compute q_{cx}.

Similarly, in y-direction,

$$\tau_{cby} = F_{bwy} + F_{sry} + F_{bcy} + F_{bvy} \tag{4.32}$$

where

$$F_{bwy} = -\frac{\partial S_{xy}}{\partial x} - \rho \frac{\partial q_{wy}}{\partial t_0} \tag{4.33}$$

$$F_{bcy} = -\rho \frac{\partial}{\partial x} \left((q_{wx} + q_{srx}) V_s + q_{wy} U_s + \hat{a} U_s V_s + q_{bx} V_0 \right) - \rho \frac{\partial q_{cy}}{\partial t_0} \tag{4.34}$$

$$F_{bvy} = \int_{-h}^{\bar{\eta}} \frac{\partial \bar{\tau}_{xy}}{\partial x} dz = \rho \hat{a} \left(\nu_{ts} \frac{\partial V_s}{\partial x} \right) + \rho (h - z_{tr}) \frac{\partial}{\partial x} \left(\nu_{t0} \frac{\partial V_0}{\partial x} \right) \tag{4.35}$$

where ν_{t0} is the averaged value of the turbulent eddy viscosity under the trough level, which can be calculated from (2.38). Equation (4.32) will be used to compute q_{cy}.

4.2 Numerical implementation

4.2.1 Model input

The input for the hydrodynamic model consists of the bathymetry and the characteristics of the incident wave. Like Tajima (2004), we require the bathymetry to be parallel to the shoreline, according to the assumption of a long straight beach. The incident wave characteristics are the wave height, period, and angle of incidence. We are interested in modeling a wave beat, in which the wave height varies slowly in time. We further assume a narrow-banded spectrum, characterized by a single period, and therefore treat the waves as monochromatic. The angle of incidence is represented by a single value.

The time scale over which the wave height changes, the beat period, is by definition significantly longer than the time scale of the wave motion, the wave period.

74

Wave beats often arise in real seas. A wave beat can be regarded as the result of the superposition of two simple harmonic waves of slightly different wave frequency. Consider two such waves,

$$\eta_1 = \frac{a}{2} \cos \varphi_1 \tag{4.36}$$

$$\eta_2 = \frac{a}{2} \cos \varphi_2 \tag{4.37}$$

where

$$\varphi_1 = (k_x + \delta k_x) x + (k_y + \delta k_y) y - (\omega + \delta \omega) t \tag{4.38}$$

$$\varphi_2 = (k_x - \delta k_x) x + (k_y - \delta k_y) y - (\omega - \delta \omega) t \tag{4.39}$$

such that $\delta \omega \ll \omega$. The superposition of these two waves yields

$$\eta = \eta_1 + \eta_2 = \hat{a} \cos \varphi \tag{4.40}$$

with

$$\hat{a} = a \cos (\delta k_x \, x + \delta k_y \, y - \delta \omega \, t) \tag{4.41}$$

$$\varphi = k_x x + k_y y - \omega t \tag{4.42}$$

Here, the superposition of the two monochromatic waves results in a wave beat whose amplitude varies from 0 to a, as represented in Figure 4-1(a).

Suppose now that the two incident waves, η_1 and η_2, have different amplitudes:

$$\eta_1 = a_1 \cos \varphi_1 \tag{4.43}$$

$$\eta_2 = a_2 \cos \varphi_2 \tag{4.44}$$

with φ_1 and φ_2 defined by (4.38) and (4.39), respectively. The resulting wave is

$$\eta = \eta_1 + \eta_2 = \hat{a} \cos (k_x x + k_y y - \omega t - \psi) \tag{4.45}$$
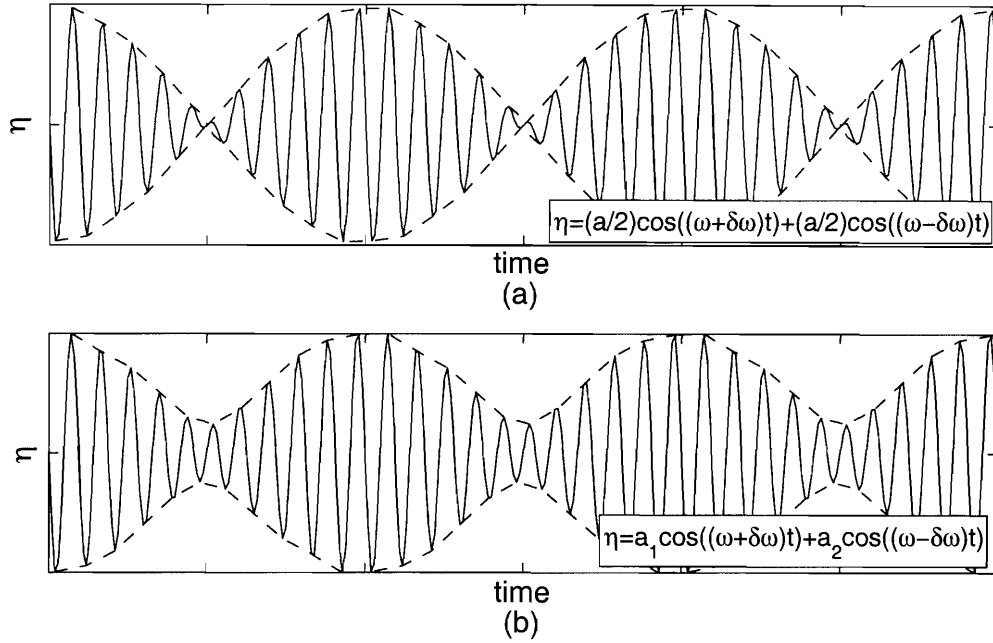
Figure 4-1: Time evolution of water elevation in a wave beat. (a) Superposition of two waves of identical amplitude. The dashed line represents the wave amplitude of the resulting beat. Note that the minimum beat amplitude is 0. (b) Superposition of two waves of different amplitude. The minimum amplitude of the resulting wave beat is greater than 0.

where

$$\hat{a} = \sqrt{a_1^2 + a_2^2 + 2a_1 a_2 \cos\left[2\left(\delta k_x x + \delta k_y y - \delta\omega\, t\right)\right]} \qquad (4.46)$$

$$\psi = \arccos\left\{\frac{(a_1 + a_2)\cos\left(\delta k_x\, x + \delta k_y\, y - \delta\omega\, t\right)}{\hat{a}}\right\} \qquad (4.47)$$

In this case, the beat amplitude is always strictly bigger than 0, as represented in Figure 4-1(b).

We will model the incident wave height variation similarly to the latter case. We will assume a slow and small time-variation of the wave height around its mean value. In our examples, the variation will be modeled as sinusoidal, although the numerical code we have developed allows for any other kind of variation.

The incident wave is defined in the model as a series of individual monochromatic

76

waves, each one of slightly different wave height from the precedent one and all of them with the same wave period. Each wave component has a duration of a wave period, and the series of wave components define the beat period.

This definition of the incident wave introduces step changes in the wave height from one component to another, which are inadequate for numerical purposes. For this reason, the wave height input is smoothed into a second order polynomial variation. For every wave period, we interpolate a second order polynomial time-varying wave height, according to the following requirements: i) Continuity of the wave height, ii) Continuity of the first derivative, iii) Conservation of total wave energy in each wave period.

Figure 4-2 shows how the smoothed incident wave looks for the numerical experiments presented in Section 4.3. In this case, the wave beat consists of 12 wave periods. Observe that, in the example, the variation of the incident wave height is only $\pm 0.1 H_{ave}$; due to this fact, H_{ave} and H_{rms} have similar values.
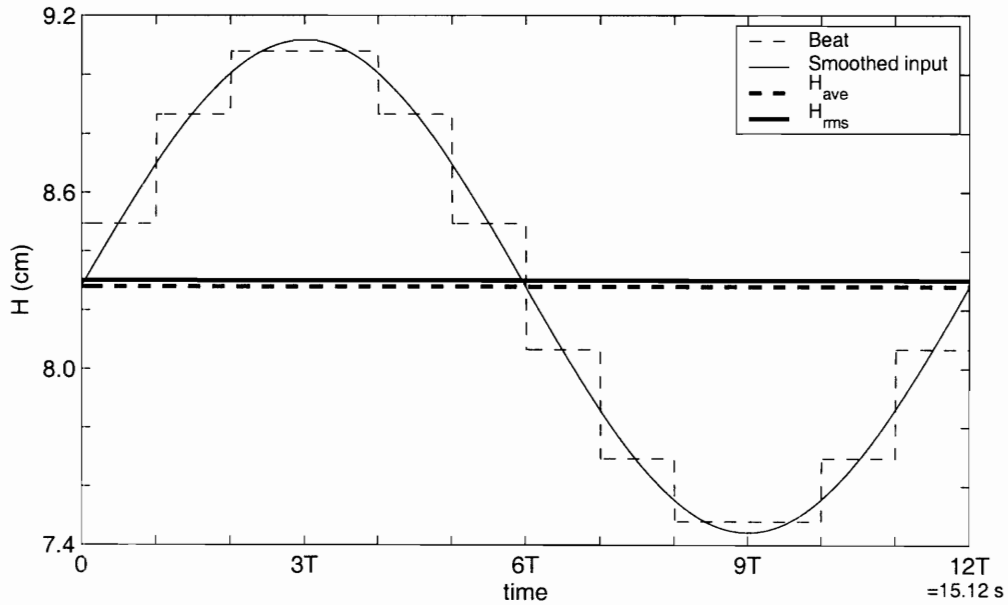

Figure 4-2: Input wave height at the offshore boundary: Incident beat and smoothed input for the numerical scheme. This input corresponds to the numerical experiments presented in Section 4.3. T stands for the wave period.

4.2.2 Model initialization

We adopt a solution scheme in which we advance in time. Therefore, we need to define initial values of the unknowns. These are obtained by running Tajima's (2004) monochromatic model for the mean wave height. Tajima's monochromatic model provides the initial values of wave set-up, current velocities and fluxes, and trough and bottom shear stresses.

Next, we need to determine the value of the wave height, H, (or equivalently the wave energy, E) and the surface roller energy, E_{sr}, at every location x and time t. The values of H, E, and E_{sr} are variable in time since they change in the slow time of the wave beat. Note that the wave and surface roller energy determine the values of the momentum fluxes, S_{xx}, S_{xy}, R_{xx} and R_{xy}. For the calculation of $H(x,t)$, $E(x,t)$, and $E_{sr}(x,t)$, we make the assumption that the values of the initial set-up provided by Tajima's monochromatic model for the root mean square wave height, H_{rms}, are representative of the set-up values for all time. Assuming these set-up values to hold, we propagate the input components of $H(x=0,t)$, for different t, using again Tajima's monochromatic wave model. We assume that each single wave component propagates at the local wave group velocity, $C_g(x)$. We note that real individual waves propagate at a speed $C > C_g$, and they move relatively to the wave envelope. Our model's individual wave components do not correspond to these real waves, but to a discretization of the wave envelope. The wave envelope and the wave energy both propagate at speed C_g. Since we are interested in the propagation of wave energy, we must impose that the model's individual wave components, of a given H, propagate at speed C_g. Therefore, $H(x=\hat{x}, t=\hat{t})$ is obtained by propagating the input component

$$H\left(x=0, t=\hat{t} - \int_{x=0}^{x=\hat{x}} \frac{1}{C_g(x)} dx\right) \tag{4.48}$$

from $x=0$ to $x=\hat{x}$, using Tajima's monochromatic model. Thus, we compute $H(x,t)$, $E(x,t)$, and $E_{sr}(x,t)$.

4.2.3 Numerical scheme

The time-advancing numerical scheme we use is a predictor-corrector method. We have implemented an Adams-Bashforth predictor scheme of 3rd order and an Adams-Moulton corrector scheme of 4th order (e.g., Ferziger and Perić, 2002).

The predictor-corrector method is defined in the following way. Suppose we want to solve the time-dependent implicit differential equation in ϕ

$$\frac{d\phi}{dt} = f(t, \phi) \tag{4.49}$$

We discretize the time domain in time intervals of equal length, Δt. Suppose we know $\{\phi^1, \phi^2, \dots, \phi^n\}$, i.e., the solution until time t_n, and we want to calculate ϕ^{n+1}, i.e., the solution for time $t_{n+1} = t_n + \Delta t$. We obtain a first approximation, ϕ_*^{n+1}, applying the 3rd order predictor scheme:

$$\phi_*^{n+1} = \phi^n + \frac{\Delta t}{12}\left[23f(t_n, \phi^n) - 16f(t_{n-1}, \phi^{n-1}) + 5f(t_{n-2}, \phi^{n-2})\right] \tag{4.50}$$

Then, we refine the approximation using the 4th order corrector scheme:

$$\phi^{n+1} = \phi^n + \frac{\Delta t}{24}\left[9f(t_{n+1}, \phi_*^{n+1}) + 19f(t_n, \phi^n) - 5f(t_{n-1}, \phi^{n-1}) + f(t_{n-2}, \phi^{n-2})\right] \tag{4.51}$$

In our hydrodynamic model, we apply this predictor-corrector method to a set of five coupled equations (4.17, 4.18, 4.23, 4.28, 4.32) with five unknowns ($\bar{\eta}$, q_{cx}, q_{cy}, U_s, V_s). Note that the numerical domain is therefore discretized both in space and time.

To summarize, the numerical procedure of the present model can be outlined as follows:

1. With the root mean square wave height, H_{rms}, compute initial cross-shore values of the independent variables and the shear stresses from Tajima's monochromatic model.

2. With the initial set-up value, and using Tajima's monochromatic model, com-

pute $H(x,t)$, $E(x,t)$, $E_{sr}(x,t)$. The volume fluxes and momentum fluxes in the governing equations remain thereafter determined for every x and t.

3. Apply the predictor algorithm (4.50) to the governing equations (4.17, 4.18, 4.23, 4.28, and 4.32), to obtain first estimates of the values of the independent variables ($\bar{\eta}$, q_{cx}, q_{cy}, U_s, and V_s) at the next time step, $t + \Delta t$.

4. Apply the corrector algorithm (4.51) to refine the previous estimates.

5. Impose the boundary conditions (see Section 4.2.4) to evaluate the unknowns at the boundaries.

6. Compute the trough and bottom shear stresses at time $t + \Delta t$ using equations (4.13) through (4.16).

7. Return to step 3 and repeat steps 3 to 6 until the solution for the whole time domain has been computed.

4.2.4   Boundary conditions

To complete the numerical formulation, we need to specify the boundary conditions. Since we are computing five independent variables, we require five boundary conditions at each of the two boundaries: Five at the offshore boundary and five at the onshore boundary.

Offshore boundary conditions

The set-up, $\bar{\eta}$, is determined by the radiation boundary condition. The radiation boundary condition expresses the fact that the offshore boundary is non-reflecting, and no waves advancing in the possitive x-direction other than the prescribed incident wave are allowed. Therefore, any wave moving in the negative x-direction is allowed to leave the domain without reflecting at the boundary. We apply a Sommerfeld-type radiation condition, whose derivation is detailed in Appendix C. The resulting

expression for $\bar{\eta}$ at the offshore boundary is

$$\bar{\eta}(t) = -\sqrt{\frac{h}{g}}U(t) \tag{4.52}$$

where

$$U(t) = \frac{q_{cx}(t) + q_{wx}(t) + q_{srx}(t)}{h} \tag{4.53}$$

and h is the still water depth. Note that, for the steady case, the net-flux in x-direction is zero and the right-hand side of (4.52) vanishes, yielding

$$\bar{\eta}(t) = 0 \tag{4.54}$$

The depth-averaged velocity in x-direction, U(t), can be written as

$$U(t) = \langle U \rangle + U'(t) \tag{4.55}$$

where $\langle U \rangle$ denotes the time-averaged value over the wave beat. In strict sense, the radiation condition only needs to be satisfied for $\langle U \rangle$, and we can allow for a zero-mean variation, $U'(t)$. However, we do not know how to determine the value of $U'(t)$. To avoid this problem, we impose the radiation condition for every time t, as stated by (4.52), which constitutes a more restrictive assumption.

Following Tajima (2004), the cross-shore flux is determined by assuming uniformity in x-direction, $\partial/\partial x = 0$, so that

$$\frac{\partial q_{cx}}{\partial x} = 0 \tag{4.56}$$

$$\frac{\partial U_s}{\partial x} = 0 \tag{4.57}$$

We also need a condition on the shore-parallel flux. This condition is of minor importance for the applications presented in this thesis, where we are mainly concerned with normal wave incidence. A possible boundary condition is obtained by assuming

that the total flux has the direction of the incident wave, and therefore

$$q_{cy} = q_{cx} \tan \theta_0 \qquad (4.58)$$

$$V_s = U_s \tan \theta_0 \qquad (4.59)$$

where θ_0 is the angle of offshore wave incidence. This boundary condition may need to be improved when computation of shore-parallel flux is relevant.

Onshore boundary conditions

In order to avoid computational instabilities in very shallow water, Tajima's (2004) numerical code stops the computation at a node, $i = i_{end}$, where the local trough depth, h_{tr}, becomes smaller than twice the local wave-current bottom boundary layer thickness, i.e., $h_{tr} \leq 2\delta$. We take this as a first approximation of our onshore boundary location. This first approximation is computed using Tajima's monochromatic model based on the *rms* wave height. However, when the wave height becomes variable due to the beat effect, it is likely that, at certain times, we obtain values of the set-up smaller than the initial one. This often causes a temporary negative total depth at $i = i_{end}$ and therefore numerical problems. If this happens, we reset $i_{end}^{new} = i_{end}^{old} - 1$ and restart the computation from the initial conditions. Eventually, we will get a value of i_{end} such that the total depth never becomes negative, and we are able to complete the calculations.

To calculate the set-up at the onshore boundary, we simply assume a linear extrapolation from the neighboring values:

$$\bar{\eta}_{i_{end}} = \bar{\eta}_{i_{end}-1} + \left(\frac{\partial \bar{\eta}}{\partial x} \right)_{i_{end}-1} \Delta x \qquad (4.60)$$

The current flux in the x-direction, q_{cx}, is computed imposing no flux beyond $i = i_{end} + 1$. This no-flux condition is represented in Figure 4-3 by a fictitious impermeable wall. The wave set-up is assumed to be constant from $i = i_{end}$ and $i = i_{end} + 1$. Imposing conservation of mass in this small volume beyond the onshore

boundary we get

$$q_{cx} = \frac{\partial A}{\partial t} - q_{wx} - q_{srx} = \frac{\partial \bar{\eta}}{\partial t}\Delta x - q_{wx} - q_{srx} \quad \text{at } i = i_{end} \qquad (4.61)$$

where A is the fluid volume per unit width between $i = i_{end}$ and $i = i_{end} + 1$, as shown in Figure 4-3.
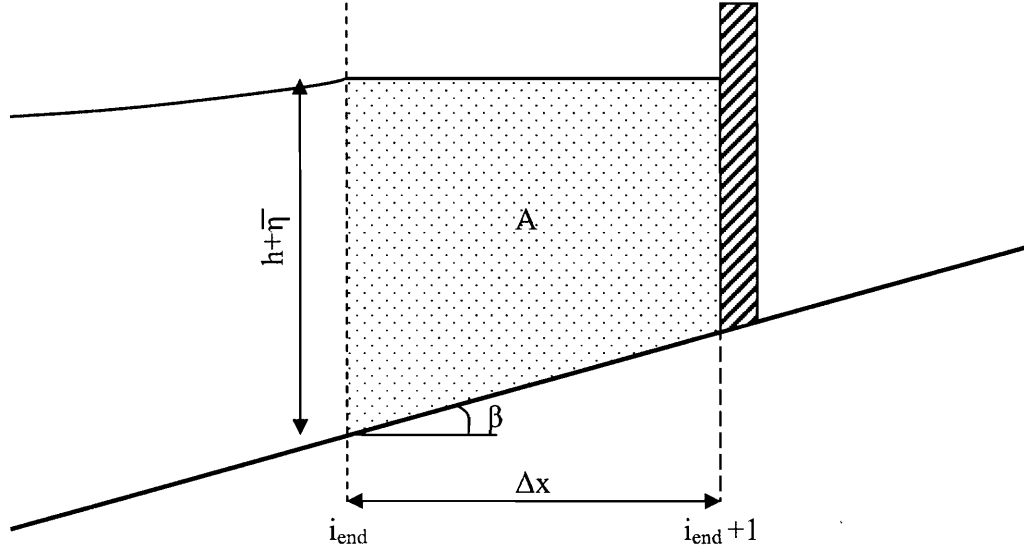
Figure 4-3: Onshore boundary condition for the current flux in x-direction. β is the bottom slope at $i = i_{end}$.

To impose this no-flux condition at $i = i_{end} + 1$ is numerically preferable to impose it at $i = i_{end}$, since the former provides a small buffer zone, A, which smooths out sudden changes of the variables that may happen at early stages of the computation.

The x-component of the current surface velocity near the onshore boundary is assumed to vary proportionally to the current flux, i.e.,

$$U_s|_{i_{end}} = U_s|_{i_{end}-1} \frac{\left(\frac{q_{cx}}{h+\bar{\eta}}\right)_{i_{end}}}{\left(\frac{q_{cx}}{h+\bar{\eta}}\right)_{i_{end}-1}} \qquad (4.62)$$

The y-components of the current flux and surface velocity are assumed to vary

proportionally to the total depth:

$$q_{cy}\big|_{i_{end}} = q_{cy}\big|_{i_{end}-1} \frac{(h+\bar{\eta})^2_{i_{end}}}{(h+\bar{\eta})^2_{i_{end}-1}} \qquad (4.63)$$

$$V_s\big|_{i_{end}} = V_s\big|_{i_{end}-1} \frac{(h+\bar{\eta})_{i_{end}}}{(h+\bar{\eta})_{i_{end}-1}} \qquad (4.64)$$

4.3 Application of the unsteady model

In this section, we illustrate the application of the unsteady model to the propagation of a wave beat. First, we compare the set-up and undertow resulting from a wave beat propagating over a barred beach with the values corresponding to the constant mean wave height. Next, we study a wave beat propagating on a plane beach and analyze the effect of the beach slope on the set-up. We show the hydrodynamic variation over the wave beat and identify coupling effects that affect sediment transport calculations.

4.3.1 Comparison between a wave beat and a constant wave

In this test case, we run our unsteady hydrodynamic model over a barred bathymetry corresponding to the experimental case presented by Wang et al. (2002). The wave period is $T_{wave} = 3$ s, the angle of incidence is $\theta_0 = 10^0$ and the wave height varies sinusoidally around a mean value of $H_{ave} = 0.162$ m. The beat variation of the wave height is of $\pm 0.1 H_{ave}$ over a wave beat $T_{beat} = 12 T_{wave} = 36$ s. We run a total of 10 wave beats. After a time of 2 beats, the results have converged, in the sense that they become perfectly periodic, following the wave beats, as shown in Figure 4-4, at location $x = -0.8$ m. This corresponds to the usual behavior of our unsteady model: After some initial oscillations, due to the approximate nature of the initial estimate provided by Tajima's monochromatic model, convergence, in the sense of beat periodicity, is achieved after a small number of beats.

Figure 4-5 shows a comparison between the results of the unsteady model, averaged in time over the last computed beat (i.e., average from $t = 324$ s to $t = 360$ s), and Tajima's monochromatic model results for the root mean square wave height,
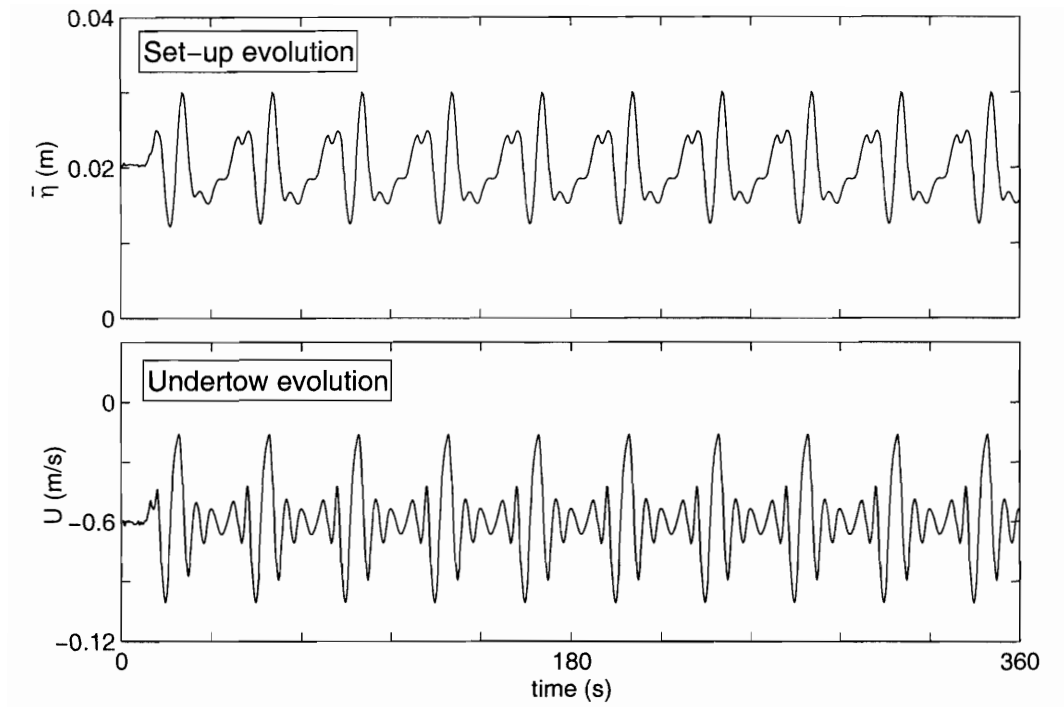
Figure 4-4: Evolution of the mean wave set-up ($\bar{\eta}$) and undertow (U) at $x = -0.8$ m. Periodicity is achieved quickly.

H_{rms}. The agreement between the two is very good, showing that the time-averaged results of the unsteady approach are consistent with Tajima's mean value predictions. However, the unsteady model is expected to capture hydrodynamic effects associated with the wave height variation, relevant to sediment transport, that are ignored by Tajima. This will be examined in the following section.

4.3.2 Wave beat propagating on a plane beach

Here we study a wave beat propagating on a plane beach. The wave beat has a sinusoidally varying wave height. It starts propagating from a deep water depth of $h_0 = 0.35$ m, where the average wave height value is $H_{ave} = 0.0828$ m and its variation is $\pm 0.1 H_{ave}$. Note that, due to the small wave height variation, H_{ave} and H_{rms} have virtually the same value. The wave period is constant, $T_{wave} = 1.26$ s. The beat period consists of 12 waves, $T_{beat} = 12 T_{wave} = 15.12$ s. We consider different values

85

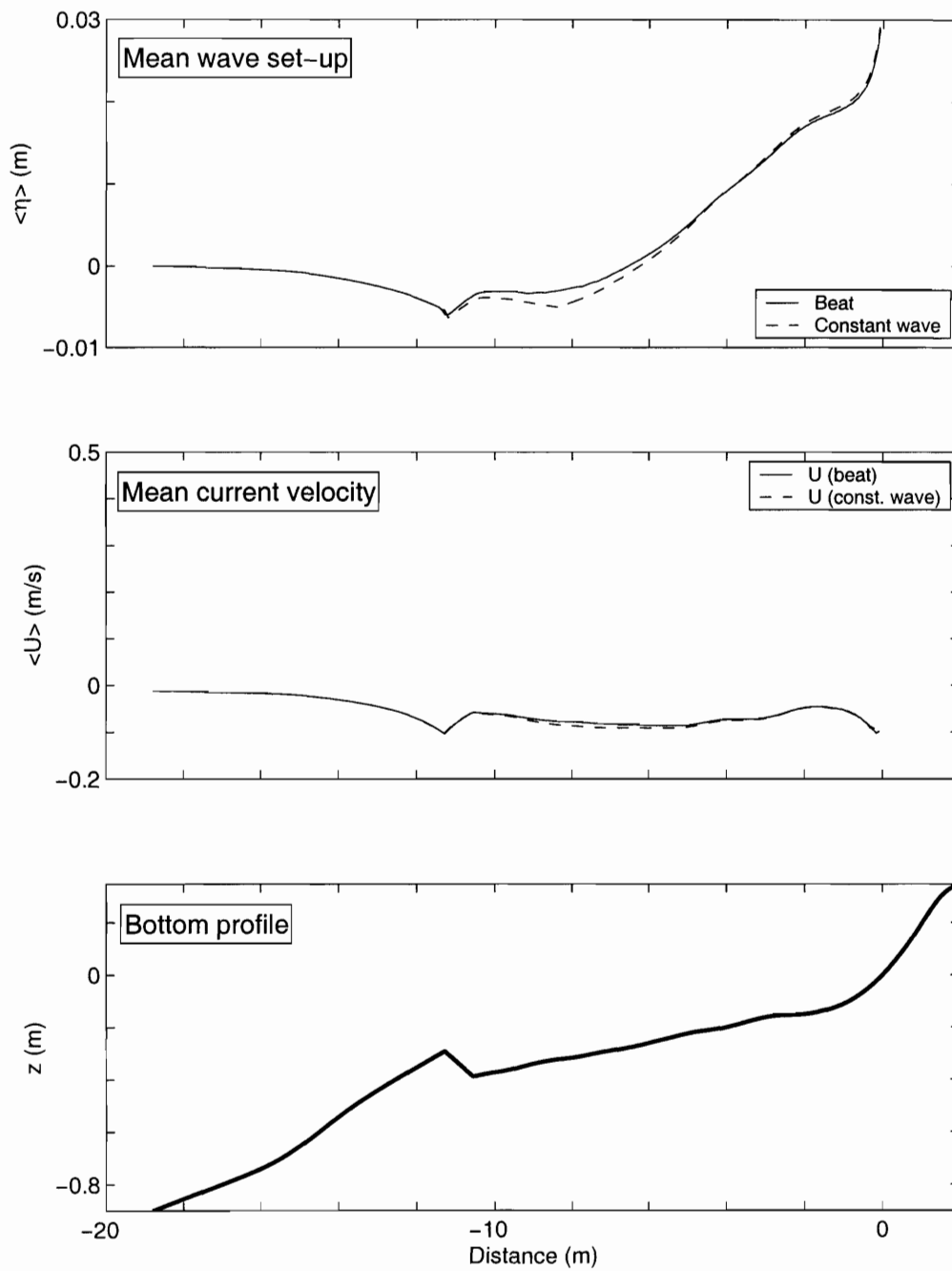Figure 4-5: Comparison between the beat averaged results of the unsteady hydrodynamic model (referred as "beat") and Tajima's monochromatic model results (referred as "constant wave"). Mean set-up (upper graph) and mean current velocities over the whole depth (middle graph).

of the beach slope, $\tan \beta$.

Similar to the case studied in the previous section, it takes a small number of beat periods to achieve convergence. We present the results after a time equal to 10 wave beats, when convergence has already been reached and the hydrodynamic behavior of the system is periodic in the wave beat.

Wave set-up

Figure 4-6 shows the mean wave set-up at different times of a beat period, for different values of the slope, $\tan \beta$. Specifically, we consider the times $10.00 T_{beat} = 151.20$ s, $10.25 T_{beat} = 154.98$ s, $10.50 T_{beat} = 158.76$ s, and $10.75 T_{beat} = 162.54$ s. As indicated before, the results for $11.00 T_{beat}$ would be equal to the results for $10.00 T_{beat}$, due to periodicity.

For the steep slope cases ($\tan \beta = 0.1$ and $\tan \beta = 0.05$), the onshore region — the region of the beach onshore of the breakpoint— is *short* when compared to the beat wavelength. Therefore, we expect a rapid response of the water body to the beat variation. In agreement with this, the water body oscillates following the beat, with a single node located next to the breakpoint. The wave set-up variation with respect to time, over the eleventh beat of the simulation, is plotted for specific nodes inside the onshore region in Figure 4-7, for $\tan \beta = 0.1$ (plots (a) and (b)) and for $\tan \beta = 0.05$ (plots (c) and (d)). The wave set-up follows an oscillatory behavior induced by the wave beat. For each slope, two different locations are presented to show that, since the onshore region is *short*, the set-up variations are in phase. We observe that, in all selected cross-shore locations, the time-average set-up predicted by the unsteady model (solid horizontal line) is larger than Tajima's steady monochromatic model's solution for H_{rms} (dashed horizontal line).

For the intermediate slope value ($\tan \beta = 0.025$), the length of the onshore region is of the order of magnitude of half the beat wavelength. Since the beat has been assumed to propagate at the wave group velocity, C_g, the beat half-wavelength is $1/2\, C_g T_{beat}$. An average value of the wave group velocity in the onshore region (from the breakpoint, around $h = 0.13$ m, to the shoreline) is $C_g = 0.68$ m/s. This average

87
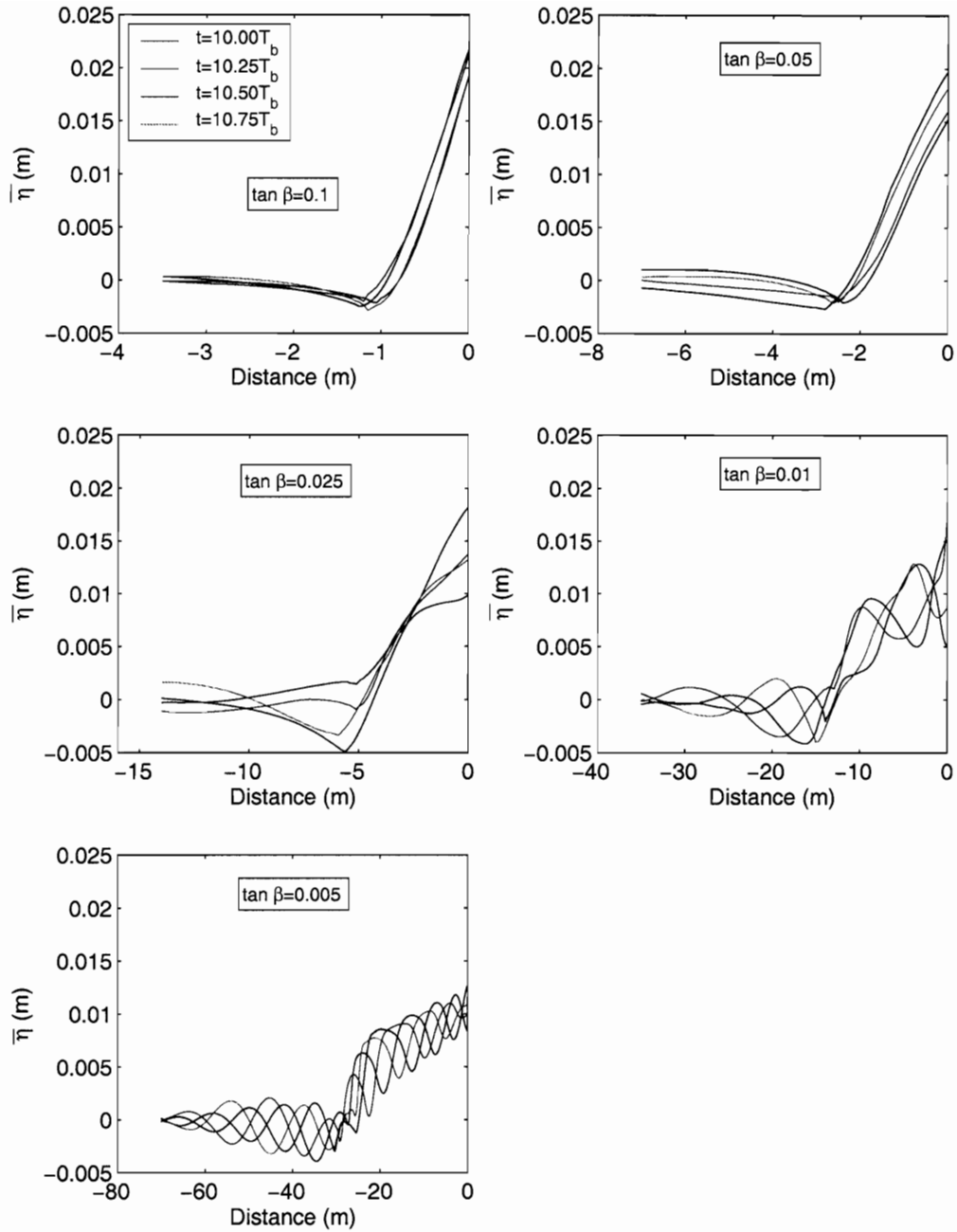
Figure 4-6: Mean wave set-up evolution over the wave beat in plane beaches with different values of the slope, $\tan \beta$.
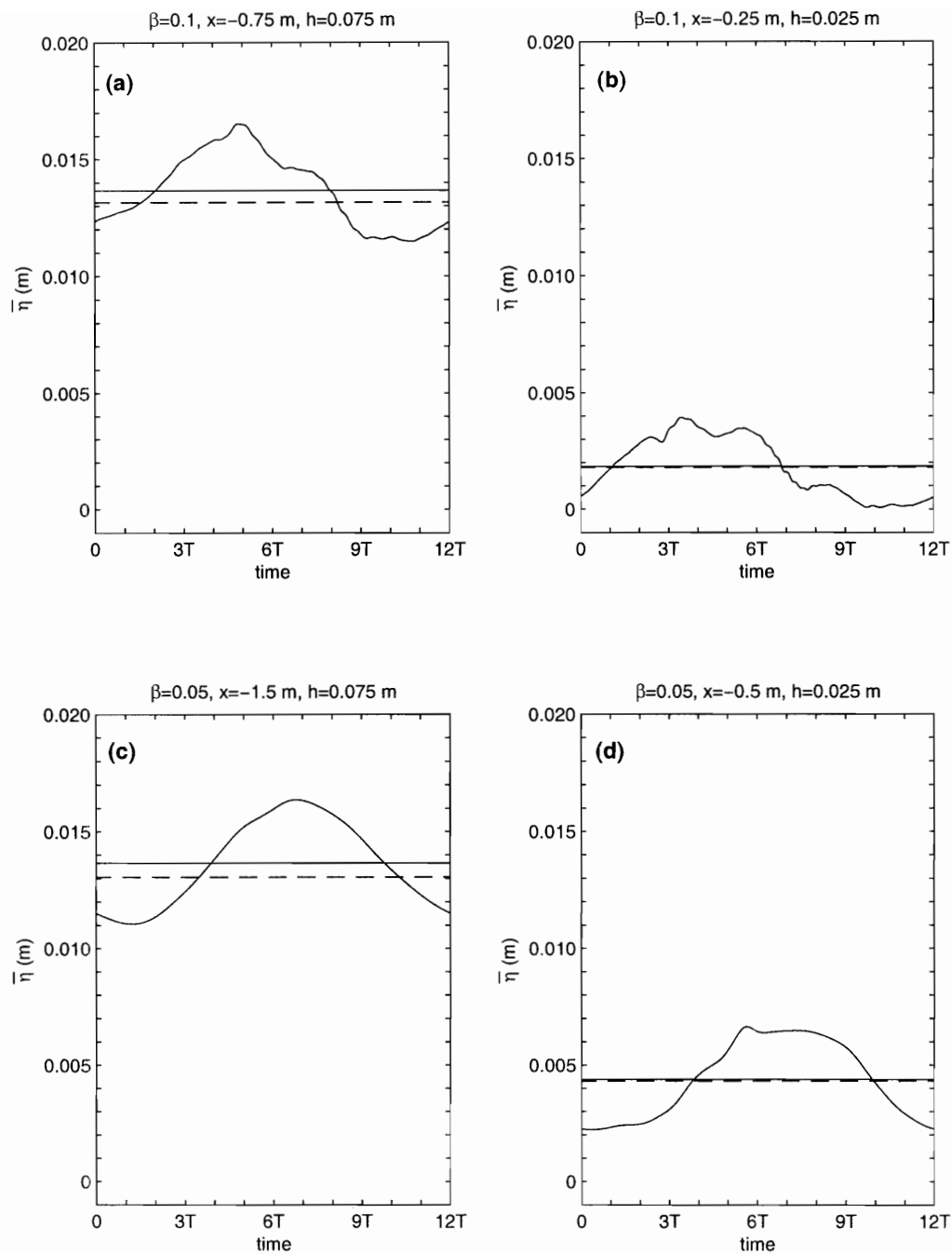
Figure 4-7: Mean wave set-up evolution over the wave beat in plane beaches of steep slope at specific cross-shore locations: (a) $\tan\beta = 0.1$, $x = -0.75$ m; (b) $\tan\beta = 0.1$, $x = -0.25$ m; (c) $\tan\beta = 0.05$, $x = -1.5$ m; (d) $\tan\beta = 0.05$, $x = -0.5$ m. The horizontal solid line represents the time-average value and the horizontal dashed line is Tajima's steady monochromatic model solution.
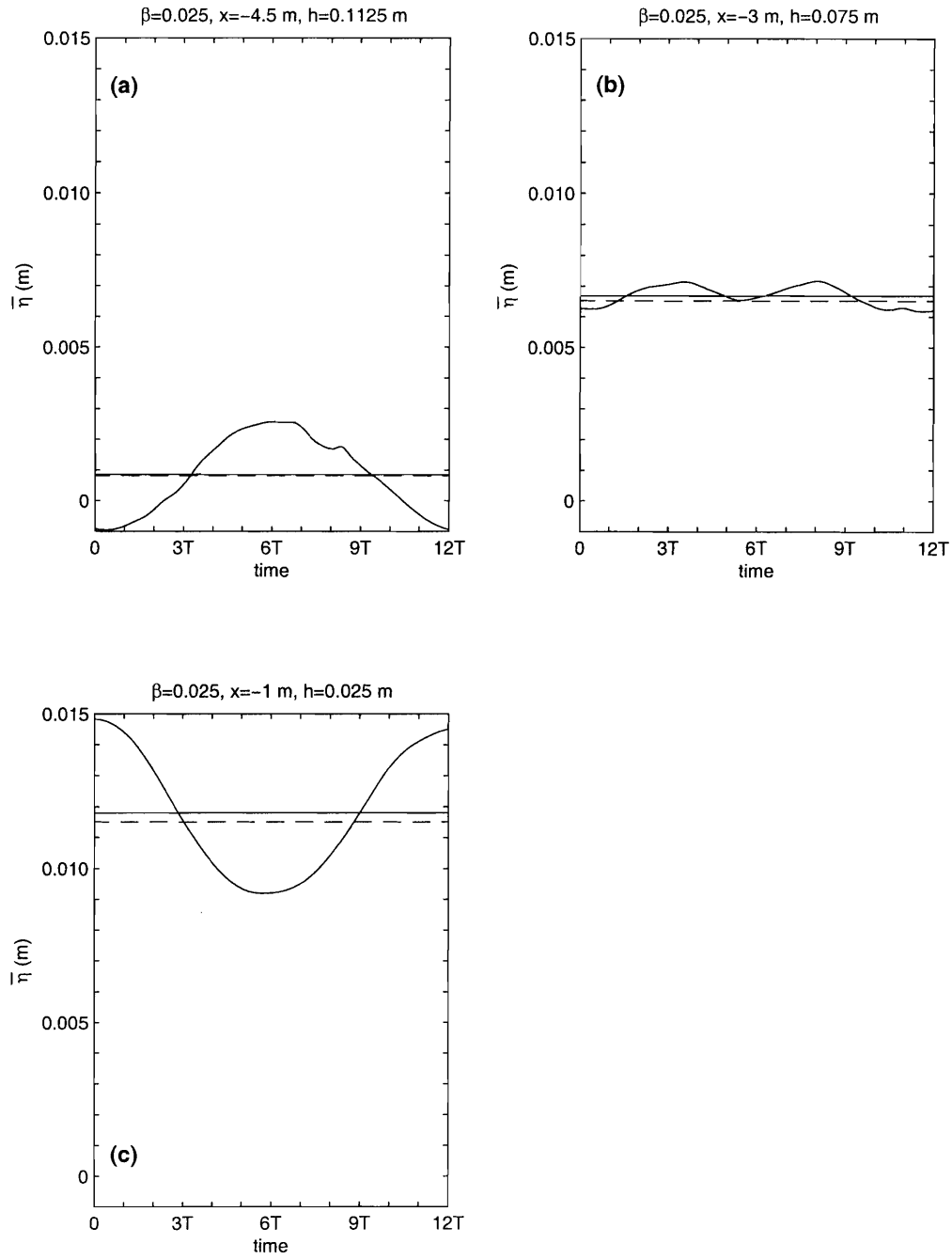
Figure 4-8: Mean wave set-up evolution over the wave beat in a plane beach of intermediate slope, $\tan\beta = 0.025$, at specific cross-shore locations: (a) $x = -4.5$ m; (b) $x = -3$ m; (c) $x = -1$ m. The horizontal solid line represents the time-average value and the horizontal dashed line is Tajima's steady monochromatic model solution.

value yields a beat half-wavelength of 5.2 m, which coincides with the onshore region length. For this reason, in this case, different stages of the wave beat variation are present at different positions of the beach at the same time. This can be seen in Figure 4-8, which represents the wave set-up evolution for specific cross-shore locations over the eleventh beat of the simulation. For time $t = 6T$, i.e., at the middle of this eleventh beat, the wave set-up is maximum at $x = -4.5$ m, average at $x = -3$ m, and minimum at $x = -1$ m, since the distance between these locations is about one quarter of the beat wavelength. The general picture along the beach is a water body oscillation with two nodes, one located in the offshore region and the other around $x = -3$ m (see Figure 4-8 (b)).

For mild slopes ($\tan \beta = 0.01$ and $\tan \beta = 0.005$), the length of the onshore region is significantly larger than the beat half-wavelength. Consequently, we observe a wavy profile of the set-up in the cross-shore direction, caused by the sequence of beats propagating shoreward. For a given cross-shore location, the set-up still exhibits a rather sinusoidal shape, as shown in Figure 4-9. The two cross-shore locations represented in Figure 4-9 are separated by a distance of 6 m, of the order of the beat half-wavelength (about 5.2 m); therefore, their respective wave set-up variations are out of phase.

Here, we have analyzed the effect of the beach slope on the set-up profile. The influence of changing the wave period, T_{wave}, or the beat period, T_{beat}, is similar. Long wave periods or long beat periods make the water body response look fast in comparison. Therefore, longer wave or beat periods have similar influence as steeper slopes, and vice versa.

Estimate of sediment transport

The ultimate goal of improving Tajima's hydrodynamic model is to investigate the influence of the suggested model modifications on sediment transport predictions in the surf zone. Sediment transport gradients lead to changes in beach bathymetry, as
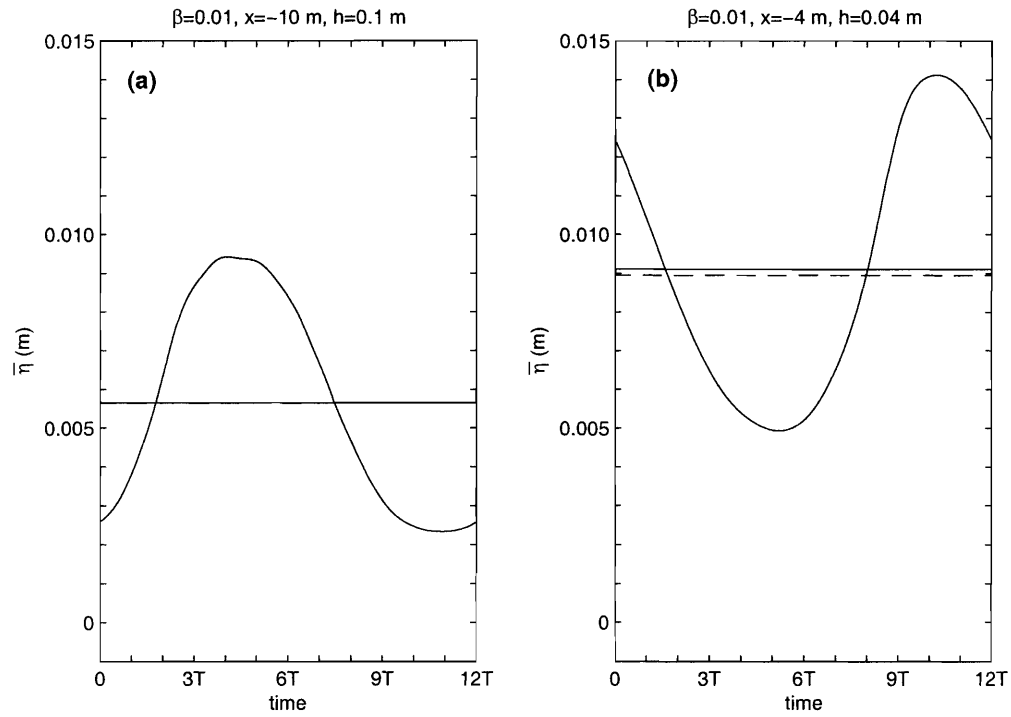
Figure 4-9: Mean wave set-up evolution over the wave beat in a plane beach of mild slope, $\tan\beta = 0.01$, at specific cross-shore locations: (a) $x = -10$ m; (b) $x = -4$ m. The horizontal solid line represents the time-average value and the horizontal dashed line is Tajima's steady monochromatic model solution.

expressed by the equation of conservation of sediment in the bottom,

$$\frac{\partial \zeta}{\partial t} = -\frac{1}{1-n}\frac{\partial Q_s}{\partial x} \tag{4.65}$$

where ζ is the bottom elevation, Q_s is the volumetric rate of sediment transport per unit width, and n is the porosity of the bed.

The sediment transport rate is calculated as

$$Q_s = \overline{\int_{-h}^{\eta} c_s u \, dz} \tag{4.66}$$

where c_s is the concentration of sediment and u is the horizontal fluid velocity. The integration is carried out over the entire water depth and the overbar denotes time-average over the wave beat. As a rough approximation, we assume c_s to account for both the suspended sediment and the bedload. c_s is proportional to the excess bottom shear stress, $(\tau - \tau_{cr}) \simeq \tau$, which is in turn proportional to u_{bm}^2, the wave bottom orbital velocity squared. The horizontal fluid velocity carrying the sediment, u, can be represented by the depth-averaged undertow, U_0. Therefore, as a first estimate, the sediment transport rate can be considered proportional to $\overline{u_{bm}^2 U_0}$. Note that, in this estimate, c_s is approximated by a depth-independent quantity, and no explicit depth integration is involved. The gradient of the sediment transport rate is then proportional to $\partial(\overline{u_{bm}^2 U_0})/\partial t$. Due to conservation of sediment, (4.65), erosion occurs when the sediment transport gradient is positive, and deposition when it is negative. The maxima of the sediment transport gradient correspond to bottom troughs, and the minima to bottom crests.

Figures 4-10 to 4-15 show the influence of the wave beat on the magnitude $\overline{u_{bm}^2 U_0}$, representative of sediment transport rate. The bathymetries correspond to four of the plane beach cases presented in Figure 4-6. Figures 4-10, 4-12, 4-14, and 4-15 represent magnitudes across the beach profile. Upper plots in these figures show the beat variations of u_{bm} and U_0. Only the values corresponding to $t = 10.25T_{beat}$ and $t = 10.75T_{beat}$ are plotted, since these approximately correspond to maximum and minimum values of sediment transport for the steeper beach cases. The estimate
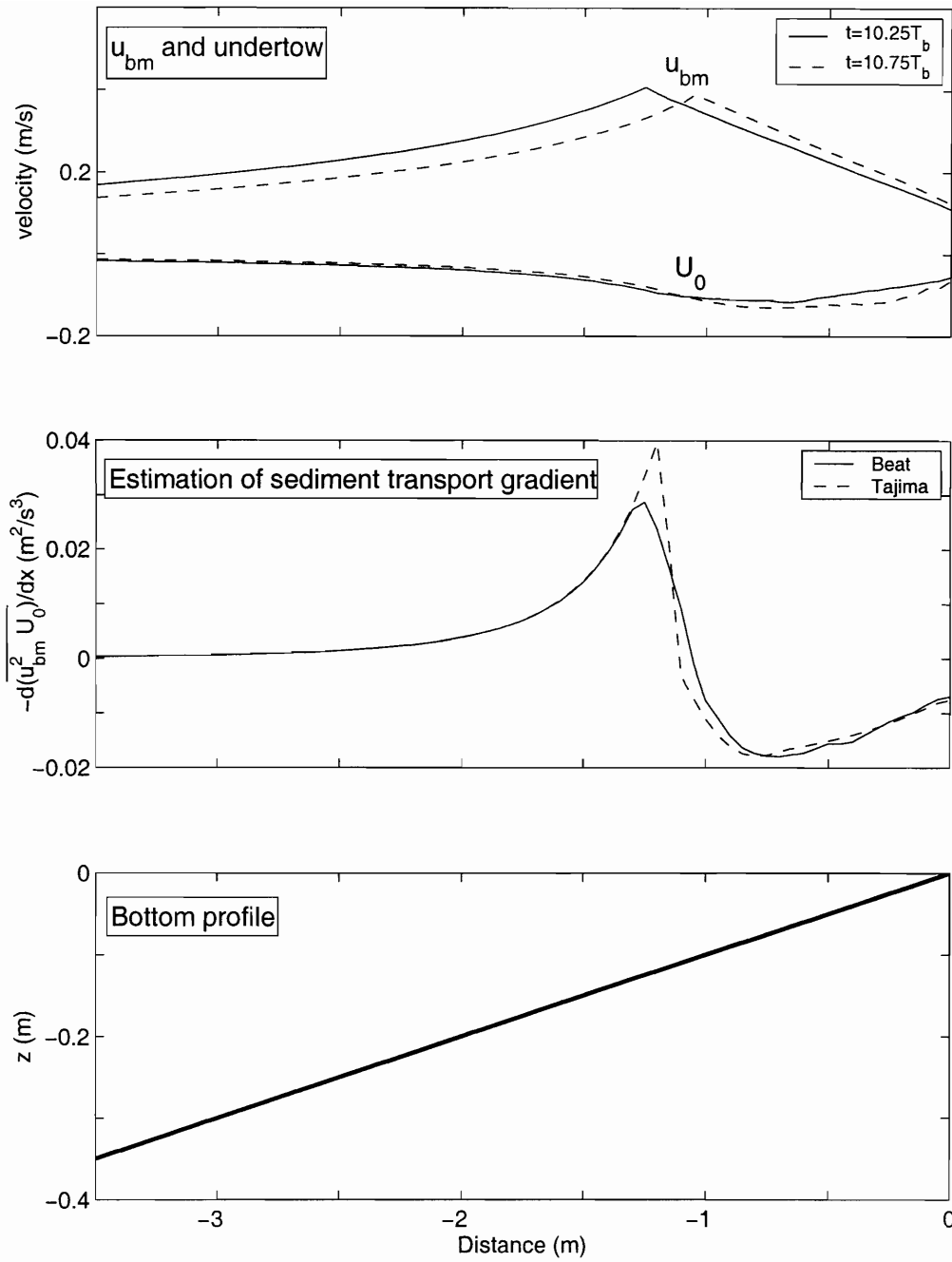
Figure 4-10: Wave bottom orbital velocity, undertow, and estimation of sediment transport gradient for a plane beach of slope $\tan \beta = 0.1$.

of $Q_s \propto \overline{u_{bm}^2 U_0}$ is calculated as a time-averaged value over the wave beat. Changes in the beach profile are governed by the cross-shore gradient of sediment transport, $\partial Q_s/\partial x$, which is represented in the middle plots of the aforementioned figures by $-\partial(\overline{u_{bm}^2 U_0})/\partial x$. The minus sign is introduced so that the plots resemble the predicted bottom shape tendency. The wave beat results are compared with Tajima's monochromatic results for H_{rms}, referred in the figures as *Tajima*. Figures 4-11 and 4-13 represent the magnitudes u_{bm} and U_0 (upper plots) and $\overline{u_{bm}^2 U_0}$ (lower plots) over the eleventh period of the simulation for specific cross-shore locations. In these two figures, the beat-averaged quantities (solid horizontal lines) are also compared to Tajima's steady monochromatic model solutions for H_{rms} (dashed horizontal lines).

In the steep beach case (Figures 4-10 and 4-11, $\tan\beta = 0.1$), the water body responds rapidly to the wave beat. Therefore, larger wave heights (with larger u_{bm}) cause an almost immediate increase of the undertow, U_0. For this reason, as seen in Figure 4-10, u_{bm} and U_0 are in phase (note the negative sign of U_0). This is shown in Figure 4-11 for $x = -0.75$ m, onshore of the breakpoint. The undertow is larger when u_{bm} is larger and there is more sediment in suspension. This coupling of effects provides a mechanism to increase sediment transport, which would have been neglected if we had only calculated the average values of u_{bm} and U_0 instead of accounting for their variation over the wave beat. Indeed, as shown by comparing the sediment transport rates of the beat and the constant wave case (Figures 4-10 and 4-11), this mechanism causes an increase of sediment transport in the onshore region. The magnitude of the increase of sediment transport gradient is small (under 5%), since the beat wave height variation is also small (10%), but it may become significant if the beat variation is larger. Note in Figure 4-10 that, near the shore, Tajima's sediment transport gradient prediction becomes larger than the beat result. This is consistent with the fact that Tajima's model overpredicts the wave height in the region closer to the shoreline, as discussed in Section 3.3 (see Figure 3-1). A major difference between the beat and the constant wave results is that the sediment transport gradient varies across the profile in a smoother way for the former (see Figure 4-10). This is due to the fact that the constant wave has a constant breakpoint

Figure 4-11: Wave bottom orbital velocity, undertow, and estimation of sediment transport for a plane beach of slope $\tan\beta = 0.1$ at $x = -0.75$ m. Horizontal solid lines represent time-average values and horizontal dashed lines are Tajima's steady monochromatic model solutions.
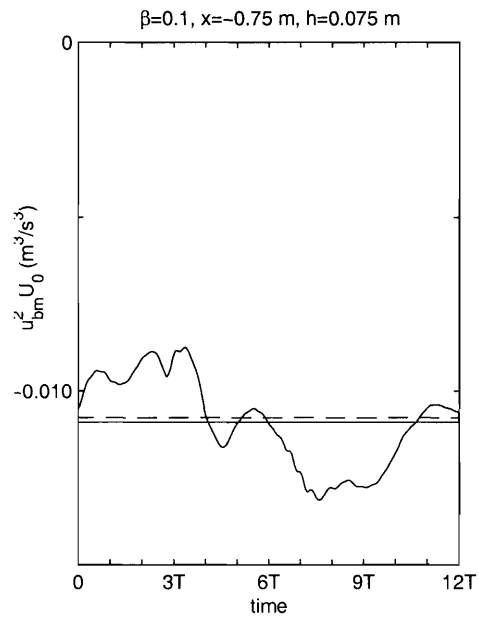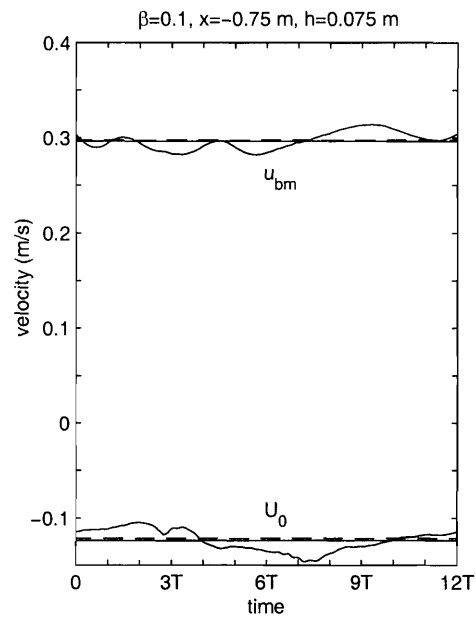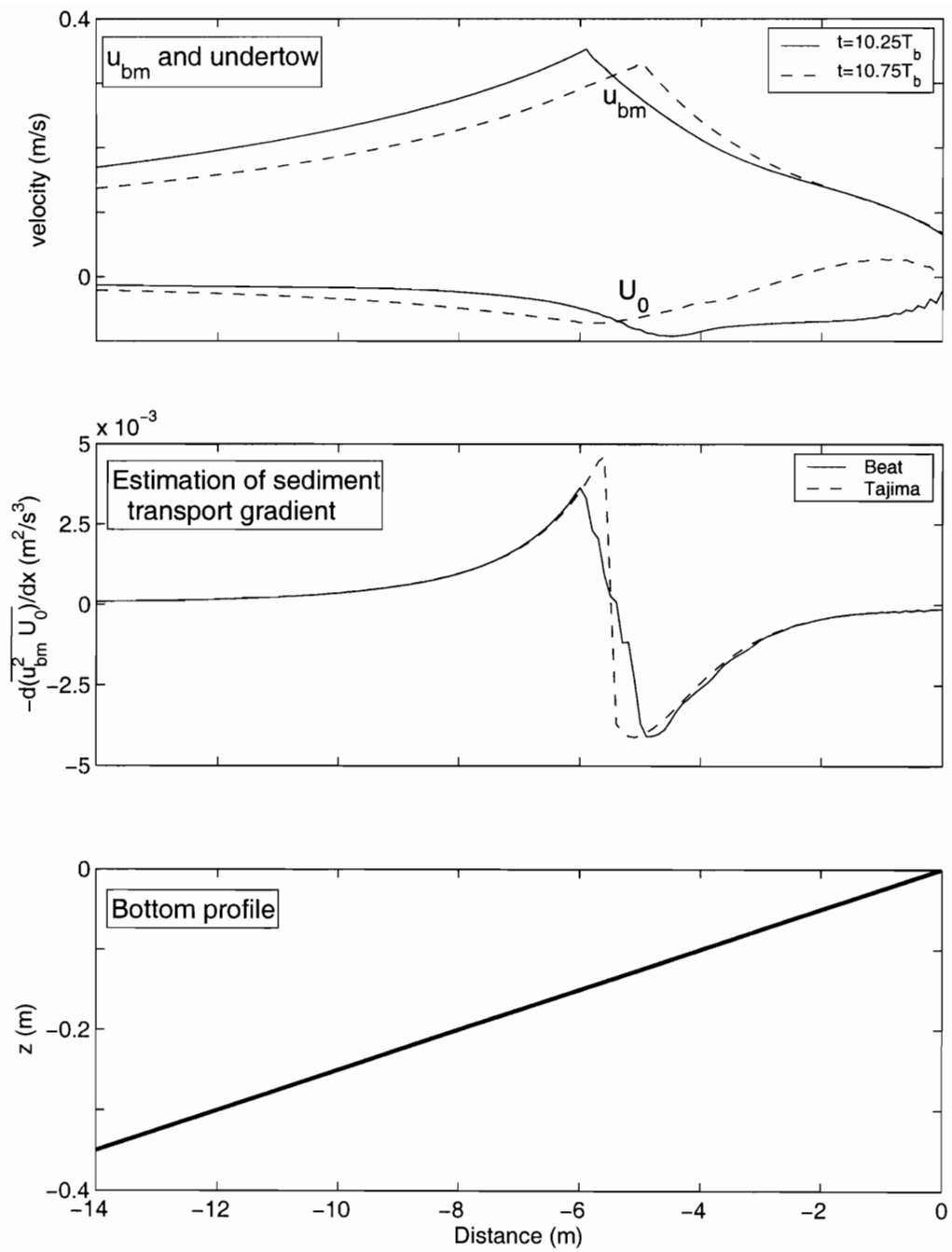
Figure 4-12: Wave bottom orbital velocity, undertow, and estimation of sediment transport gradient for a plane beach of slope $\tan\beta = 0.025$.

location, which causes the sharp shape of the sediment transport gradient. In contrast, the wave beat has a variable breakpoint, since the wave height is variable, which yields a smooth beat-averaged sediment transport gradient.

For intermediate slopes (Figures 4-12 and 4-13 (a), $\tan \beta = 0.025$), the water body response to the beat is slower. U_0 is now out of phase with u_{bm} and the aforementioned coupling process no longer happens. In Figure 4-12, the represented times approximately correspond to extreme values of U_0 and sediment transport, but they yield intermediate values for u_{bm} in the onshore region. For this reason, in Figure 4-12, u_{bm} appears to be constant in the onshore region. This is not the case, as shown by the time evolution of u_{bm} at $x = -1$ m, represented in Figure 4-13 (a). Also note in Figure 4-12 how the locations of the predicted bar crest and bar trough (corresponding to maximum and minimum values of $-\partial(\overline{u_{bm}^2 U_0})/\partial x$, respectively) are very different from the steady case. The bar crest has migrated seaward and the bar trough shoreward with respect to the steady case.

For mild slopes (Figures 4-14 and 4-13 (b), $\tan \beta = 0.01$, and Figure 4-15, $\tan \beta = 0.005$), the cross-shore variation of U_0 shows undulations corresponding to different wave beats propagating towards the shore. The average value of these beats yields a sediment transport variation significantly smoother than in the constant wave case. Therefore, the sediment transport gradient is notably smaller, and we expect slower changes in the beach bathymetry. We observe again that the predicted positions of the bar crest and trough have moved seaward and shoreward, respectively, with respect to the steady model results. The small bottom undulations predicted in Figure 4-15 ($\tan \beta = 0.005$) correspond to variations within the length scale of the local wavelength. Since all results from the hydrodynamic model are averaged values over a wave period, these small undulations must be disregarded. We note that the average predicted sediment transport gradient inside the surf zone is similar to the constant wave case. However, the time variation predicted by the unsteady model is noticeable. Consider for instance the cross-shore location $x = -6m$ in the $\tan \beta = 0.01$ beach. The average sediment transport gradient is almost the same for the steady and unsteady cases (Figure 4-14). However, the time variation of the
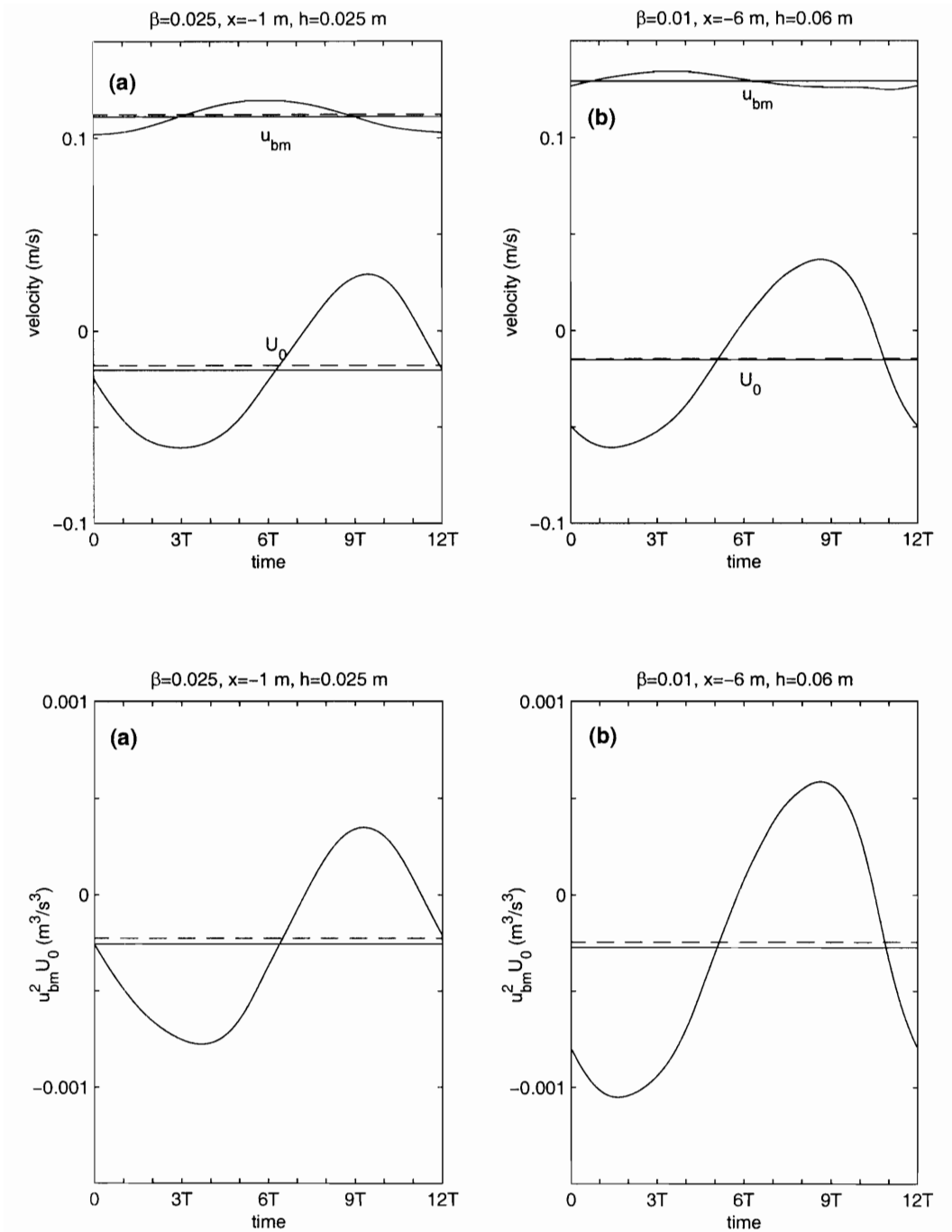
Figure 4-13: Wave bottom orbital velocity, undertow, and estimation of sediment transport for plane beaches at specific cross-shore locations: (a) $\tan \beta = 0.025$, $x = -1$ m; (b) $\tan \beta = 0.01$, $x = -6$ m. Horizontal solid lines represent time-average values and horizontal dashed lines are Tajima's steady monochromatic model solutions.
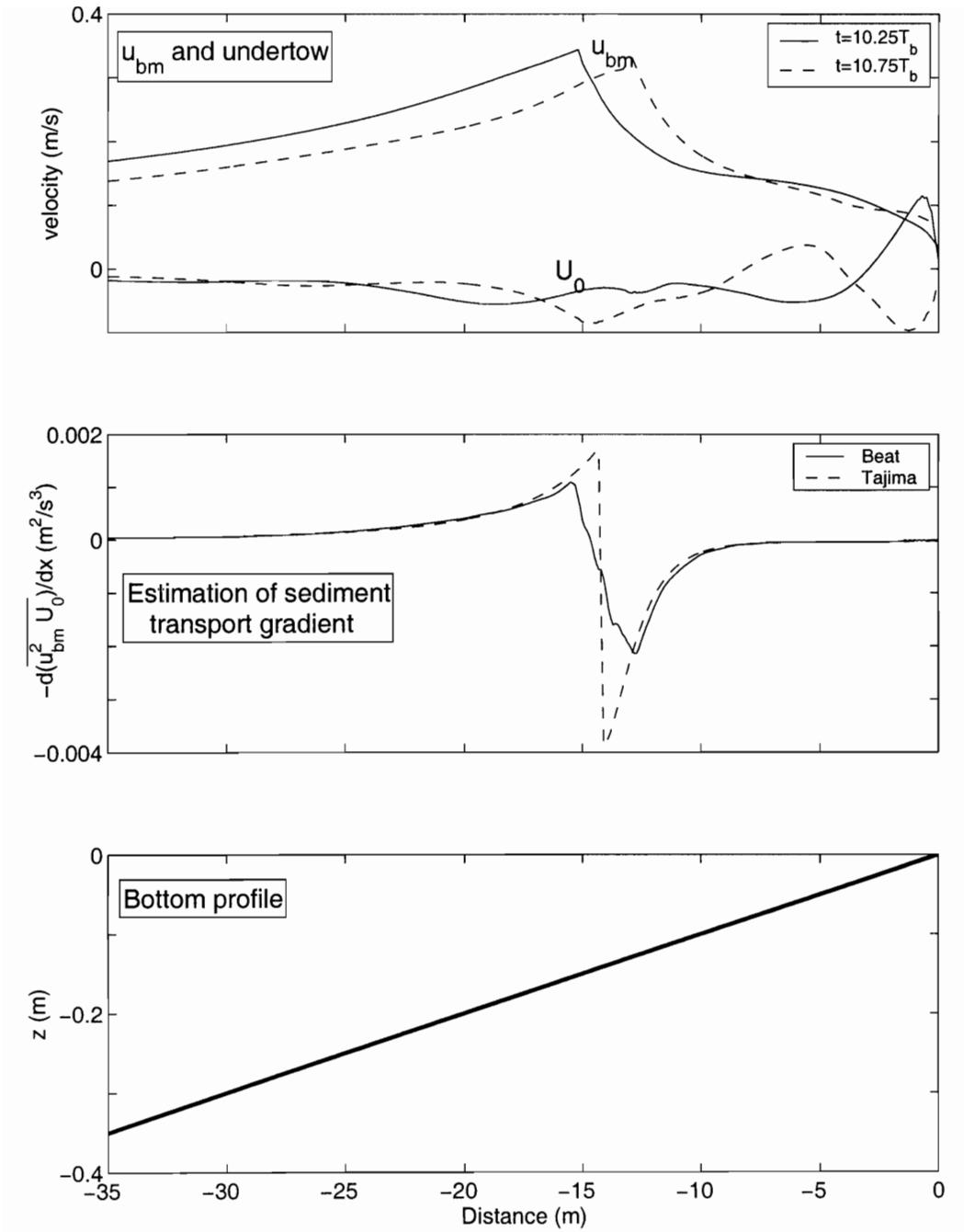
Figure 4-14: Wave bottom orbital velocity, undertow, and estimation of sediment transport gradient for a plane beach of slope $\tan \beta = 0.01$.
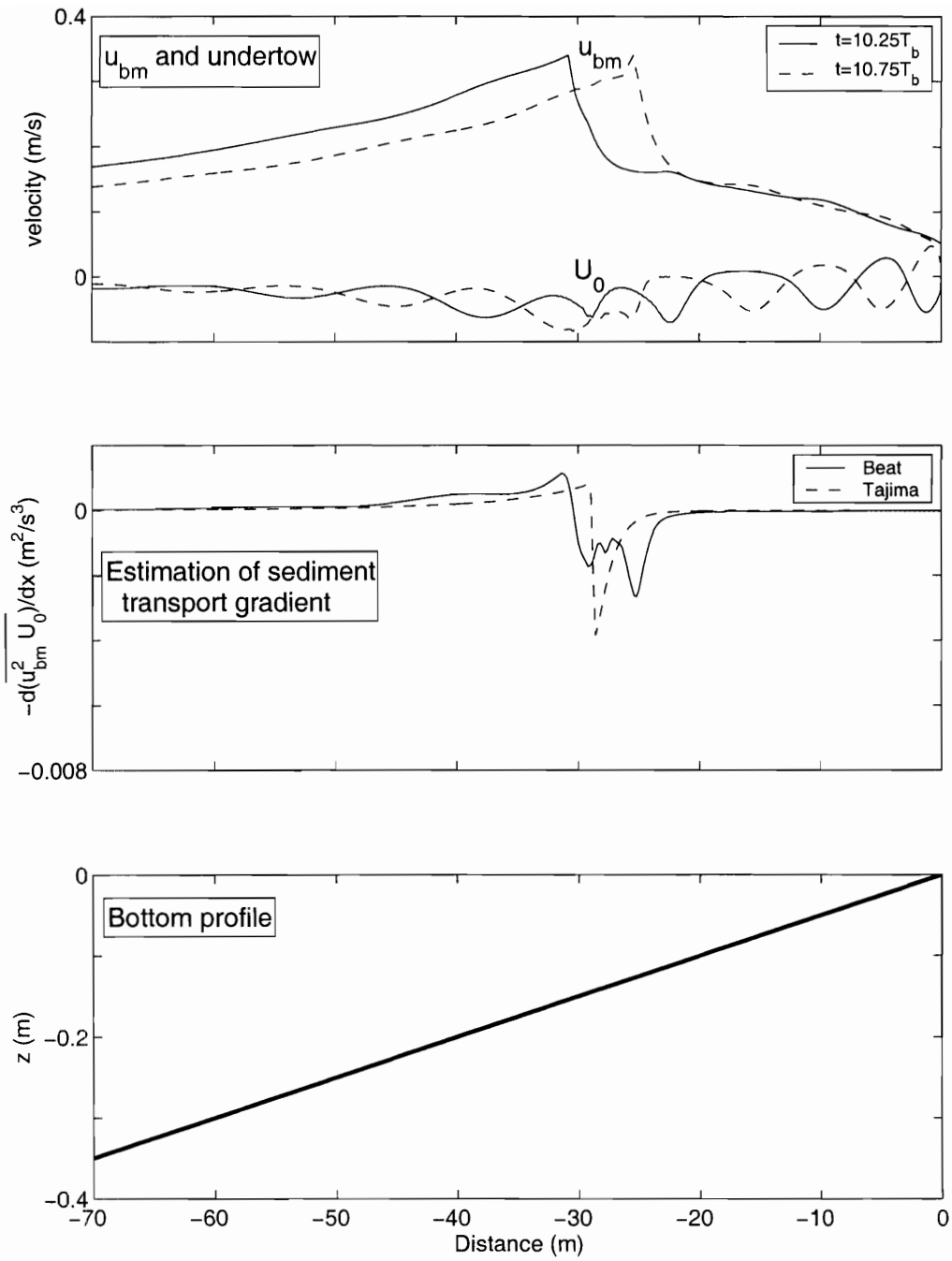
Figure 4-15: Wave bottom orbital velocity, undertow, and estimation of sediment transport gradient for a plane beach of slope $\tan \beta = 0.005$.

transport rate in the unsteady case is about six times larger than its average magnitude, yielding both onshore and offshore transports, as shown in Figure 4-13 (b), while the beat wave height variation is only 10%. In this test, the large unsteady deviations with respect to the steady mean transport compensate each other, but they suggest the potentiality of the unsteady model to yield significant corrections of the average transport predictions, when asymmetry and skewness of the waves are accounted for and the beat wave height variation is larger.

Chapter 5

Concluding remarks

This thesis had a dual purpose. First, we wanted to assess the suitability of Tajima's (2004) hydrodynamic model, by comparing it with previously existing models, as well as with a new accurate wave-by-wave approach based on well-established statistical wave descriptions. Second, we intended to generalize Tajima's hydrodynamic model to the unsteady case. This improved model will allow us to account for unsteady hydrodynamic phenomena relevant for sediment transport, and thus improve cross-shore sediment transport predictions.

In this chapter, we summarize the conclusions of this thesis and suggest directions for future improvement of the hydrodynamic and sediment transport model, which has as its ultimate objective to obtain accurate predictions of sediment transport in the nearshore region of long straight beaches.

5.1 Conclusions

- Tajima's linear wave model yields more accurate results than previously existing wave models. In the test cases shown in Chapter 2, Tajima's average linear errors with respect to measurements are 3-9%, while Battjes and Janssen's (1978) are 4-17% and Thornton and Guza's (1983) are 9-13%. In contrast to these older models, Tajima's wave model presents convenient features: It is fully predictive and it does not require parameter fitting, which affects significantly

the results of other models; it can be applied to monochromatic waves and therefore it can be used in conjunction with statistical descriptions of wave heights and periods, as shown in Chapter 3, and provide estimates of non-linear near-bottom wave orbital velocity, accounting for asymmetry and skewness, which may be important for sediment transport predictions. These calculations cannot be done using existing spectral models, such as Battjes and Janssen's, Thornton and Guza's or Tajima's simple spectral model.

- Tajima's surface roller model, based on Dally and Brown (1995), yields similar results to Stive and De Vriend's (1994) formulation. This confirms the validity of the choice of Tajima's as our surface roller model.

- We have developed a methodology for using Tajima's hydrodynamic model with a wave characterized by a joint probability distribution of heights and periods, which we referred to as the probabilistic wave-by-wave approach. Specifically, we recommend Longuet-Higgins's 1983 distribution, without accounting for different period durations in the probabilistic average of individual wave results. We have compared the hydrodynamic results of Tajima's model based on Longuet-Higgins's 1975 and 1983 distributions with the results from his own ideally narrow-banded spectral distribution. The agreement is reasonably good, although Tajima's simple spectral model's predicted radiation stresses appear displaced seaward with respect to the results of the more accurate statistical description. As a result of this comparison, we recommend that Tajima's simple spectral model is characterized by the average wave period, T_{ave}, instead of the peak period, T_{peak}, as originally suggested by Tajima. This allows to reasonably represent narrow banded spectra up to $\nu = 0.6$. However, for either choice of the representative period, Tajima's model overpredicts near-shore wave heights and undertow with respect to the wave-by-wave approach.

- We have derived the governing equations for the generalized unsteady hydrodynamic model. We have also developed a numerical scheme for their implementation. Examples of application of the unsteady model were shown in Chapter 4.

- Using the unsteady hydrodynamic model, we have studied the effect of a wave beat propagating on a plane sloping beach. For steep beaches (or, equivalently, long waves or long beats), we have identified how the rapid response of the water body to the beat induces a coupling of effects between the wave height and the undertow. We expect this mechanism to enhance suspended sediment transport, although its quantitative importance in the analyzed cases was small, since the variation of the wave height over the beat represented a small fraction (10%) of the mean height. The unsteady model predicts a smoother bottom shape than Tajima's steady monochromatic model, and locations of bar crests and troughs displaced seaward and shoreward, respectively, with respect to Tajima's model.

5.2   Future work

To achieve more accurate predictions of sediment transport, different aspects of Tajima's model need to be refined. This thesis focused on the improvement of Tajima's hydrodynamic model by generalizing it to the unsteady case. Further improvements of the hydrodynamic model are still necessary. Even under the assumption of long straight beach, obliquely incident waves will cause inhomogeneity in the long-shore (y) direction if we allow for unsteadiness. Therefore, development of a two dimensional unsteady formulation and of the corresponding numerical scheme, based on the general 2D equations presented in Appendix B, is necessary. The main difficulty in developing a 2D model is the definition of the lateral boundary conditions. The simple radiation condition applied at the offshore boundary in the present 1D model is not appropriate for the lateral boundaries, where the water depth varies from deep to shallow, and the direction of incidence of long wave disturbances is difficult to know a priori.

The bottom shear stress model used by Tajima also needs to be refined. As it is shown in Tajima (2004), the cross-shore sediment transport is not only very sensitive to the magnitude of the bottom shear stress, but also to the formulation chosen to

describe its variation in time. The bottom shear stress can be expressed as

$$\tau_b(t) = \frac{1}{2}\rho f_{cw}|u_b(t)|u_b(t) \tag{5.1}$$

where f_{cw} is the combined wave-current friction factor, and $u_b(t)$ is the near-bottom wave orbital velocity. An accurate description of how $u_b(t)$ changes in time requires to account for the asymmetry and skewness of the waves. In addition, we have to consider the time-variation of f_{cw}. f_{cw} is assumed constant by Tajima; in the unsteady model presented in this thesis, it is assumed to vary from wave to wave. However, if we account for wave asymmetry, f_{cw} becomes dependent on time within each wave period. According to (2.45), f_{cw} is a function of k_n/A_{bm}, where k_n is the bottom roughness and A_{bm} is the near-bottom orbital amplitude. For skewed and asymmetric waves, A_{bm} is variable over the wave period and so is f_{cw}.

These refinements of the bottom shear stress formulation will allow the improvement of the sediment concentration distribution model. In Tajima (2004), the sediment concentration distribution is defined as a function of a reference concentration, $C_r(t)$, at a certain depth $z = z_r$. This reference concentration is a function of the bottom shear stress and, therefore, it is time-dependent. However, in his calculations, Tajima uses the time-averaged value of $C_r(t)$ to predict sediment concentration. Future work needs to be conducted to account for the time-dependency of C_r, which will yield a temporal variation of the suspended sediment concentration, $C_s = C_s(x, y, z, t)$. The importance of this time-dependency on the sediment transport rate needs to be investigated. We expect this refinement of the model to improve its capability to predict cross-shore sediment transport in the nearshore region.

Appendix A

Integrability of the energy flux integral

We want to determine for which values of the constants r and t

$$I = \int_0^\infty \int_0^\infty \xi^r \tau^t f_{\xi\tau}(\xi, \tau) d\xi d\tau \tag{A.1}$$

is integrable. Here, $f_{\xi\tau}$ is one of the Longuet-Higgins density functions (1975 or 1983), defined in sections 3.1.3 and 3.1.4.

A.1   Longuet-Higgins's (1983) distribution

But for a constant factor, the integral (A.1) reads

$$\int_0^\infty \int_0^\infty \xi^{r+2} \tau^{t-2} \exp\left\{ -\xi^2 \left[1 + \frac{1}{\nu^2} \left(1 - \frac{1}{\tau} \right)^2 \right] \right\} d\xi d\tau \tag{A.2}$$

Assume $r \geq 0$, $t \geq 0$ are integers. First, we will only consider the integral in ξ. It can be expressed as

$$\tilde{I}(r) = C \int_0^\infty \xi^{r+2} e^{-B\xi^2} d\xi \tag{A.3}$$

where B and C are functions of τ only, and $B > 0$. Integrating by parts, the following

recurrence relation is found:

$$\tilde{I}(r) = \frac{r+1}{2B}\tilde{I}(r-2) \tag{A.4}$$

If r is an even integer, $r = 2k$, $k \geq 0$, by applying recurrently the previous relation, we obtain

$$\tilde{I}(r) = \frac{(2k+1)(2k-1)(2k-3)\cdot\ldots\cdot 3\cdot 1}{(2B)^{k+1}}\tilde{I}(-2) = \frac{(2k+2)!}{2^{k+1}(k+1)!}\frac{1}{(2B)^{k+1}}\frac{C}{2}\sqrt{\frac{\pi}{B}} \tag{A.5}$$

Analogously, if r is odd, $r = 2k+1$, $k \geq 0$, we obtain

$$\tilde{I}(r) = \frac{(k+1)!}{B^{k+1}}\frac{C}{2B} \tag{A.6}$$

Therefore, the original integral I can be written as

$$I = \int_0^\infty \int_0^\infty \xi^r \tau^t f_{\xi\tau}(\xi,\tau)d\xi d\tau = A\int_0^\infty \frac{1}{B^\alpha}\tau^{t-2}d\tau \tag{A.7}$$

where A is a constant, and

$$B = 1 + \frac{1}{\nu^2}\left(1 - \frac{1}{\tau}\right)^2 \tag{A.8}$$

$$\alpha = \begin{cases} k + \frac{3}{2} > 0 & \text{if } r = 2k \geq 0, \quad k \in \mathcal{Z} \\ k + 2 > 0 & \text{if } r = 2k+1 > 0, \quad k \in \mathcal{Z} \end{cases} \tag{A.9}$$

It can be easily shown that, for large values of τ,

$$\frac{1}{B} = \frac{\nu^2}{\nu^2+1} + \frac{2\nu^2}{(\nu^2+1)}\frac{1}{\tau} + O\left(\frac{1}{\tau^2}\right) \tag{A.10}$$

Therefore,

$$\frac{1}{B^\alpha} = \left(\frac{\nu^2}{\nu^2+1}\right)^\alpha + O\left(\frac{1}{\tau^\beta}\right) \tag{A.11}$$

where $\beta > 0$. Thus, the integral I can be written as

$$I = A\int_0^\infty \frac{1}{B^\alpha}\tau^{t-2}d\tau = A\int_0^\infty \left[\left(\frac{\nu^2}{\nu^2+1}\right)^\alpha \tau^{t-2} + O\left(\tau^{t-2-\beta}\right)\right]d\tau \tag{A.12}$$

108

Consequently, the integral (A.1) with the Longuet-Higgins (1983) distribution is finite if

$$t - 2 < -1 \Leftrightarrow t < 1 \tag{A.13}$$

A.2   Longuet-Higgins's (1975) distribution

For the truncated Longuet-Higgins's (1975) distribution (see equation 3.7), the integral (A.1) reads

$$\int_0^\infty \int_0^\infty \xi^{r+2} \tau^t e^{-\xi^2 D(\tau)} d\xi d\tau \tag{A.14}$$

but for a constant factor. Here,

$$D(\tau) = 1 + \left(\frac{\tau - 1}{\nu}\right)^2 \tag{A.15}$$

The integration in ξ is similar to the previous case. The integral I can be written as

$$I = \int_0^\infty \int_0^\infty \xi^r \tau^t f_{\xi\tau}(\xi, \tau) d\xi d\tau = K \int_0^\infty \frac{1}{D^\alpha} \tau^t d\tau \tag{A.16}$$

where K is a constant. For large τ,

$$\frac{1}{D^\alpha} = \left(\frac{\nu}{\tau}\right)^{2\alpha} + O\left(\frac{1}{\tau^\beta}\right) \tag{A.17}$$

where $\beta > 2\alpha$. Therefore, the integrability of I is determined by the term

$$\int_0^\infty \frac{1}{\tau^{2\alpha}} \tau^t d\tau = \int_0^\infty \tau^{t-2\alpha} d\tau \tag{A.18}$$

which is integrable if $t - 2\alpha < -1 \Leftrightarrow t < 2\alpha - 1$, where α is defined by (A.9).

Thus, the integrability condition is the following: If r is even, $r = 2k \geq 0$, I is integrable if $t < 2k + 2$. If r is odd, $r = 2k + 1 > 0$, I is integrable if $t < 2k + 3$. For $r = 2$, I is integrable if $t < 4$.

Appendix B

Derivation of expressions for trough and bottom shear stresses

Following Tajima (2004, appendix A), we derive the expressions that relate trough and bottom shear stress, at bottom and trough levels, with wave and current forcings. These expressions constitute the governing equations of the hydrodynamic model. Here, we present the unsteady generalization of Tajima's derivation.

B.1 Velocity field

The fluid velocity field, (u, v, w), can be written as

$$(u, v, w) = (U, V, W) + (\tilde{u}, \tilde{v}, \tilde{w}) \tag{B.1}$$

where (U, V, W) are the mean current components, and $(\tilde{u}, \tilde{v}, \tilde{w})$ are the deviations from the mean, due to the waves. Assume

$$O(U) = O(\tilde{u}) \ , \ O(V) = O(\tilde{v}) \tag{B.2}$$

We further assume

$$O(L_w) \ll O(L_m) \tag{B.3}$$

where L_w is the horizontal length-scale for the wave variation and L_m is the horizontal length-scale for the mean current variation. Continuity implies

$$O(W) = O\left(\frac{Uh}{L_m}\right) \simeq \frac{L_w}{L_m} O\left(\frac{\tilde{u}h}{L_w}\right) = \frac{L_w}{L_m} O(\tilde{w}) \ll O(\tilde{w}) \tag{B.4}$$

where h is the water depth. Therefore, $O(W) \ll O(\tilde{w})$. However, we note that W is not negligible with respect to $\tilde{w}$ if we calculate time averages, since the time average of $\tilde{w}$ is 0.

B.2   Time dependency of the velocity field

In the unsteady case, we model the incident wave as a wave beat. We assume the mean components of the velocity field to have a slow variation, in the long time scale of the wave beat, t_0. The wave velocities vary much faster, in the short time scale t_1. We apply the multiple scales method to write

$$t = t_0 + \epsilon t_1 \tag{B.5}$$

where $\epsilon \sim \frac{T_{wave}}{T_{beat}} \ll 1$, since the wave period, T_{wave}, is much smaller than the beat period, T_{beat}. The velocities depend on the time scales in the following way:

$$
\begin{aligned}
u(t_0, t_1) &= U(t_0) + \hat{u}(t_0) \cos \varphi(t_1) \\
v(t_0, t_1) &= V(t_0) + \hat{v}(t_0) \cos \varphi(t_1) \\
w(t_0, t_1) &= \hat{w}(t_0) \cos \varphi(t_1)
\end{aligned}
\tag{B.6}
$$

where $\hat{u}$, $\hat{v}$, and $\hat{w}$ are the amplitudes of the wave velocities, and φ is the phase. Similarly, the surface elevation with respect to the still water level (SWL), η, can be written as

$$\eta(t_0, t_1) = \bar{\eta}(t_0) + \hat{a}(t_0) \cos \varphi(t_1) \tag{B.7}$$

where $\bar{\eta}$ is the mean set-up, and $\hat{a}$ is the amplitude of the wave motion. The geo-
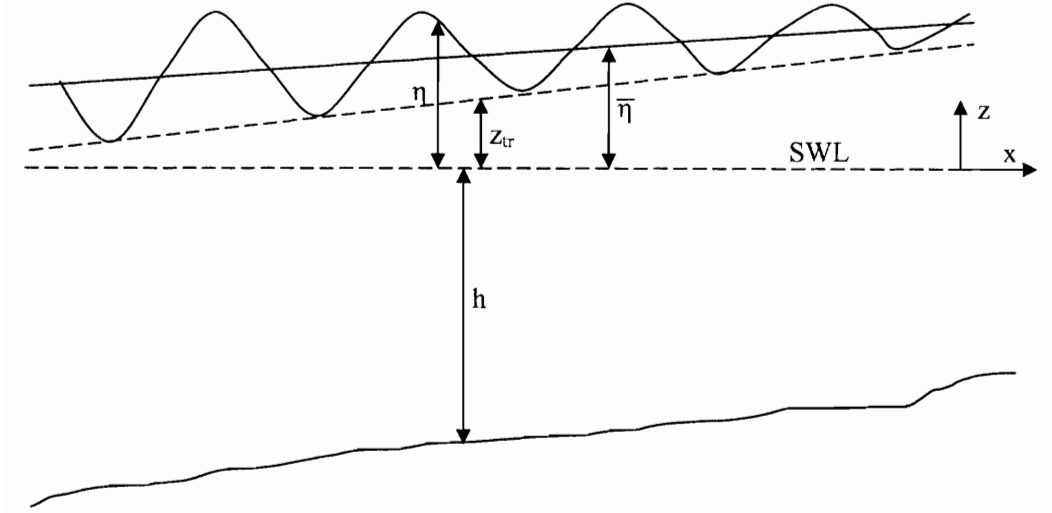
Figure B-1: Geometrical variables of the wave motion. The origin of the z axis is the still water level (SWL). η is the surface elevation, $\bar{\eta}$ is the mean set-up, z_{tr} is the elevation of the wave trough, and h is the still water depth.

metrical variables involved in this derivation are represented in Figure B-1. These geometrical variables depend on the space and time scales in the following manner:

$$\begin{aligned}
\bar{\eta} &= \bar{\eta}(x, y, t_0) \\
\eta &= \eta(x, y, t_0, t_1) \\
z_{tr} &= z_{tr}(x, y, t_0) \\
h &= h(x, y)
\end{aligned}$$
(B.8)

where

$$\eta = \bar{\eta} + \hat{a}\cos\varphi$$
(B.9)

$$z_{tr} = \bar{\eta} - \hat{a}$$
(B.10)

Note in Figure B-1 that the origin of the z-axis in all calculations in this appendix is the still water level. In our definition of the nearshore current model (Chapter 2), the origin of z-axis was the bottom.

In application of the multiple scales method, the rule of differentiation with respect

113

to time is

$$\frac{\partial \bullet}{\partial t} = \frac{\partial \bullet}{\partial t_0} + \epsilon \frac{\partial \bullet}{\partial t_1} \tag{B.11}$$

Average in time is represented by an overline, i.e.,

$$\overline{\bullet} = \frac{1}{T_{wave}} \int_0^{T_{wave}} \bullet \, dt_1 \tag{B.12}$$

Note that the overline denotes the averaged value over a wave period, much shorter than the beat period. Therefore, time-averaged quantities can still vary over the time-scale of the wave beat.

B.3   Pressure force

The vertical momentum equation reads

$$\rho \left(\frac{\partial w}{\partial t} + \frac{\partial (uw)}{\partial x} + \frac{\partial (vw)}{\partial y} + \frac{\partial w^2}{\partial z} \right) = -\frac{\partial p}{\partial z} - \rho g + \frac{\partial \tau_{xz}}{\partial x} + \frac{\partial \tau_{yz}}{\partial y} + \frac{\partial \tau_{zz}}{\partial z} \tag{B.13}$$

Integrating from z_{tr} to η, and applying the kinematic free surface boundary condition, this equation yields

$$\begin{aligned}
&\rho \left[\frac{\partial}{\partial t} \int_{z_{tr}}^{\eta} w dz + \frac{\partial}{\partial x} \int_{z_{tr}}^{\eta} uw dz + \frac{\partial}{\partial y} \int_{z_{tr}}^{\eta} vw dz \right] \\
&+ \rho w_{tr} \left[\frac{\partial z_{tr}}{\partial t_0} + u_{tr} \frac{\partial z_{tr}}{\partial x} + v_{tr} \frac{\partial z_{tr}}{\partial y} - w_{tr} \right] \\
&= -p_a + p_{tr} - \rho g \left(\eta - z_{tr} \right) \\
&+ \int_{z_{tr}}^{\eta} \frac{\partial \tau_{xz}}{\partial x} dz + \int_{z_{tr}}^{\eta} \frac{\partial \tau_{yz}}{\partial y} dz + \tau_{zz,\eta} - \tau_{zz,tr}
\end{aligned} \tag{B.14}$$

where subscripts η and tr denote values at the free surface and at the trough level, respectively, and p_a is the atmospheric pressure at the surface. The pressure at the trough level, p_{tr}, reads

$$\begin{aligned}
p_{tr} = {}& p_a + \rho g \left(\eta - z_{tr} \right) \\
&+ \rho \left[\frac{\partial}{\partial t} \int_{z_{tr}}^{\eta} w dz + \frac{\partial}{\partial x} \int_{z_{tr}}^{\eta} uw dz + \frac{\partial}{\partial y} \int_{z_{tr}}^{\eta} vw dz - w_{tr}^2 \right]
\end{aligned}$$

$$+ \rho w_{tr} \left[\frac{\partial z_{tr}}{\partial t_0} + u_{tr} \frac{\partial z_{tr}}{\partial x} + v_{tr} \frac{\partial z_{tr}}{\partial y} \right]$$

$$- \int_{z_{tr}}^{\eta} \frac{\partial \tau_{xz}}{\partial x} dz - \int_{z_{tr}}^{\eta} \frac{\partial \tau_{yz}}{\partial y} dz - \tau_{zz,\eta} + \tau_{zz,tr} \tag{B.15}$$

B.4   Order of magnitude simplifications

Some simplifications can be introduced by analyzing the order of magnitude of the viscous stresses:

$$\begin{aligned}
\tau_{zx} &= \rho\nu \left(\frac{\partial u}{\partial z} + \frac{\partial w}{\partial x} \right) = \rho\nu \, O \left(\frac{\mathcal{U}}{h} + \frac{\mathcal{W}}{L} \right) \\
&= \rho\nu \, O \left(\frac{\mathcal{U}}{h} + \frac{\mathcal{U}}{h} \left(\frac{h}{L} \right)^2 \right) = \rho\nu \, O \left(\frac{\mathcal{U}}{h} \right) \tag{B.16}
\end{aligned}$$

where $\mathcal{U}$ and $\mathcal{W}$ denote the velocity scales, h is the water depth, and L is a length scale, either related with the wave or the beat, but in any case much larger than h. We have applied continuity to relate the orders of magnitude of $\mathcal{U}$ and $\mathcal{W}$. For the vertical stress component,

$$\tau_{zz} = 2\rho\nu \frac{\partial \mathcal{W}}{\partial z} = \rho\nu O \left(\frac{\mathcal{U}}{L} \right) \tag{B.17}$$

We are interested in comparing the order of magnitude of different terms in (B.15). In particular,

$$\rho \frac{\partial}{\partial x} \int_{z_{tr}}^{\eta} uw dz = O \left(\frac{\rho\nu(\eta - z_{tr})\mathcal{U}}{hL} \frac{\mathcal{W}h}{\nu} \right) \tag{B.18}$$

$$\int_{z_{tr}}^{\eta} \frac{\partial \tau_{xz}}{\partial x} dz = O \left(\frac{\rho\nu(\eta - z_{tr})\mathcal{U}}{hL} \right) \tag{B.19}$$

$$\tau_{zz,\eta} - \tau_{zz,tr} = O \left(\frac{\rho\nu(\eta - z_{tr})\mathcal{U}}{hL} \right) \tag{B.20}$$

The factor $\frac{\mathcal{W}h}{\nu}$ is the Reynolds number based on the vertical velocity and we will assume it to be much larger than 1. Therefore, terms like (B.19, B.20) are

much smaller than terms like (B.18). Consequently, the viscous stress terms can be neglected when calculating p_{tr}.

In the near-surface region, $z \geq z_{tr}$, we assume that wave orbital velocities and horizontal mean current velocities can be accurately represented by their surface values, i.e.,

$$(\tilde{u}, \tilde{v}, \tilde{w}) \simeq (\tilde{u}_s, \tilde{v}_s, \tilde{w}_s) \quad z \geq z_{tr}$$

$$(U, V) \simeq (U_s, V_s) \quad z \geq z_{tr} \tag{B.21}$$

With these assumptions, (B.15) can be rewritten as

$$
\begin{aligned}
p_{tr} = \ & p_a + \rho g(\eta - z_{tr}) \\
& + \rho \left[\frac{\partial}{\partial t} \{ \tilde{w}_s(\eta - z_{tr}) \} + \frac{\partial}{\partial x} \{ (U_s + \tilde{u}_s)\tilde{w}_s(\eta - z_{tr}) \} \right. \\
& \left. + \frac{\partial}{\partial y} \{ (V_s + \tilde{v}_s)\tilde{w}_s(\eta - z_{tr}) \} - \tilde{w}_s^2 \right] \\
& + \rho \tilde{w}_s \left[\frac{\partial z_{tr}}{\partial t_0} + (U_s + \tilde{u}_s)\frac{\partial z_{tr}}{\partial x} + (V_s + \tilde{v}_s)\frac{\partial z_{tr}}{\partial y} \right]
\end{aligned}
\tag{B.22}
$$

B.5   Mean pressure at the trough level

From (B.6), the wave velocity components can be written as

$$
\begin{aligned}
\tilde{u}(t_0, t_1) &= \hat{u}(t_0) \cos \varphi(t_1) \\
\tilde{v}(t_0, t_1) &= \hat{v}(t_0) \cos \varphi(t_1) \\
\tilde{w}(t_0, t_1) &= \hat{w}(t_0) \sin \varphi(t_1)
\end{aligned}
\tag{B.23}
$$

Introducing these expressions into (B.22) and time-averaging over a wave period, we obtain

$$\bar{p}_{tr} = p_a + \rho g \hat{a} - \frac{\rho \hat{w}_s^2}{2} \tag{B.24}$$

116

B.6   Mean pressure force above the trough level

The time-averaged mean pressure force above the trough level is defined as

$$P_s = \overline{\int_{z_{tr}}^{\eta} p\,dz} \qquad (B.25)$$

Recall that the time-average is calculated in the short-time scale of the wave period. Therefore, P_s varies in the beat time scale.

The pressure p is given by replacing z_{tr} by z in (B.22). Since $\frac{\partial z}{\partial t} = \frac{\partial z}{\partial x} = \frac{\partial z}{\partial y} = 0$, the last three terms in (B.22) now vanish. Introducing the expression for p into (B.25) we obtain, after integrating in z and time-averaging,

$$
\begin{aligned}
P_s &= p_a(\bar{\eta} - z_{tr}) + \frac{\rho g}{2}\overline{(\eta - z_{tr})^2} + \frac{\rho}{2}\overline{\frac{\partial}{\partial t}\{\tilde{w}_s(\eta - z_{tr})^2\}} \\
&\quad + \rho\frac{\partial z_{tr}}{\partial t_0}\overline{\tilde{w}_s(\eta - z_{tr})} + \frac{\rho}{2}\overline{\frac{\partial}{\partial x}\{(U_s + \tilde{u}_s)\tilde{w}_s(\eta - z_{tr})^2\}} \\
&\quad + \rho\frac{\partial z_{tr}}{\partial x}\overline{(U_s + \tilde{u}_s)\tilde{w}_s(\eta - z_{tr})} + \frac{\rho}{2}\overline{\frac{\partial}{\partial y}\{(V_s + \tilde{v}_s)\tilde{w}_s(\eta - z_{tr})^2\}} \\
&\quad + \rho\frac{\partial z_{tr}}{\partial y}\overline{(V_s + \tilde{v}_s)\tilde{w}_s(\eta - z_{tr})} - \rho\overline{\tilde{w}_s^2(\eta - z_{tr})}
\end{aligned}
\qquad (B.26)
$$

Introducing the expressions for the velocity components, (B.23), and time-averaging, the previous equation can be simplified to

$$P_s = p_a\hat{a} + \frac{E}{2} + \frac{\rho g \hat{a}^2}{2} - \frac{1}{2}\rho\hat{a}\hat{w}_s^2 \qquad (B.27)$$

where $E = \rho g\hat{a}^2/2$.

B.7   Trough shear stress

The horizontal momentum equation reads

$$\rho\left(\frac{\partial u}{\partial t} + \frac{\partial u^2}{\partial x} + \frac{\partial(uv)}{\partial y} + \frac{\partial(uw)}{\partial z}\right) = -\frac{\partial p}{\partial x} + \frac{\partial \tau_{xx}}{\partial x} + \frac{\partial \tau_{yx}}{\partial y} + \frac{\partial \tau_{zx}}{\partial z} \qquad (B.28)$$

117

After integration from $z = z_{tr}$ to $z = \eta$ and application of the kinematic free surface boundary condition, the previous equation yields

$$
\rho \left[\frac{\partial}{\partial t} \int_{z_{tr}}^{\eta} u\, dz + \frac{\partial}{\partial x} \int_{z_{tr}}^{\eta} u^2\, dz + \frac{\partial}{\partial y} \int_{z_{tr}}^{\eta} uv\, dz \right]
$$

$$
+ \rho u_{tr} \left[\frac{\partial z_{tr}}{\partial t_0} + u_{tr} \frac{\partial z_{tr}}{\partial x} + v_{tr} \frac{\partial z_{tr}}{\partial y} - w_{tr} \right]
$$

$$
= -\frac{\partial}{\partial x} \int_{z_{tr}}^{\eta} p\, dz + p_a \frac{\partial \eta}{\partial x} - p_{tr} \frac{\partial z_{tr}}{\partial x}
$$

$$
+ \int_{z_{tr}}^{\eta} \frac{\partial \tau_{yx}}{\partial y}\, dz + \tau_{ax} - \tau_{tr,zx} \tag{B.29}
$$

where $\tau_{ax} = \tau_{zx,\eta}$ is the shear stress in the surface. Due to order of magnitude arguments, the term

$$
\int_{z_{tr}}^{\eta} \frac{\partial \tau_{xx}}{\partial x}\, dz \tag{B.30}
$$

is negligible when compared with advective terms.

Assuming as before vertical uniformity of the horizontal velocity components above the trough level, (B.21), and time-averaging over a wave period, the current shear stress at the trough level, τ_{csx}, can be written as

$$
\tau_{csx} = \overline{\tau_{tr,zx}} = -\frac{\partial}{\partial x} P_s + p_a \frac{\partial \bar{\eta}}{\partial x} - \bar{p}_{tr} \frac{\partial z_{tr}}{\partial x}
$$

$$
- \rho \left[\frac{\partial}{\partial t} \int_{z_{tr}}^{\eta} u_s\, dz + \overline{\frac{\partial}{\partial x} \int_{z_{tr}}^{\eta} u_s^2\, dz} + \overline{\frac{\partial}{\partial y} \int_{z_{tr}}^{\eta} u_s v_s\, dz} \right]
$$

$$
- \rho \frac{\partial z_{tr}}{\partial t_0} \bar{u}_s - \rho \overline{u_s^2} \frac{\partial z_{tr}}{\partial x} - \rho \overline{u_s v_s} \frac{\partial z_{tr}}{\partial y} + \rho \overline{u_s w_s}
$$

$$
+ \overline{\int_{z_{tr}}^{\eta} \frac{\partial \tau_{yx}}{\partial y}\, dz} + \tau_{ax} \tag{B.31}
$$

The integrals are simplified by making use of the hypothesis introduced in (B.21). Using the results (B.24) and (B.27), the previous expression can be reduced to

$$
\tau_{csx} = -\frac{\partial}{\partial x} \left(p_a \hat{a} + \frac{E}{2} + \frac{\rho g \hat{a}^2}{2} - \frac{1}{2} \rho \hat{a} \hat{w}_s^2 \right)
$$

$$
+ p_a \frac{\partial \hat{a}}{\partial x} - \left(\rho g \hat{a} - \rho \frac{\hat{w}_s^2}{2} \right) \frac{\partial z_{tr}}{\partial x} - \rho \frac{1}{2} \frac{\partial (\hat{u}_s \hat{a})}{\partial t_0}
$$

118

$$
\begin{aligned}
&- \frac{\partial}{\partial t_0}(U_s \hat{a}) - \rho \overline{\frac{\partial}{\partial x}\left((\tilde{u}_s + U_s)^2 (\eta - z_{tr}) \right)} \\
&\overline{- \rho \frac{\partial}{\partial y}\left((\tilde{u}_s + U_s)(\tilde{v}_s + V_s)(\eta - z_{tr}) \right)} - \rho \frac{\partial z_{tr}}{\partial t_0} U_s \\
&- \rho \left(\frac{\hat{u}_s^2}{2} + U_s^2 \right) \frac{\partial z_{tr}}{\partial x} - \rho \left(\frac{\hat{u}_s \hat{v}_s}{2} + U_s V_s \right) \frac{\partial z_{tr}}{\partial y} \\
&+ \rho \overline{u_{tr} w_{tr}} + \hat{a} \frac{\partial \tau_{yx}}{\partial y} + \tau_{ax}
\end{aligned}
\tag{B.32}
$$

Introducing (B.23), we finally obtain

$$
\begin{aligned}
\tau_{csx} \;=\; & -\hat{a}\frac{\partial p_a}{\partial x} - \frac{\partial}{\partial x}\left(\frac{E}{2} \right) + \frac{\rho \hat{a}}{2}\frac{\partial \hat{w}_s^2}{\partial x} \\
& - \left(\rho g \hat{a} - \frac{\rho \hat{w}_s^2}{2} \right) \frac{\partial \bar{\eta}}{\partial x} - \frac{\rho}{2}\frac{\partial(\hat{u}_s \hat{a})}{\partial t_0} - \frac{\partial}{\partial t_0}(U_s \hat{a}) \\
& - \rho \frac{\partial}{\partial x}(\hat{a}\hat{u}_s U_s) - \frac{1}{2}\rho \frac{\partial}{\partial x}\left(\hat{a}\hat{u}_s^2 \right) - \rho \frac{\partial}{\partial x}\left(\hat{a} U_s^2 \right) \\
& - \frac{1}{2}\rho \frac{\partial}{\partial y}\left[\hat{u}_s \hat{v}_s \hat{a} + \hat{u}_s V_s \hat{a} + U_s \hat{v}_s \hat{a} \right] - \rho \frac{\partial}{\partial y}(\hat{a} U_s V_s) \\
& - \rho \frac{\partial z_{tr}}{\partial t_0} U_s - \rho \left(\frac{\hat{u}_s^2}{2} + U_s^2 \right) \frac{\partial z_{tr}}{\partial x} - \rho \left(\frac{\hat{u}_s \hat{v}_s}{2} + U_s V_s \right) \frac{\partial z_{tr}}{\partial y} \\
& + \rho \overline{u_{tr} w_{tr}} + \hat{a} \frac{\partial \tau_{yx}}{\partial y} + \tau_{ax} \\
& - \rho \frac{\partial q_{srx}}{\partial t_0} + \tau_{srx}
\end{aligned}
\tag{B.33}
$$

where the two last terms introduce the surface roller effect. The term involving q_{srx} represents the long-term variation of the flux due to the surface roller. The term τ_{srx} accounts for the fraction of the trough shear stress acting over the roller. The evaluation of the latter is discussed in the following section.

B.8 Momentum forces due to the surface roller

Inside the surf zone, there is a shear force component acting on the surface roller, which is balanced by a trough level shear stress component affecting the underlying water column. Following Tajima (2004), we assume that the mean fluid velocities in

the surface roller are affected by the mean current velocities near the surface, i.e.,

$$(u_{sr}, v_{sr}) = (C\cos\theta + U_s, C\sin\theta + V_s) \tag{B.34}$$

where C is the phase velocity and θ is the angle of incidence of the waves. Time-averaged momentum flux components due to the surface roller are then determined to be

$$\begin{pmatrix} M_{sr,xx} & M_{sr,yx} \\ M_{sr,xy} & M_{sr,yy} \end{pmatrix} = \begin{pmatrix} R_{xx} + \rho U_s q_{srx} & R_{yx} + \rho U_s q_{sry} \\ R_{xy} + \rho V_s q_{srx} & R_{yy} + \rho V_s q_{sry} \end{pmatrix} \tag{B.35}$$

where R_{ij} are the surface roller momentum flux components due to waves only, as defined in (4.5, 4.6), and q_{srj} are the volume fluxes of the roller, defined by

$$\begin{pmatrix} q_{srx} \\ q_{sry} \end{pmatrix} = \frac{S_{sr}}{T_{wave}} \begin{pmatrix} \cos\theta \\ \sin\theta \end{pmatrix} \tag{B.36}$$

The shear stresses at the trough level due to the roller are determined by

$$\tau_{srj} = -\frac{\partial M_{sr,xj}}{\partial x} - \frac{\partial M_{sr,yj}}{\partial y} \tag{B.37}$$

where j stands for x or y.

B.9 Mean vertical momentum flux at the trough level

Continuity equation reads

$$\frac{\partial u}{\partial x} + \frac{\partial v}{\partial y} + \frac{\partial w}{\partial z} = 0 \tag{B.38}$$

We integrate this equation above the trough level, from $z = z_{tr}$ to $z = \eta$. We assume that the horizontal velocity above the trough level is independent of z, according to (B.21). Taking into account the surface roller flux and applying Leibnitz rule, the

120

integration yields

$$w_{tr} = \frac{\partial}{\partial x}\left(\int_{z_{tr}}^{\eta} u_s dz + q_{srx}\right) + \frac{\partial}{\partial y}\left(\int_{z_{tr}}^{\eta} v_s dz + q_{sry}\right)$$
$$+ u_s \frac{\partial z_{tr}}{\partial x} + v_s \frac{\partial z_{tr}}{\partial y} + \frac{\partial \eta}{\partial t} \tag{B.39}$$

after introducing the kinematic free surface boundary condition. Multiplying by $u_{tr} = u_s$, the total fluid velocity in x-direction above the trough, and time-averaging,

$$\overline{u_{tr}w_{tr}} = \overline{u_s\frac{\partial}{\partial x}\left(\int_{z_{tr}}^{\eta} u_s dz + q_{srx}\right)} + \overline{u_s\frac{\partial}{\partial y}\left(\int_{z_{tr}}^{\eta} v_s dz + q_{sry}\right)}$$
$$+ \overline{u_s^2 \frac{\partial z_{tr}}{\partial x}} + \overline{u_s v_s \frac{\partial z_{tr}}{\partial y}} + \overline{u_s \frac{\partial \eta}{\partial t}} \tag{B.40}$$

The mean wave volume flux above the trough level is

$$q_{wx} = \overline{\int_{z_{tr}}^{\eta} \tilde{u}_s dz} = \frac{\hat{u}_s \hat{a}}{2} \tag{B.41}$$

The total mean volume flux above the trough level is

$$q_{sx} = \overline{\int_{z_{tr}}^{\eta} u_s dz} + q_{srx} = q_{wx} + U_s \hat{a} + q_{srx} \tag{B.42}$$

Introducing (B.23) into (B.40), and making use of the definitions (B.41) and (B.42), we conclude that the mean vertical momentum flux at the trough level is

$$\rho\overline{u_{tr}w_{tr}} = \rho\left(U_s \frac{\partial q_{sx}}{\partial x} + \left(U_s^2 + \frac{\hat{u}_s^2}{2}\right)\frac{\partial z_{tr}}{\partial x}\right)$$
$$+ \rho\left(U_s \frac{\partial q_{sy}}{\partial y} + \left(U_s V_s + \frac{\hat{u}_s \hat{v}_s}{2}\right)\frac{\partial z_{tr}}{\partial y}\right)$$
$$+ \rho\hat{u}_s\left(\frac{\partial q_{wx}}{\partial x} + \frac{\partial q_{wy}}{\partial y}\right) + \frac{1}{2}\rho\hat{u}_s\frac{\partial \hat{a}}{\partial t_0}$$
$$+ \frac{1}{2}\rho\hat{u}_s\left(U_s \frac{\partial \hat{a}}{\partial x} + V_s \frac{\partial \hat{a}}{\partial y}\right) \tag{B.43}$$

where we have made use of the fact that, by continuity,

$$\frac{\partial U_s}{\partial x} + \frac{\partial V_s}{\partial y} = 0 \qquad (B.44)$$

B.10   Mean trough shear stress

Substituting (B.37) and (B.43) into (B.33) we get, after some algebra,

$$
\begin{aligned}
\tau_{csx} \;=\; & \tau_{ax} - \hat{a}\frac{\partial p_a}{\partial x} - \rho g \hat{a}\frac{\partial \bar{\eta}}{\partial x} - \frac{\partial R_{xx}}{\partial x} - \frac{\partial}{\partial x}\left(\frac{E}{2}\right) \\
& + \frac{\rho \hat{a}}{2}\frac{\partial \hat{w}_s^2}{\partial x} + \frac{\rho \hat{w}_s^2}{2}\frac{\partial \bar{\eta}}{\partial x} - \rho\left[q_{sx}\frac{\partial U_s}{\partial x} + \left(q_{wx} + \frac{\hat{a}U_s}{2}\right)\frac{\partial \hat{u}_s}{\partial x}\right] \\
& + \hat{a}\frac{\partial \tau_{yx}}{\partial y} - \frac{\partial R_{yx}}{\partial y} - \rho\left[q_{sy}\frac{\partial U_s}{\partial y} + \left(q_{wy} + \frac{\hat{a}V_s}{2}\right)\frac{\partial \hat{u}_s}{\partial y}\right] \\
& - \frac{\rho}{2}\frac{\partial\left(\hat{u}_s\hat{a}\right)}{\partial t_0} - \rho\frac{\partial\left(\bar{\eta} - \hat{a}\right)}{\partial t_0}U_s + \frac{1}{2}\rho\hat{u}_s\frac{\partial \hat{a}}{\partial t_0} \\
& - \rho\frac{\partial\left(U_s\hat{a}\right)}{\partial t_0} - \rho\frac{\partial q_{srx}}{\partial t_0} \qquad (B.45)
\end{aligned}
$$

The mean trough shear stress in the y-direction, τ_{csy}, is obtained by replacing in the previous equation x by y, $(\hat{u}, U)$ by $(\hat{v}, V)$, and vice versa.

B.11   Mean bottom shear stress

Integrating the horizontal momentum equation (B.28) from the bottom $(z = -h)$ to the trough level $(z = z_{tr} = \bar{\eta} - \hat{a})$ and time-averaging over the wave period, we obtain

$$
\begin{aligned}
& \rho\frac{\partial}{\partial t_0}\int_{-h}^{z_{tr}} \bar{u}\,dz - \rho\frac{\partial z_{tr}}{\partial t_0}u_{tr} + \rho\frac{\partial}{\partial x}\int_{z_{tr}}^{\eta}\overline{u^2}\,dz - \rho\frac{\partial z_{tr}}{\partial x}\overline{u_{tr}^2} \\
& + \rho\frac{\partial}{\partial y}\int_{-h}^{z_{tr}}\overline{uv}\,dz - \rho\frac{\partial z_{tr}}{\partial y}\overline{u_{tr}v_{tr}} + \rho\overline{u_{tr}v_{tr}} \\
& = -\frac{\partial}{\partial x}\int_{-h}^{z_{tr}}\bar{p}\,dz + \frac{\partial z_{tr}}{\partial x}\bar{p}_{tr} + \frac{\partial h}{\partial x}\bar{p}_b + \int_{-h}^{z_{tr}}\frac{\partial \overline{\tau}_{yx}}{\partial y}\,dz + \overline{\tau}_{tr,zx} - \overline{\tau}_{b,zx} \qquad (B.46)
\end{aligned}
$$

where the subscript b refers to the bottom, $z = -h$. As before, we have neglected the contribution of τ_{xx} and applied the kinematic bottom boundary condition. Introduc-

ing (B.31), the mean bottom shear stress, τ_{cbx}, results:

$$
\begin{aligned}
\tau_{cbx} = \overline{\tau_{b,zx}} \; = \; & \tau_{ax} - \frac{\partial}{\partial x}\left(P_s + \int_{-h}^{z_{tr}} \bar{p}\,dz\right) + p_a\frac{\partial\bar{\eta}}{\partial x} + \bar{p}_b\frac{\partial h}{\partial x} \\
& - \rho\left[\frac{\partial}{\partial t_0}\overline{\int_{z_{tr}}^{\eta} u_s\,dz} + \frac{\partial}{\partial t_0}\int_{-h}^{z_{tr}} \bar{u}\,dz\right] \\
& - \rho\left[\frac{\partial}{\partial x}\overline{\int_{z_{tr}}^{\eta} u_s^2\,dz} + \frac{\partial}{\partial x}\int_{-h}^{z_{tr}} \overline{u^2}\,dz\right] \\
& - \rho\left[\frac{\partial}{\partial y}\overline{\int_{z_{tr}}^{\eta} u_s v_s\,dz} + \frac{\partial}{\partial y}\int_{-h}^{z_{tr}} \overline{uv}\,dz\right] + \int_{-h}^{\bar{\eta}}\frac{\partial\bar{\tau}_{yx}}{\partial y}\,dz \quad (\text{B.47})
\end{aligned}
$$

By analogy with (B.24),

$$
\bar{p} = p_a + \rho g\left(\bar{\eta} - z\right) - \rho\frac{\hat{w}^2}{2} \tag{B.48}
$$

Introducing (B.6), (B.27) and (B.48) into (B.47), and accounting for the surface roller contribution yield

$$
\begin{aligned}
\tau_{cbx} \; = \; & \tau_{ax} + \tau_{sr,x} - \rho\frac{\partial q_{srx}}{\partial x} - \rho\frac{\partial q_{wx}}{\partial t_0} - (\bar{\eta}+h)\frac{\partial p_a}{\partial x} - \rho g\left(\bar{\eta}+h\right)\frac{\partial\bar{\eta}}{\partial x} \\
& - \frac{\partial S_{xx}}{\partial x} - \rho\overline{\tilde{w}_b^2}\frac{\partial h}{\partial x} - \rho\frac{\partial}{\partial t_0}\int_{-h}^{\bar{\eta}} U\,dz - \rho\frac{\partial}{\partial x}\int_{-h}^{\bar{\eta}} U^2\,dz - \rho\frac{\partial}{\partial x}\left(2q_{wx}U_s\right) \\
& - \frac{\partial S_{yx}}{\partial y} - \rho\frac{\partial}{\partial y}\int_{-h}^{\bar{\eta}} UV\,dz - \rho\frac{\partial}{\partial y}\left(q_{wy}U_s + q_{wx}V_s\right) + \int_{-h}^{\bar{\eta}}\frac{\partial\bar{\tau}_{yx}}{\partial y}\,dz \quad (\text{B.49})
\end{aligned}
$$

where, as Tajima (2004) points out, the term $\rho\overline{\tilde{w}_b^2}\frac{\partial h}{\partial x}$ is negligible for a gently sloping bottom. S_{xx}, S_{yx} and S_{yy} are the radiation stresses, defined as

$$
S_{xx} \; = \; \rho\int_{-h}^{\bar{\eta}}\left(\overline{\tilde{u}^2} - \overline{\tilde{w}^2}\right)dz + \frac{E}{2} \tag{B.50}
$$

$$
S_{yx} \; = \; S_{xy} = \rho\int_{-h}^{\bar{\eta}}\overline{\tilde{u}\tilde{v}}\,dz \tag{B.51}
$$

$$
S_{yy} \; = \; \rho\int_{-h}^{\bar{\eta}}\left(\overline{\tilde{v}^2} - \overline{\tilde{w}^2}\right)dz + \frac{E}{2} \tag{B.52}
$$

Again, the mean bottom shear stress in the y-direction, τ_{cby}, is obtained by replacing x by y, $(\hat{u}, U)$ by $(\hat{v}, V)$, and vice versa, in (B.49).

B.12 Simplifications in the depth-integrated momentum equations

We use the approach suggested by Tajima (2004) to introduce a simplification in (B.49). We write the mean current velocity under the trough level in the following way:

$$(U, V) = (U_0, V_0) + (U', V') \tag{B.53}$$

where (U_0, V_0) are the depth-averaged mean current velocities below the trough level,

$$(U_0, V_0) = \frac{1}{h_{tr}} \int_{-h}^{z_{tr}} (U, V) dz = \frac{1}{h_{tr}} (q_{bx}, q_{by}) \tag{B.54}$$

(q_{bx}, q_{by}) are the total fluxes below the trough level and $h_{tr} = h + \bar{\eta} - \hat{a}$ is the *trough level depth*. (U', V') are the current velocity departures with respect to the mean. We assume that $O(U') \ll O(\tilde{u})$ and therefore neglect terms of order U'^2. We also assume that $O(U_0) \sim O(V_0) \sim O(\tilde{u})$ and therefore keep terms of order U_0^2. Applying these considerations to (B.49), the expression of τ_{cbx} is simplified to

$$
\begin{aligned}
\tau_{cbx} = {} & \tau_{ax} - (h + \bar{\eta}) \frac{\partial p_a}{\partial x} - \rho g (h + \bar{\eta}) \frac{\partial \bar{\eta}}{\partial x} - \frac{\partial}{\partial x} S_{xx} - \frac{\partial}{\partial x} R_{xx} \\
& - \rho \overline{\tilde{w}_b^2} \frac{\partial h_0}{\partial x} - \rho \frac{\partial}{\partial x} \left((q_{sx} + q_{wx}) U_s + q_{bx} U_0 \right) \\
& - \frac{\partial}{\partial y} S_{yx} - \frac{\partial}{\partial y} R_{yx} - \rho \frac{\partial}{\partial y} \left(q_{sy} U_s + q_{wx} V_s + q_{by} U_0 \right) \\
& + \int_{-h}^{\bar{\eta}} \frac{\partial \bar{\tau}_{yx}}{\partial y} dz - \rho \frac{\partial q_x}{\partial t_0}
\end{aligned} \tag{B.55}
$$

where $q_x = q_{bx} + U_s \hat{a} + q_{wx} + q_{srx}$ is the total flux in x-direction, due to currents (below and above the trough level), waves, and surface roller.

B.13 Mass conservation

To complete the formulation, we need to include an equation that guarantees mass conservation. Integrating (B.38) from $z = -h$ to $z = \eta$, and taking into account

surface roller effects, we obtain, after applying Leibnitz rule,

$$\frac{\partial}{\partial x}\left(\int_{-h}^{\eta} u\,dz + q_{srx}\right) + \frac{\partial}{\partial y}\left(\int_{-h}^{\eta} v\,dz + q_{sry}\right)$$
$$- u\frac{\partial \eta}{\partial x} - u\frac{\partial h}{\partial x} - v\frac{\partial \eta}{\partial y} - v\frac{\partial h}{\partial y} + w_\eta - w_b = 0 \qquad (B.56)$$

where the subscript b refers to the bottom level, $z = -h$, and the subscript η refers to the surface, $z = \eta$. The kinematic free surface and bottom boundary conditions respectively require

$$w_\eta - u\frac{\partial \eta}{\partial x} - v\frac{\partial \eta}{\partial y} = \frac{\partial \eta}{\partial t} \qquad (B.57)$$

$$-w_b - u\frac{\partial h}{\partial x} - v\frac{\partial h}{\partial y} = 0 \qquad (B.58)$$

Introducing (B.57) and (B.58) into (B.56) and time-averaging over a wave period yield

$$\frac{\partial \bar{\eta}}{\partial t_0} + \frac{\partial}{\partial x}\left(q_{cx} + q_{wx} + q_{srx}\right)$$
$$+ \frac{\partial}{\partial y}\left(q_{cy} + q_{wy} + q_{sry}\right) = 0 \qquad (B.59)$$

Appendix C

Offshore radiation condition

Here, we describe the radiation condition to be satisfied in the offshore boundary. We apply the classic Sommerfeld radiation condition (e.g., Sundstrom and Elvius, 1979). Its purpose is to "radiate" disturbances outside the computational domain, avoiding spurious reflection.

From the linearized depth-integrated equations of motion for long waves, and neglecting bottom friction, we have for water of constant depth, h,

$$\frac{\partial u}{\partial t} = -g\frac{\partial \eta}{\partial x} \tag{C.1}$$

$$\frac{\partial \eta}{\partial t} = -h\frac{\partial u}{\partial x} \tag{C.2}$$

where u is the depth-averaged velocity and η is the surface elevation above the sea water level. Differentiating (C.1) with respect to time, t, and replacing $\frac{\partial^2 \eta}{\partial x \partial t}$ by use of (C.2), we obtain the governing equation in terms of u:

$$\frac{\partial^2 u}{\partial t^2} - gh\frac{\partial^2 u}{\partial x^2} = 0 \tag{C.3}$$

Once (C.3) is solved, we obtain the surface elevation from (C.2).

Since the governing equation is linear, we may, for a periodic motion, take

$$u = \text{Re}\left\{\tilde{u}(x)e^{-i\omega t}\right\} \tag{C.4}$$

127

upon which (C.3) becomes

$$-\omega^2 \tilde{u} - gh\frac{\partial^2 \tilde{u}}{\partial x^2} = 0 \tag{C.5}$$

which has the solution

$$\tilde{u} = u_+ e^{ikx} + u_- e^{-ikx} \tag{C.6}$$

where the wave number k is

$$k = \frac{\omega}{\sqrt{gh}} \tag{C.7}$$

We assume η to be of the form

$$\eta = \text{Re}\left\{\eta_+ e^{i(kx-wt)} + \eta_- e^{-i(kx+wt)}\right\} \tag{C.8}$$

Inserting (C.6) and (C.8) in (C.2) we obtain

$$-i\omega\left(\eta_+ e^{ikx} + \eta_- e^{-ikx}\right) = -h\left(iku_+ e^{ikx} - iku_- e^{-ikx}\right) \tag{C.9}$$

or

$$\eta_+ = \frac{kh}{\omega}u_+ = \sqrt{\frac{h}{g}}u_+ \tag{C.10}$$

$$\eta_- = -\frac{kh}{\omega}u_- = -\sqrt{\frac{h}{g}}u_- \tag{C.11}$$

A progressive wave in the positive x-direction must obey the radiation condition (C.10), while a progressive wave in the negative x-direction must obey (C.11).

Bibliography

Battjes, J. A. and Janssen, J. P. F. M. (1978). Energy loss and set-up due to breaking of random waves. In *Proc. 16th Int. Coastal Engineering Conf.*, pages 569–578. Amer. Soc. of Civil Eng.

Bouws, E., Günther, H., Rosenthal, W., and Vincent, C. L. (1985). Similarity of the wind wave spectrum in finite depth water 1. Spectral form. *Journal of Geophysical Research*, 90(C 1):975–986.

Cavanié, A., Arhan, M., and Ezraty, R. (1976). A statistical relationship between individual heights and periods of storm waves. In *Proc. Conf. on Behaviour of Offshore Structures*, pages 354–360. Norwegian Institute of Technology.

Chen, Q., Kirby, J. T., Dalrymple, R. A., Kennedy, A. B., and Chawla, A. (2000). Boussinesq modeling of wave transformation, breaking and runup. II: Two horizontal dimensions. *Journal of Waterway, Port, Coastal and Ocean Engineering*, 126:48–56.

Dally, W. R. and Brown, C. A. (1995). A modeling investigation of the breaking wave roller with application to cross-shore currents. *Journal of Geophysical Research*, 100(C 12):24,873–24,883.

Dally, W. R., Dean, R. G., and Dalrymple, R. A. (1985). Wave height variation across beaches of arbitrary profile. *Journal of Geophysical Research*, 90(C 6):11,917–11,927.

Dean, R. G. (1965). Stream function representation of nonlinear ocean waves. *Journal of Geophysical Research*, 70(C 18):431–458.

Deigaard, R. (1993). A note on the three-dimensional shear stress distribution in a surf zone. *Coastal Engineering*, 20.

Deigaard, R. and Fredsoe, J. (1989). Shear stress distributions in dissipative water waves. *Coastal Engineering*, 13.

Ferziger, J. H. and Perić, M. (2002). *Computational methods for fluid dynamics*. Springer.

Hamilton, D. G. and Ebersole, B. A. (2001). Establishing uniform longshore currents in a large-scale sediment transport facility. *Coastal Engineering*, 42.

Hasselmann, K., Barnett, T. P., Bouws, E., Carlson, H., Cartwright, D. E., Enke, K., Ewing, J. A., Gienapp, H., Hasselmann, D. E., Kruseman, P., Meerburg, A., Müller, P., Olbers, D. J., Richter, K., Sell, W., and Walden, H. (1973). Measurements of wind-wave growth and swell decay during the Joint North Sea Wave Project (JONSWAP). *Dtsch. Hydrogr. Z. Suppl. A*, 8:1–95.

Isobe, M. (1979). Hozonha no setsudo-kai no hako ni yoru hyouji. *Annual Conference, JSCE*, 2(394):760–761.

Kirby, J. T., Wei, G., Chen, Q., Kennedy, A. B., and Dalrymple, R. A. (1998). FUNWAVE 1.0 fully nonlinear Boussinesq wave model documentation and user's manual. Research report CACR-98-06, Center for Applied Coastal Research, University of Delaware.

Lindgren, G. (1972). Wave-length and amplitude in Gaussian noise. *Adv. appl. Prob.*, 4:81–108.

Lindgren, G. and Rychlik, I. (1982). Wave characteristic distributions for Gaussian waves – wavelength, amplitude and steepness. *Ocean Engng*, 9:411–432.

Longuet-Higgins, M. (1983). On the joint distribution of wave periods and amplitudes in a random wave field. *Proc. R. Soc. Lond. A*, 389:241–258.

Longuet-Higgins, M. S. (1975). On the joint distribution of the periods and amplitudes of sea waves. *J. geophys. Res.*, 80(18):241–258.

Madsen, O. S. (1994). Spectral wave-current bottom boundary layer flows. In *Proceedings of the 24rd International Coastal Engineering Conference*, pages 384–398. ASCE.

Madsen, P. A., Banjamali, B., Schaffer, H. A., and Sorensen, O. R. (1996). Boussinesq type equations with high accuracy in dispersion and nonlinearity. In *Proceedings of the 25th International Conference on Coastal Engineering*, pages 95–108. ASCE.

Madsen, P. A., Sorensen, O. R., and Schaffer, H. A. (1997a). Surf zone dynamics simulated by a Boussinesq type model. Part I. Model description and cross-shore motion of regular waves. *Coastal Engineering*, 32:255–287.

Madsen, P. A., Sorensen, O. R., and Schaffer, H. A. (1997b). Surf zone dynamics simulated by a Boussinesq type model. Part II. Surf beat and swash oscillations for wave groups and irregular waves. *Coastal Engineering*, 32:289–320.

Mei, C. C. (1989). *The applied dynamics of ocean surface waves*, volume 1 of *Advanced Series on Ocean Engineering*. World Scientific.

Miche, R. (1951). Le pouvoir réfléchissant des ouvrages maritimes exposés à l'action de la houle. *Annals des Ponts et Chaussées*, 121:285–319.

Michell, J. H. (1893). On the highest wave in water. *Phil. Mag., 5th series*, 36:430–437.

Mitsuyasu, W. (1970). Development of spectra of wind and waves (2). In *Proceedings of the 17th International Coastal Engineering Conference*, pages 1–7. ASCE.

Nairn, R. B., Roelvink, J. A., and Southgate, H. N. (1990). Transition zone width and implications for modelling surfzone hydrodynamics. In *Proceedings of the 22nd International Coastal Engineering Conference*, pages 68–81. ASCE.

Nikuradse, J. (1933). Strömungsgesetze in rauhen rohren. *VDI-Forshungsh.*, 361.

Nwogu, O. (1993). Alternative form of Boussinesq equations for nearshore wave propagation. *Journal of Waterway, Port, Coastal and Ocean Engineering*, 119(6):618–638.

Okayasu, A. and Katayama, H. (1992). Distribution of undertow and long-wave component velocity due to random waves. In *Proceedings of the 23rd International Conference on Coastal Engineering*, pages 883–893. Amer. Soc. of Civil Eng.

Peregrine, D. H. (1967). Long waves on a beach. *Journal of Fluid Mechanics*, 27:815–827.

Ruessink, B. G., Miles, J. R., Feddersen, F., Guza, R. T., and Elgar, S. (2001). Modeling the alongshore current on barred beaches. *Journal of Geophysical Research*, 106(C 10):22,451–22,463.

Srokosz, M. A. and Challenor, P. G. (1987). Joint distributions of wave height and period: A critical comparison. *Ocean Engng*, 14(4):295–311.

Stive, M. J. F. and De Vriend, H. J. (1994). Shear stresses and mean flow in shoaling and breaking waves. In *Proceedings of the 24rd International Coastal Engineering Conference*, pages 594–608. ASCE.

Sundstrom, A. and Elvius, T. (1979). Computational problems related to limited-area modelling. In *Numerical methods used in atmospheric models, Vol. 2*, number 17 in GARP Publ. Series, part 7, pages 381–419. World Meteorol. Org., Geneva, Switzerland.

Svendsen, I. A. (1984). Mass flux and undertow in a surf zone. *Coastal Engineering*, 8:303–329.

Tajima, Y. (2004). *Waves, currents, and sediment transport in the surf zone along long, straight beaches.* PhD dissertation, Massachusetts Institute of Technology, Department of Civil and Environmental Engineering.

Thornton, E. B. and Guza, R. T. (1983). Transformation of wave height distribution. *J. Geophys. Res.*, 88:5925–5938.

Wang, P., Smith, E. R., and Ebersole, B. A. (2002). Large-scale laboratory measurements of longshore sediment transport under spilling and plunging breakers. *Journal of Coastal Research*, 18(1):118–135.

Watanabe, A., Hara, T., and Horikawa, K. (1984). Study on breaking condition for compound wave trains. *Coastal Engineering in Japan*, 27:71–82.

Wei, G., Kirby, J. T., Grilli, S., and Subramanya, R. (1995). A fully nonlinear Boussinesq model for surface waves, part 1. Highly nonlinear unsteady waves. *Journal of Fluid Mechanics*, 294:71–92.